Chapter 1

Introduction

Nanowires or nanofibers are mechanical nanostructures that have been investigated to provide solutions to many applications of modern technologies. Specifically in areas such as: biomedical, aeronautical, automotive, microelectronics and industrial instrumentation, the nanofibers have proven to develop significant impact in the near future.

Research in nanofibers has progressed intensively during the last 20 years due to their novel characteristics which generates solutions to many day to day miniaturization devices that serve the human mankind. Carbon nanofibers have shown good electrical conductivity, good thermal conductivity, and good mechanical strength. Nanofibers can be produced from a wide range of materials and processes, and many possible applications have been proposed [1-6]. One application is to build a gas sensor device with a heater element to vary the temperature. The heater element in the sensor raises the operating temperature (i.e. 300-600 ^{o}C) to reach a suitable working regime for electrochemical reactions to occur. The nanofiber performs the heating/sensing function having an electrical current to drive the device.

Other applications for nanofibers as will be mentioned in chapter 3 include: filtration; affinity membranes; tissue engineering scaffolds; drug delivery systems; sensors; energy conversion and storage; reinforcement; and molecular electronics.

Fibers have been commercially successful as air filters. Self-assembled monolayers can be produced when nanofiber membranes are functionalized to react with molecules. Fibers can also be used as scaffolds for tissue engineering applications in which cells react to the fiber enhanced microenvironment. Drug delivery systems can also be developed and improved by the use of nanofibers that could release the drugs in a controlled timed manner. The sensor industry could benefit from the small size and fast response of nanofibers. Nanofibers can also reinforce

materials such as other polymers or metals to withstand stronger impacts. Molecular electronics benefits from nanofibers with nanogaps to generate basic working units.

The importance of fabrication, characterization and operation of nanofibers becomes a very important research area to provide feasible solutions for implementing sensors, actuators and other mechanical nanostructures in different fields related to: medical, industrial, aerospace and commercial applications.

1.1 Problem Statement and Objectives

1.1.1 Research problem

This research develops a methodology for the characterization and properties identification of glassy carbon nanofibers which includes: their geometry, nanoconstriction generation due to applied electrical fields, nano-gap formation due to power dissipation and tension/compression stress induction due to controlled electrical current applications, and glowing emission due also to controlled experiments with electrical variables such as voltages and electrical current circulation. The methodology provides experimentation on glassy carbon nanofiber samples, suspended between two carbon electrode structures which were fabricated in controlled clean rooms using photolithography processes. The sequence of steps to develop the characterization methodology includes: nanofiber manufacturing, sample identification and observation using a Scanning Electron Microscope (SEM), experimental set up to apply voltage and current to the sample using a data acquisition system, experimental set up using a vacuum chamber to operate the tests at minimum or no-oxygen conditions, and the final observation of the nanofiber samples observed again over a SEM. Finally, the research focus on future specific applications that provide an initial analysis platform to continue with solutions in gas sensors, electrochemical reaction enhancers, stem cell differentiation stimulation, and carbon nanofiber based glowing devices.

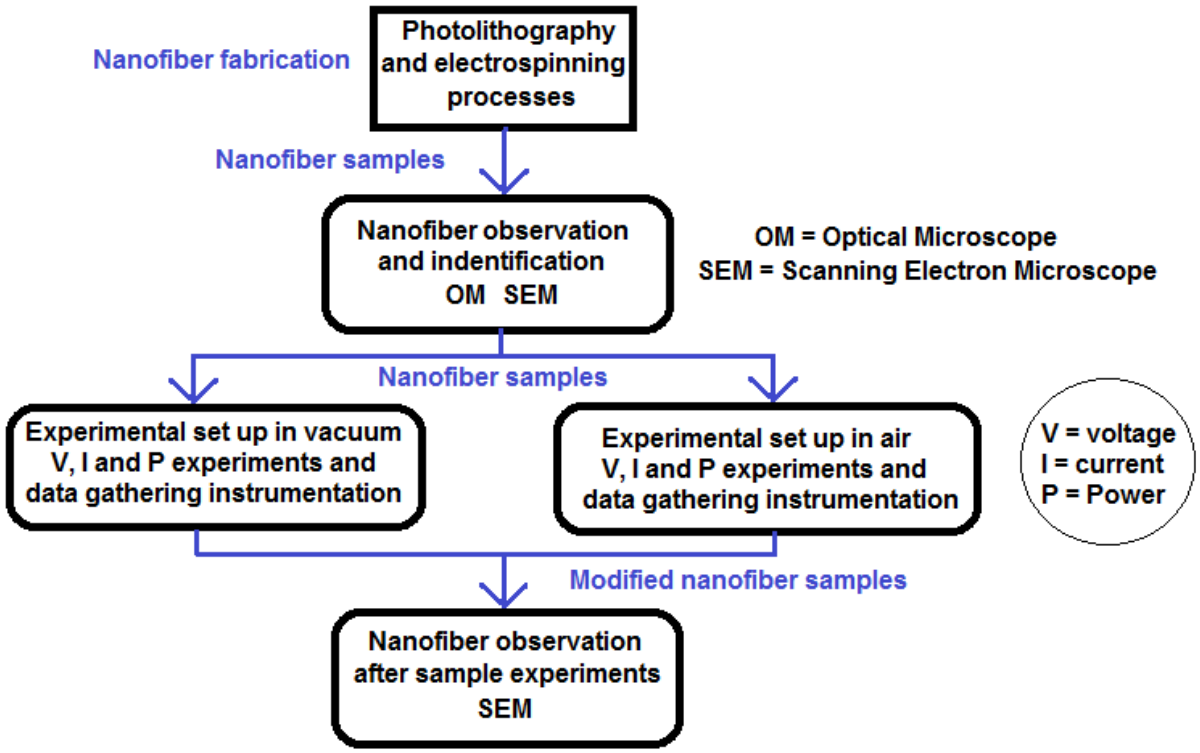

Figure 1.1: Characterization methodology for the nanofiber samples

1.1.2 Research objectives

This dissertation has the following particular objectives:

1. To manufacture glassy carbon nanofiber samples using appropriate and efficient photolithography processes in advanced clean room conditions and/or electrospinnig processes.
2. To identify and observe the nanofiber sample structures using both, optical (50X) and Scanning Electron (SEM) microscopes in order to perform a geometric characterization of the sample.
3. To develop a mathematical model for predicting temperature changes and melting phenomenon in the nanofiber when current is flowing through the nanostructure.
4. To design the experiment in free air to induce nanoconstriction, nanofiber breackdown, and nanogaps in the nanostructure samples, such that electrical variables like voltage and

current can be controlled, and a data gathering processing can be performed to measure power dissipation and conductivity.

5. To design the experiment in vacuum to induce nanoconstriction, nanogaps and nanoglowing in the nanostructure samples, such that electrical variables like voltage and current can be controlled and a data gathering processing can be performed to measure power dissipation and conductivity.
6. To observe the nanofiber sample structures once the experiments are finished using the Scanning Electron Microscope (SEM) to identify phenomena such as nanoconstriction, nanofiber breackdown, and nanogap formation.
7. To document the results and prepare a recommendation table for glassy carbon nanofiber where characterized parameters are suggested for specific applications such as nanogaps, nanoconstriction and nanoglowing.

1.2 Experimentation Preview

The electrical current flowing through a nanofiber induces a temperature change; therefore, if a control is established in the applied voltage, the nanofiber´s temperature can be modified. A good electrical contact between the nanofiber prototype and contact pads is fundamental to flow a controlled current through the nanofiber structure. This research takes advantage of a fiber fabrication technique such as electrospinning, and microfabrication techniques, such as photolithography, and converts polymer solutions to glassy carbon suspended fibers after pyrolysis. The contact pads, all the supporting electrodes and the nanofibers, are made out of polymer solutions. The exact polymer solution combination for each structure will be described in the experimental setup.

While controlling the current through the nanofiber structure, if the fiber breaks, it will be unable to work as a proper heater element. Therefore, a comprehensive understanding of the safe power limits that the nanofibers can absorb, and an adequate technique to control the electrical current sent to the nanowire, are two very important aspects to consider.

The nanofiber breakdown phenomenon could be used in a constructive way by controlling the electrical variables applied to the system. This induces a very well formed nanogap that can be appreciated using the SEM systems [7-55]. Nanogaps are fundamental building blocks for the fabrication of nanometer-sized devices and circuits which include single electron tunneling transistors (SETT). They can also be an important tool for the analysis of material properties at nanometer scale or even in the molecular scale. Normally, generating nanogaps using current technology is a costly and time consuming process. Also, the materials used to build those nanogaps are metals such as gold [14]. Therefore, an alternative nanogap generation technique can be developed using simple cost-effective electrical variable control over the nanofiber. To generate nanogaps from suspended glassy carbon fibers requires previous knowledge of the electrical characteristics of the fiber itself (i.e. their electrical resistance). Once the resistance of the fibers is evaluated, a control over those characteristics must be accomplished in order to modify the fiber geometry, particularly in the generation of a nanoconstriction. The nanoconstriction is started when the electrical power dissipated by the fiber goes beyond certain threshold. Finally, if the nanoconstriction is further continued, a nanogap is produced.

This research work uses glassy carbon nanofibers which are suspended between two carbon wall electrodes/contact pads. The nanofibers are studied carefully and their experimentation includes several different sizes and diameters. They are fabricated by an electrospinning technique from an optimized polymer solution.

1.3 Previous Research and State of The Art

Carbon has been studied and used since many years now as an industrial applications material. Since the 1950´s, the studies on carbon properties were focused on bulk material of glassy carbon. However, as the microfabrication technology has improved, the size of the carbon samples that researchers can study have also underwent a dramatic reduction in size, from a few millimeters to a few micrometers and even to the nanometer range. This ability to create and study small structures due to technological developments, have made possible to start controlling

micro and nano device fabrication and to analyze micro and nanostructures, such as very thin films, nanotubes, and nanofibers. Nanofibers, in particular, are interesting because of their potential application in many different areas such as electrochemical electrodes, gas sensors, stem-cell simulation solutions, nano-electronic transistors, SETT´s, scaffolds for tissue engineering, and more [3].

The surface of a particular carbon allotrope can be modified in several different ways. For example, a carbon surface can be modified by using a laser, using an electron beam, passing an electrical current throughout the sample, or by neutron irradiation [56-64].

In the case that a laser is used to modify a glassy carbon surface [62], the glassy carbon samples are irradiated by a number of superimposed laser pulses. This produces a temperature increase due to the energy density delivered to the material. In [62], the authors suggest that the temperature of the glassy carbon samples did not reach its melting point under their experiments. However, a higher energy density would make the temperature rise to its melting point. This process, as suggested by the authors, modifies the microstructure of the irradiated samples by the careful choice of the laser irradiation conditions.

When glassy carbon samples are neutron irradiated, the microstructure changes according to [61]. The authors mention that the porosity of glassy carbon reduces after being neutron irradiated. Also, the glassy carbon samples used show micro and macro cracks due to neutron irradiation. The size of the glassy carbon samples used by [61] leads to sample shrinkage after being neutron irradiated.

In [30], a graphene layer was modified using the help of both an electron beam and an electrical current. The main purpose of this work was to generate nanoconstrictions, and measure their widths and electronic properties. Table 1.1, 1.2, 1.3, and 1.4 summarizes the several important and significant research contributions to the field of nanofibers that serve as platform to our research endeavor. Even though, those tables are not exhaustive, but provide some very representative research efforts in mechanical nanostructures such as nanowires or nanofibers.

Table 1.1: Research Contributions in nanofiber, nano particles and glassy carbon structures

Title	Authors / Journal / Year	Summary
Application of electrospun nanofibers [3]	Fang, J.; Niu H.; Lin, T.; Wang, X. / Chinese Science Bulletin (SpringerLink) / 2008	Very good overall description of electrospun nanofiber applications. Nanofibers possess an excellent surface to volume ratio, and pore interconnectivity. The surface chemistry of the polymer itself, from which the fibers are obtained, provides the nanofibers with desirables properties for a range of applications.
Characterization of fullerenes and carbon nanoparticles generated with a laser-furnace technique [58]	Ishigaki, T.; Suzuki, S.; Kataura, H.; Krätschmer, W.; Achiba, Y. / Applied Physics A / 2000	Laser ablation of a graphite rod and in situ separation of carbon soot by temperature gradient sublimation was systematically investigated using a laser-furnace apparatus. Laser Raman spectroscopy was also applied to deduce structural information of the carbon deposits.
Glassy carbon layer formed in diamond-like carbon films with femtosecond laser pulses [63]	Yasumaru, N.; Miyazaki, K.; Kiuchi, J. / Applied Physics A / 2004	Glassy carbon layer was modified from diamon-like carbon films with femtosecond laser pulses. In this work, the authors claim that the glassy carbon layer is produced most efficiently at low laser intensity near the ablation threshold of the diamond-like carbon films.

Table 1.2: Research Contributions in LASER driving nanofiber and glassy carbon surfaces

Title	Authors / Journal / Year	Summary
Laser processing of materials [57]	Majumdar, J.; Manna, I. / Sadhana / 2003	This work provides an overview of the application of lasers for material processing. In particular, laser-assited forming, joining, machining and surface engineering. A particular attention is drawn to laser surface engineering. Special mention is made about laser surface vitrification or amorphization.
Laser synthesis of carbon nanofibers and nanoclusters [56]	Antipov, A.; Arakelyan, S.; Kutrovskaya, S.;Kucherik, A.; Osipov, A.; Prokoshev, V.;Schekin, A. / Nanotechnologies in Russia / 2011	In this work, results of laser synthesis of carbon nanomaterials during the deposition of carbon vapors are presented. In particular, they show results from experiments on the laser action on the carbon targets, in the presence of a constant electric field, and also in the presence of inhomogeneous magnetic fields. They show that a change in the target material and action modes allows a change in the structure of the deposited layer.
Laser-induced structural modifications of glassy carbon surfaces [62]	Vitali, G.; Rossi, M. / Journal of Applied Physics / 1995	They report structural modifications induced by pulsed laser irradiations in the surface layers of glassy carbon. The glassy carbon samples were irradiated by 30 superimposed pulses. The energy density delivered to the material, and the repetition rate of the laser, were chosen so that the temperature increase of the irradiated surface layers was below the melting point of glassy carbon.

Table 1.3: Research Contributions in carbon nanoparticles, glassy carbon properties and graphene nanoconstrictions

Title	Authors / Journal / Year	Summary
Time evolution of emission by carbon nanoparticles generated with a laser furnace technique [60]	Suzuki, S.; Yamaguchi, H.; Ishigaki, T.; Sen, R.; Katasaura, H.; Kratschmer, W.; Achiba, Y. / The European Physical Journal D / 2001	The time evolution of emission by carbon nanoparticles generated with a laser furnace technique was investigated using a high-speed video camera. The internal temperature of the samples was determined as a function of time delay after laser vaporization. Differences in emission were found under different experimental conditions.
Effect of neutron irradiation on properties of glassy carbon [61]	Virgil, Y.; Lebedev, I. / Inorganic Materials / 2002	Experimental data is shown on the effect of neutron irradiation on the dimensions and properties of glassy carbon. The irradiation performed leads to a linear shrinkage of the samples. The effects of the irradiation are analyzed in terms of the microstructure and properties of glassy carbon.
In situ electronic characterization of graphene nanoconstrictions fabricated in a transmission electron microscope [30]	Lu, Y.; Merchant, C.; Drndic, M; Johnson, A. / Nanoletters / 2011	In this work, it is reported electronic measurements on graphene nanoconstrictions. An electrical current was used to anneal and clean the material and improve its electronic properties. Then a transmission electron microscope beam was used to modify the samples into a series of desired widths in the range of 1-700 nm.

Table 1.4: Research Contributions in nanowire modeling, nanocontacts, Joule heating, nanofiber interconnects and microlamps

Title	Authors / Journal / Year	Summary
A governing parameter for the melting phenomenon at nanocontacts by Joule heating and its applications to joining together two thin metallic wires [65]	Tohmoyoh, H./Journal of Applied Physics/ 2009	This paper provides a mathematical model of the temperature changes in a metal nanofiber/nanowire using a heat conduction partial differential equation and its steady state a transient solution. The application is focused at the melting phenomenon using Joule heating to generate wire bounding at nanoscale.
Heat conduction model for nanowire applications [66]	Tohmoyoh, H./Journal of Applied Physics/ 2013	This paper improves the model illustrated in 2009 by incorporating additional factor to improve the estimation of temperatures in the nanowire. The model develops the conditions and justifies the assumptions made for the applications of nanowire bounding.
Length dependence of current-induced breakdown in carbon nanofiber interconnects [67]	Kitsuki, H., Yamada, T., Fabris, D., Jameson, J.R., Wilhite, P., Suzuki, M., and Yang, C.Y./ Journal of Applied Physics/ 2008	The paper describes the breakdown phenomenon for carbon nanofibers with applications to interconnects applications. The article provides a model between current density through the fiber and the temperature reached using Joule heating and heat diffusion. They also discuss the characteristics of the breakdown including threshold temperature and critical value.
MEMS-based incandescent microlamps for integrated optics applications [68]	Alayo, M.I., Rehder, R., and Carreño, M. N. P.,/ Journal of Optics A/2008	The paper shows the fabrication and operation of incandescent microlamps for integrated optics applications. In this case the microlamp emits white and infrared light from a chromium resistor embedded in a free-standing silicon oxynitride (SiO_xN_y) cantilever that can be coupled to an optical waveguide. The device is built using front-side bulk micromachining of a silicon substrate in potassium hydroxide (KOH) solution.

1.4 Research Organization

This dissertation is divided in chapters that follow the chronological steps since the initial concept of the problem. Chapter 1 (this current chapter) describes the background information, problem statement, objectives, experimentation preview, previous research and state of the art in the areas of nanofibers, nanowires, nanogaps and nanoglowing (incandescence) made using glassy carbon materials. Chapter 2 illustrates the nanofiber fabrication process that includes photolithography, electrospinning, and pyrolysis. Photolithography is used to build the carbon electrode (or carbon-MEM) support structure. Electrospinning includes the wide variety of procedures such as: far field, electrospraying, multijet, coaxial, emulsion, melt, and near-field. Chapter 3 describes the fundamental aspects of the electromigration, nanoconstrictions and nanogaps. It also provides some fundamental background on carbon as the building material for the nanofiber structures studied in this dissertation; it particularly emphasizes on glassy carbon, photoresist and pyrolysis processes, and mechanical/electrical properties of glassy carbon material. Lastly, it discusses some of the emergent technologies and applications of nanofibers and nanowires, including sensors, high performance semiconductor devices, nanoglowing devices such as microlamps, bound wires in microelectronics, among others. Chapter 4 describes a mathematical model based upon the Joule heating conduction equations to predict operating temperatures at the point where the nanoconstriction and nanogaps arise in the nanofiber structure. Chapter 5 shows the control and data acquisition hardware to handle the experimental set up, data collection instrumentation, control routines and post-processing algorithm. The instrumentation includes graphical programming instrumentation and a DAQ box to facilitate the data gathering process. Chapter 6 describes the experimentation methodology and the experiments performed. Here, experiments having the nanofiber samples exposed to air are considered using the instrumentation hardware. Chapter 7 describes the experiments performed having the nanofiber samples operating in vacuum conditions. Also the temperature and power profiles are discussed in detail to provide an insight to the validation of the Joule heating model of the nanofiber. Experimental results presented in Chapter 6 and 7 are described in terms of current, voltage, resistance and power signal profiles and they explain how the controlled and different threshold levels were reached. Images from SEM are illustrated, before and after the

sample was driven into the experiment. Finally, Chapter 8 provides the conclusive remarks about this research and the recommendations for future development endeavors. The Reference section, after Appendices, shows more than 120 bibliographic sources that were consulted during the development of this research.

The Appendices illustrate the following items:

A. Glossary of terms
B. LabVIEW code of control program.
C. MATLAB code for data processing.
D. Additional Test Results.
E. Derivation of Heat Equation with Joule Heat; both for steady and transient states.

Chapter 2

Nanofiber Fabrication Processes

This chapter describes the fabrication processes followed to develop the sample mechanical nanostructures used in the characterization of the glassy carbon nanofibers. The processes discussed here comprehend:

1. The C-MEMS support structure, which includes the photolithography process to generate the interface connections and electrode to the nanofiber.
2. The electrospinning process, which includes the use of specific polymer solutions to tend and suspend the nanofiber over two carbon walls.
3. Pyrolysis process, which includes an annealing procedure to solidify the nanofiber having robust and firm nanostructure.

2.1 Introduction to the Nanofiber Fabrication

In this research, suspended glassy carbon nanofibers were fabricated. Microfabrication steps are necessary in order to build and mount the nanofibers over a rigid and robust carbon platform, where electrode contacts are developed for further experimentation. Standard photolithography is used in order to set up and define the initial structure that becomes the C-MEMS support structure.

The following sections describe the complete fabrication process of the suspended glassy carbon fibers. The description follows a sequence of procedures that go along the sections included in this chapter. First, the C-MEMS (Carbon-Micro-Electro-Mechanical-Systems) support structure is described. Then, the electrospinning process used is described. Finally, a brief explanation of the process that converts a polymer solution into glassy carbon consolidates

the fabrication sequence. Figure 2.1 illustrates the sequential processes to build the suspended glassy carbon nanofiber samples.

Figure 2.1: Complete overall fabrication steps

2.2 Carbon Electrode Support Structure

The support electrode structure, on which the polymer fibers will be electro spun, starts out as a micro-fabricated polymer structure. The microfabrication technique used to fabricate such nanostructures is very similar to the standard photolithographic processes used to manufacture CMOS Integrated Circuits. In photolithography, one can choose the desired height that a given microstructure will have. The height of the nanosctructure is controlled by carefully performing several steps during the photolithographic fabrication process.

The support structure can be converted into carbon by heat treatment (or annealing). This carbon structure is then used to provide an electrical contact path between external circuitry and the fiber. Figure 2.2 shows pictures of a typical support structure and the electrical contact pads. Without this carbon structure it would be difficult to make a good electrical contact with the fiber due to its size. In other words, this carbon structure provides with electrodes to make electrical contact with the nanofiber sample.

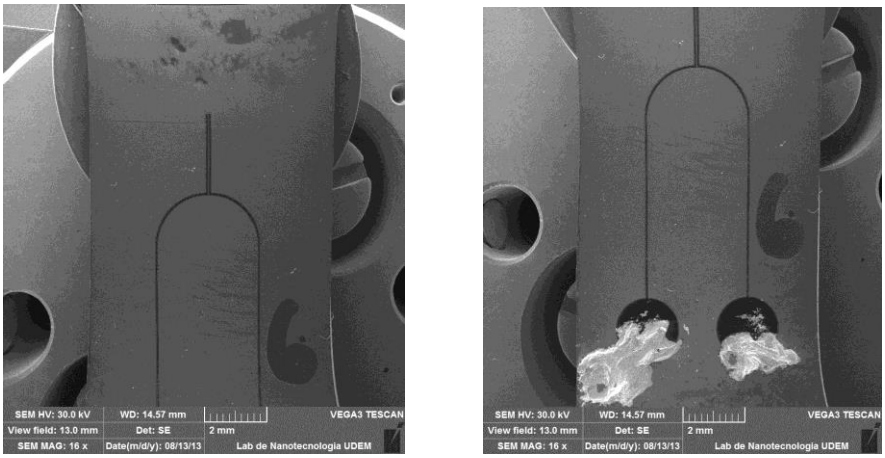

Figure 2.2: Carbon support structure and electrical contact pads (right)

A note on the carbon nanofiber structure is that its contact pads are larger in size compared to other portions of the sample. This allows a practical way to make electrical connections when manually manipulating the sample. However, due to the rough surface of the carbon structure, if one tries to make a good electrical connection to the pads using a simple alligator clip, it would be very difficult indeed and excessive noise would be obtained in the measured signals responses during experiments.

There are several possible solutions to make good electrical contact with the carbon contact pads. One possible solution is to build a holder device that will bring down a pin. This pin connector will make electrical contact on most of the surface of the carbon contact pad. Also, the holder device could have a spring to push the pin against the carbon pad and hold it in that position. However, this solution was not implemented. The reason is that the silicon wafer beneath the carbon structure could suffer mechanical damage by this method.

Another possibility to make a good electrical contact with the carbon contact pads is to cover the carbon contact pads with silver paste, as illustrated in figures 2.2 (right) and 2.3. Silver paste can adhere to carbon much better than other common solder pastes used in electronics. This silver paste provides a larger contact surface area with the alligator clips. This greater surface area greatly improves the electrical contact by reducing the ohmic resistance between the carbon

pad and simple alligator clip. This solution was implemented for all the samples due to its simplicity and good results from the electrical circuit standpoint.

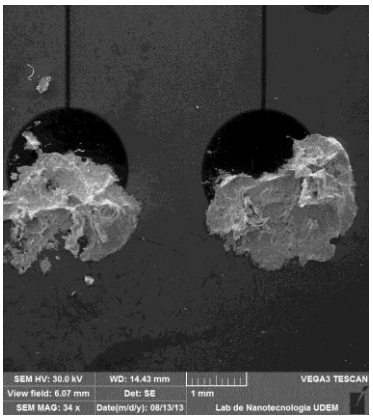

Figure 2.3: Silver paste on carbon contact pads

2.2.1 Photolithography process

Photolithography is a microfabrication process to pattern microstructures over a silicon wafer using: oxidation, photoresist coating, UV light exposure and photoresist developing. Figure 2.4 illustrates those fundamental steps and shows the sequence of subprocesses to generate the support structure. This procedure is also used to fabricate CMOS IC chips but with the addition of oxidation etching and photoresist strip sub-processes. Geometrical micro-patterns can be fabricated using this technique. Photolithography requires a photomask holding the geometric patterns to be transferred into a thin polymer film. This polymer film is a light sensitive photoresist.

The photoresist polymer Microchem's SU-8 is used to coat the Silicon wafer and to build the nanostructures used in this research. This photoresist allows a high aspect ratio in the fabricated micro/nanostructures. Possible thickness obtained fluctuates from a few microns to several hundred microns; SU-8 photoresist has a good UV light sensitivity between the 350-400 nm wavelength range. The conventional photolithography steps performed are as follows:

1. Substrate preparation.
2. Photoresist coating.
3. Soft bake of the coated Silicon wafer.
4. UV light exposure with the patterned mask.
5. Post exposure bake
6. Wafer development
7. Optional hard bake.

Figure 2.4 shows both, a graphical representation diagram and a sequential process flow diagram of the conventional steps used to fabricate the nanostructures. When preparing the Si substrate, it is advisable to clean it with deionized water and dry it with nitrogen gas to remove possible dust particles. During the coating step, the Silicon wafer is spin-covered with the photoresist; this film thickness will have a direct impact on the final structure thickness. The soft bake has to be performed on a hot plate with good temperature control and evenly distributed heat. The temperature for the hotplate is set to 95 ^{o}C. The time necessary for the wafer to stay over the hot plate for the soft-bake depends upon the thickness desired.

After removal of the spin-covered Si wafer from the hotplate, it follows an exposure to UV light. This exposure to UV light creates a chemical reaction on the exposed areas of the film that crosslinks its chemical bonds. This will avoid that these areas of the film get etched away during the development phase (negative photoresist). Therefore, only the harder to etch portions of the film will remain. Those areas constitute the electrode structure and support of the suspended nanostructure.

The post soft-bake (95 ^{o}C) has to follow immediately after exposure to UV light. Again, the post soft-bake time affects directly to the final thickness size of the photoresist film. After the post bake completion, the development sub-process is necessary to harden the patterned areas. This step requires the use of a developer solution that will remove the non-cross-linked portions of the film. Here is where only the electrode structures will remain on the Si wafer. The Si wafer has a thermally grown silicon dioxide (SiO_2) layer of about 500 nm that was formed during the

initial oxidation step. This SiO_2 layer work as an insulating layer between the electrically conducting carbon structures and the Si wafer.

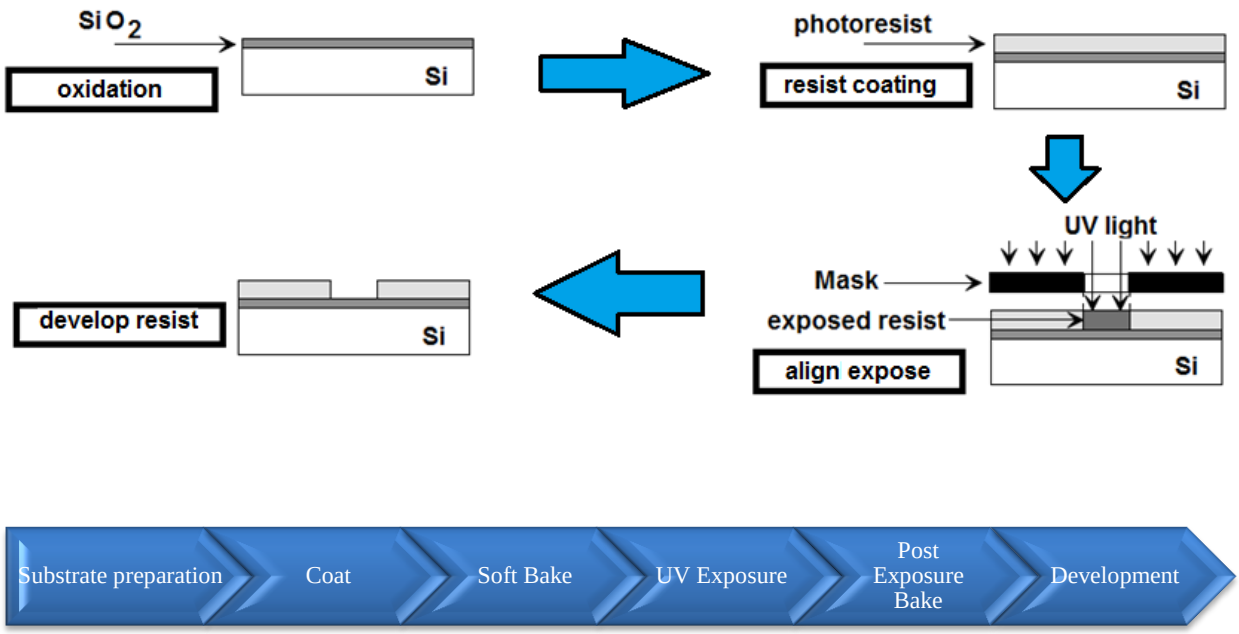

Figure 2.4: Photolithography conventional steps and process flow

Figures 2.5 and 2.6 shows the steps of SU-8 photoresist coating, and soft bake at 95°C, performed by the author at the class 1000 clean room facility of University of California, Irvine (UCI).

Figure 2.5: Coating of Si wafer with SU-8

Figure 2.6: Soft bake

2.3 Nanofiber Fabrication Technique: Electrospinning

Electrospinning is a common technique to manufacture micro and nanostructures which has been used in industry for many years. Some of the first commercial usages were for textile yarns and air filters. This technique uses an electrical charge to create very thin fibers (micrometers or nanometers in scale) out of polymers solutions. This technique does not require high temperatures or pressure, therefore facilitating its use with large and complex molecules. However, there are several modifications to this technique that may use heating of the polymer or air pressure to facilitate polymer flow.

In the basic electrospinning setup, a sufficiently high voltage (from 100 V for near field to 30 KV for far field) is applied to a liquid droplet, the droplet becomes charged and it counteracts the surface tension of the droplet, shooting out of the needle towards a grounded electrode by electrostatic repulsion. At the beginning of the process, a Taylor cone shows up, just after the tip of the syringe, and then the fibers are shoot out and stretched after this point. Figure 2.7 shows a general diagram of the electrospinning process where the so called near-field is illustrated closer to the needle cone and the so called far-field is illustrated further away from it. While the fiber continues its flight to reach the ground electrode, it dries and the mode of current flow changes from ohmic to convective due to a migration of the charges into the surface of the fiber jet. Then, a whipping process occurs causing the fiber jet to whip until reaching the ground electrode (collector). This whipping process instability is caused by electrostatic repulsion and it benefits the thinning of the fiber jet.

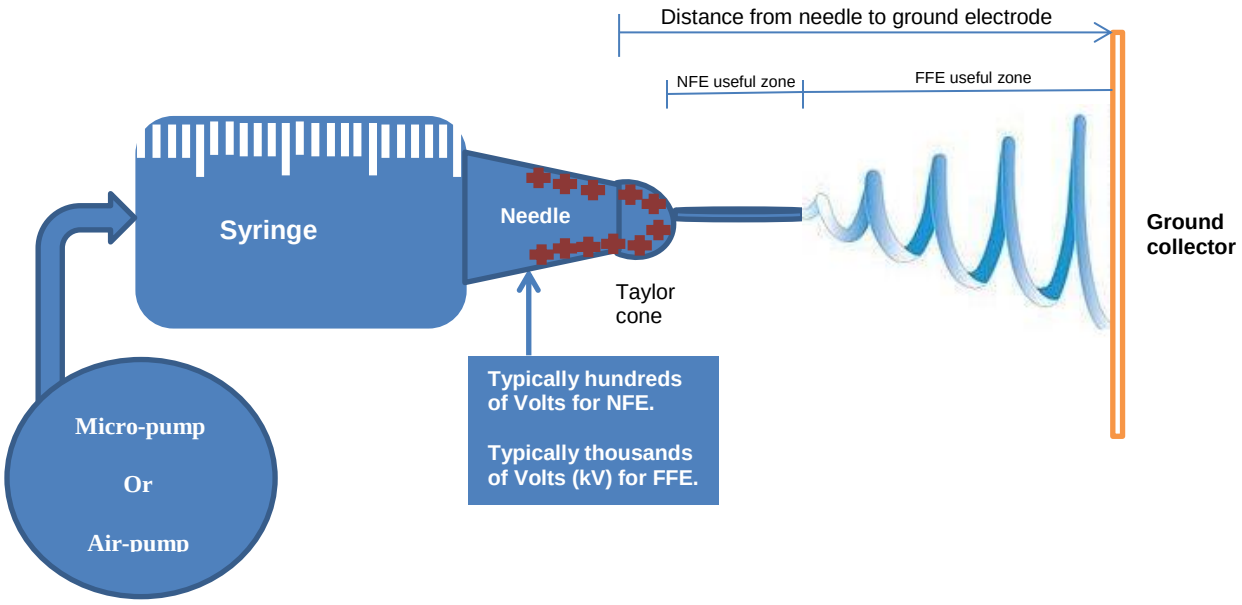

Figure 2.7: Basic electrospinning scheme

The parameters that control the outcome of the electrospinning process are:

1. The molecular weight of the polymer.
2. Polymer´s viscosity.
3. Polymer´s conductivity.
4. Polymer´s surface tension.
5. Applied electric potential.
6. Polymer´s flow rate.
7. Polymer´s concentration.
8. Distance between needle and collector electrode.
9. Ambient parameters such as temperature, humidity and air velocity in the chamber.
10. Motion and size of the collector electrode (for example if the collector is rotating then rpm's are important).
11. Needle gauge.

The final product of a normal electrospinning experiment is a fiber mat with a high surface-to-volume ratio and with fiber sizes from a few nanometers to several micrometers, depending on experimental parameter setup.

Electrospinning can have process variations that diverge from the basic technique. The following sections describe:

a) The traditional electrospinning technique, also known as Far Field Electrospinning (FFE).

b) Electrospraying which is a modification to traditional electrospinning, in which droplets are obtained instead of fibers.

c) Multijet Electrospinning.

d) Coaxial Electrospinning.

e) Emulsion Electrospinning.

f) Melt Electrospinning.

g) Near Field Electrospininng (NFE), which is the chosen technique to obtain the fiber samples used in this research.

The FFE approach to obtain suspended glassy carbon nanofibers was experienced by the author in this research when spending 3 months back in 2012 at the UNIST (Ulsan National Institute of Science and Technology) in Korea.

2.3.1 Far field electrospinning

As mentioned previously in this section, in a typical FFE, an electrostatic potential, normally between 10 KV and 30 KV, is applied between a spinneret and a ground collector. A spinneret works as the polymer source, which consists in a blunt tip needle of a certain diameter and a

syringe, with its polymer being fed in a controlled manner by a micro-pump or an air pump (see figure 2.7). The ground collector could be made of aluminum and have many different shapes: circular, squared, or rectangular. The collector can also be a static collector (no movement), or a rotating collector (i.e a drum form). The distance separating both of them is set between 10 cm to 30 cm. The solution used is normally a polymer with a solvent that evaporates during the spinning process.

In FFE, a droplet is first held at the needle tip by the polymer´s own surface tension. Then when the electric potential is applied between the spinneret and the collector, the interactions between the electrical charges in the polymer solution at the tip with the electric fields, cause the droplet to obtain a conical shape, also known as the Taylor cone. At some point, the applied electric field surpasses the surface tension of the droplet, making it unstable and ejecting a fiber jet towards the ground collector by means of electrostatic repulsion.

Figure 2.8 shows a photograph of the FFE machine used by the author at UNIST as part of his research stay in Korea. Flat collectors, as well as a drum collector were used to obtain suspended glassy carbon nanofibers by means of FFE. Examples of the results obtained by these experiments using the equipment from figure 2.8 can be seen in figures 2.9 and 2.10. Figure 2.10 shows the carbon support microstructures on which the nanofibers are suspended. These carbon support microstructures where fabricated by a photolithographic process such as the one mentioned previously in this chapter.

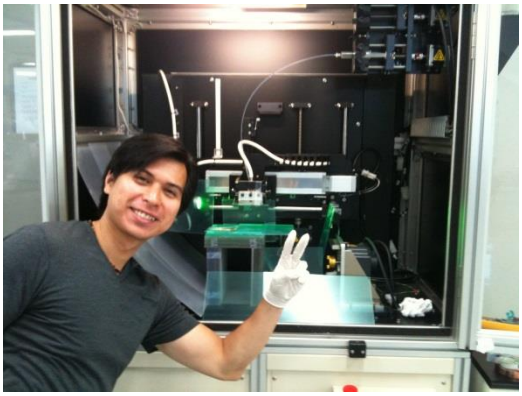

Figure 2.8: FFE equipment at UNIST in Korea

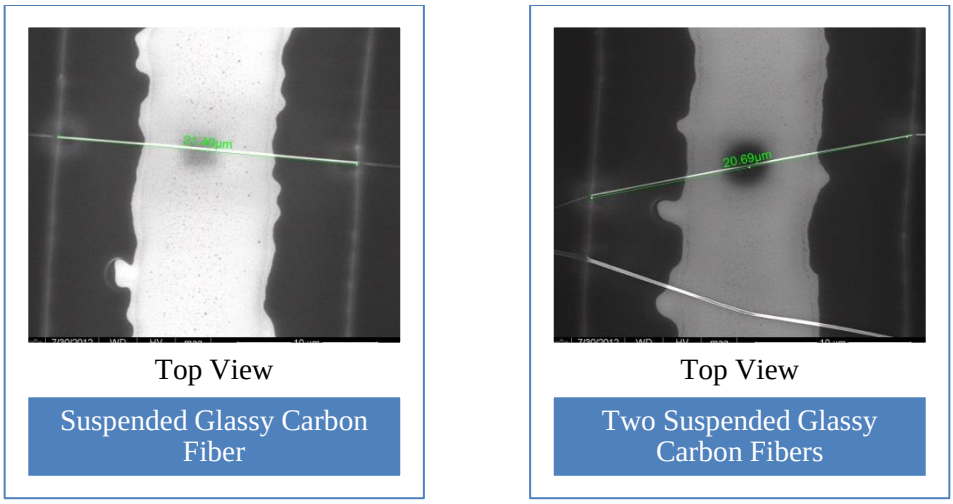

Figure 2.9: Nanofibers examples from FFE at UNIST in Korea

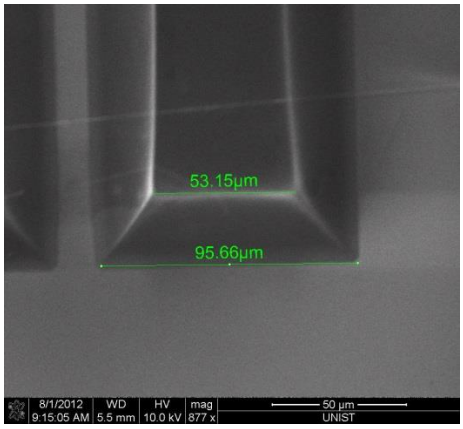

Figure 2.10: Support carbon structure for suspended glassy carbon nanofibers from FFE at UNIST in Korea

The author also had the opportunity to participate in the design and development of a FFE facility designed at the University of California, Irvine (UCI), during his research stay back in 2012. Figure 2.11 shows the design concept and the implemented system for the FFE facility performed at UCI.

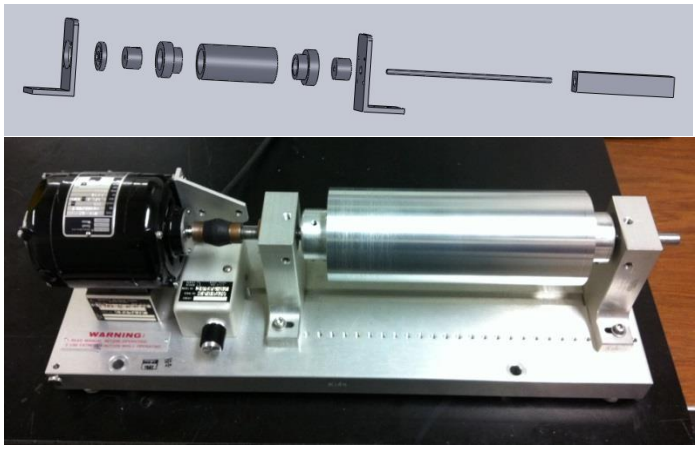

Figure 2.11: FFE design at UCI: Concept view (top) and real implemented facility (Bottom)

Other designs for FFE were also proposed at the Research Engineering Facilities from Instituto Tecnológico y de Estudios Superiores de Monterrey, campus Monterrey (ITESM). These designs were an initial effort to bring FFE into a research group that has the interest in joining together FFE and 3D printing for tissue engineering applications, using materials such as PCL. Figure 2.12, 2.13, and 2.14 show preliminary designs of the FFE facility at the Tecnológico de Monterrey Engineering Laboratories. They basically consist of a modular-interchangeable moving drum system. The design will have a DC motor (not shown) to rotate the drum, a micro-pump base for the polymer, and everything encased to protect it from the environment and have a better control of the ambient conditions. These designs were proposed based on previous experience of the author with FFE. The design illustrated in figure 2.12 has support lines that will allow the drum cylinder to move away or closer to the spinneret. This particular characteristic would allow dual operation mode of the device, this is from FFE to NFE.

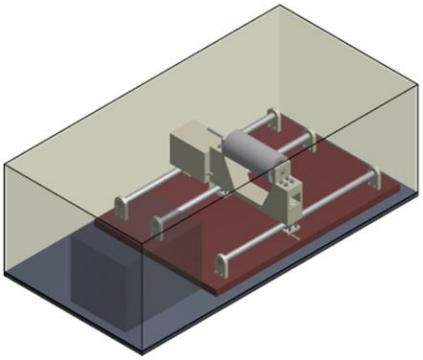

Figure 2.12: Encased rotating drum setup for FFE applications

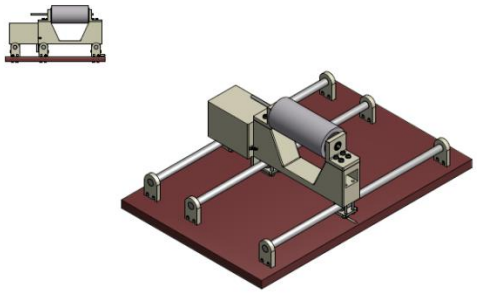

Figure 2.13: Basic rotating drum setup for FFE applications

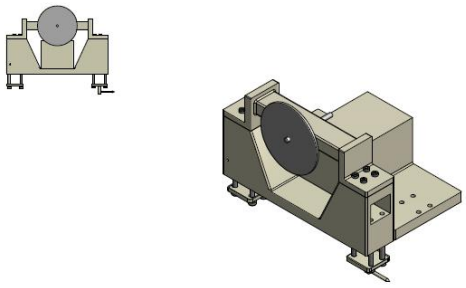

Figure 2.14: Planar-rotating drum for FFE applications

2.3.2 Electrospraying

In electrospraying, the fiber jet breaks into droplets instead of landing as a continuous fiber on the ground collector as in FFE. This effect is known as the Rayleigh instability effect [69]. This effect consists of having a thin unstable jet of liquid that breaks into droplets. Low-viscosity polymers will not pose much resistance against the Rayleigh instability effect and they will eventually break into small droplets, and sometimes, a pearls-on-a-string like formation can occur during electrospraying. This technique has found applications in the generation of fine aerosols for paints and coating, and also in the delivery of structural colors. [70].

2.3.3 Multijet electrospinning

This technique uses multiple spinnerets simultaneously to generate fibers that will be deposited on the ground collector. Care has to be taken in order to design the arrays in such a way that it will avoid electrostatic interference, otherwise a successful spinning process is difficult to obtain. An important consideration is that all the spinnerets need to be synchronized in order to produce homogeneous fibers. A finite element analysis (FEA) on the electric field distribution of the multijet electrospinning designs is usually needed to obtain a homogenous fiber result [71].

2.3.4 Coaxial electrospinning

In a coaxial electrospinning setup, two different solutions can be injected together in the spinneret. This allows obtaining a coaxial like fiber jet. If the two solutions are immiscible then a core/shell structure is usually observed. Some applications of coaxial electrospinning include drug delivery applications. The core from the coaxial fiber can also be removed by a selective solvent, thus leading to hollow fibers [71].

2.3.5 Emulsion electrospinning

Instead using a coaxial setup configuration to obtain fibers, an emulsion could be used in the electrospinning experiment. Core/shell or composite fibers can be created using emulsions and without modifying the spinneret. However, one of the main issues in emulsion electrospinning is that fibers are more difficult to obtain, when compared to other electrospinning techniques, due to the added complexity and hardware needed to generate the emulsion [71].

2.3.6 Melt electrospinning

Since many polymers are not easily electrospun due to their high viscosity, successful electrospinning cannot be obtained using all sorts of polymers in traditional electrospining. Therefore melt electrospinning is a good alternative for polymers having higher viscosities. In melt electrospinning the polymer is melt by heat, thus its viscosity and surface tension are reduced. The heat could come from resistance heating, circulating fluids, air heating/blowing or even from lasers. Using this technique eliminates the need for volatile solvents in the liquid solutions prepared for electrospinning [71].

2.3.7 Near field electrospinning

Near field electrospinning (NFE) is a ramification of the far field electrospinning (FFE) technique. The main difference between NFE and FFE is the distance from needle to collector electrode (closer for NFE and further away for FFE). For FFE, a distance of more than 10 cm is usually established between the needle and the collector. In comparison, a distance of a few millimeters is normally required for NFE. Another way to differentiate them is that in NFE the straight fiber jet stream is the only allowed portion from the jet stream, instead allowing the generation of the whip like stream jet as in FFE.

The samples of suspended nanofibers used in this study were generated using the NFE setup from the BioMEMS group at UCI. The polymer solution consisted of a mix of SU-8 2002 (MicroChem Corp), which is a photosensitive carbon precursor epoxy, and Poly (ethylene oxide)

(PEO) with 4,000,000 molecular weight (MW) in a concentration of 0.5 wt%. The addition of this low amount of PEO was enough to obtain a viscoelastic characteristic for the polymer to be continuously spun on a moving collector during electrospinning. However, due to the lack of conductivity from this polymer solution, the resulting electric field was not strong enough to impose and maintain a vertical jet during NFE. Therefore, salt was added to promote a higher accuracy of the patterning control. When salt is added to the solution, the charge induced in the polymer jet is increased, leading to a much better balance between the mechanical and electrostatic forces on the jet, which in turn translate into a much better polymer jet control [73]. The salt added to the solution was BF_4 (0.5 wt%), mainly because its stability even under a strong electric field. The final solution was stirred at 60^o C for 30-40 min until salt and PEO were completely dissolved.

The setup that was used to obtain the nanofibers is the same as the setup used by [73], and it consisted of a moving grounded collector, a needle, and a syringe with polymer solution. The polymer solution was pumped by an air pump, and a voltage of 350 V was used to overcome the polymer's surface tension.

Figure 2.15 shows a photograph of the UCI´s facility to perform the NFE. The picture illustrates: air pump, power supply, electronic control for the moving base, the moving base, the microscope, and at the far end the pyrolysis furnace. The only difference between the scheme mentioned in [73] and the approach used in this research is that only one single fiber was spun on the electrodes, instead of multiple fibers as is the case for the work of [73]. The samples were then cured under UV light, followed by a heat process (pyrolysis) at 900^o C in an inert N_2 environment to carbonize fibers and structures in one single step. Figure 2.16 describes the entire process using a block diagram.

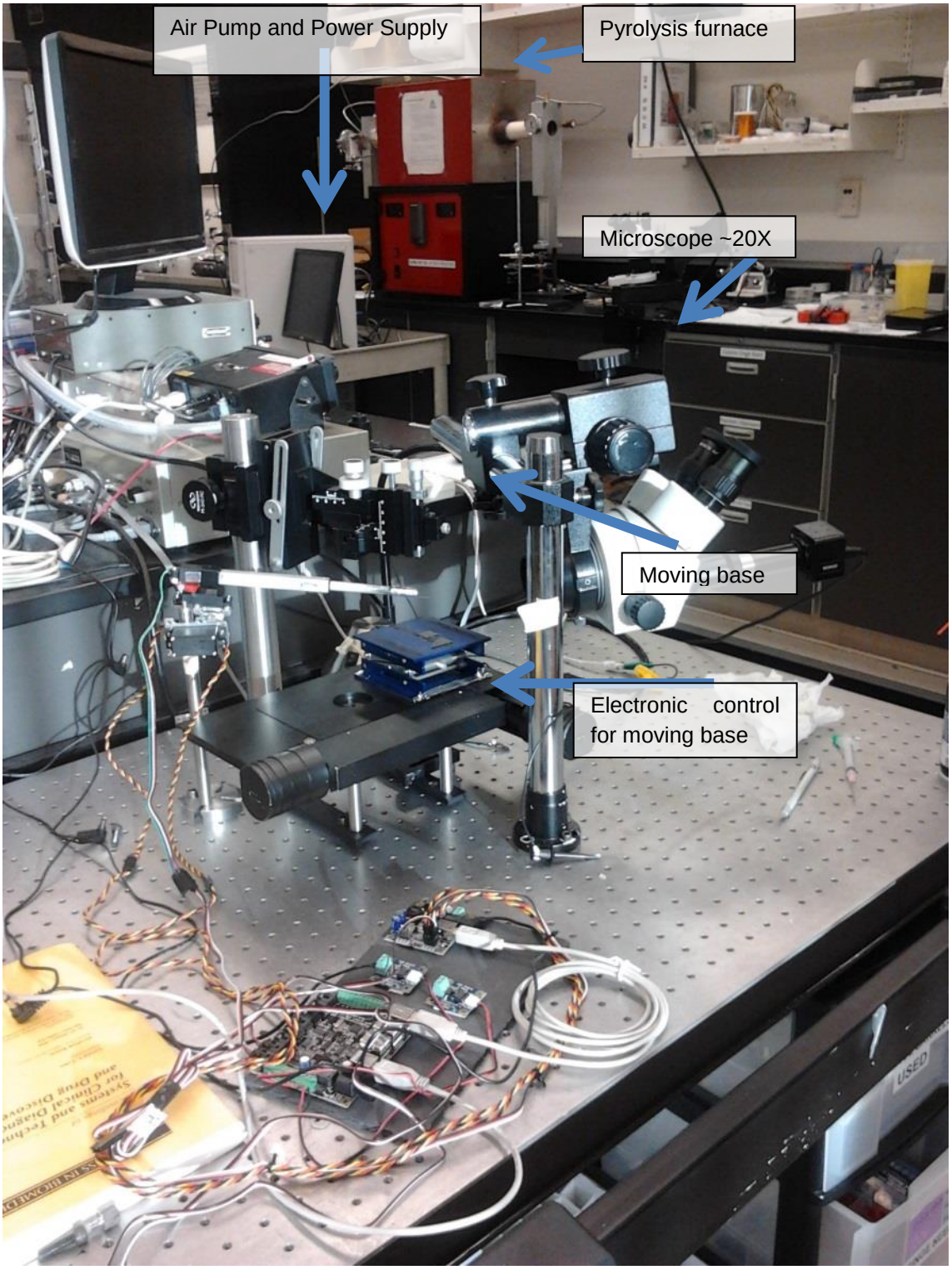

Figure 2.15: NFE setup from BioMEMS UCI's group

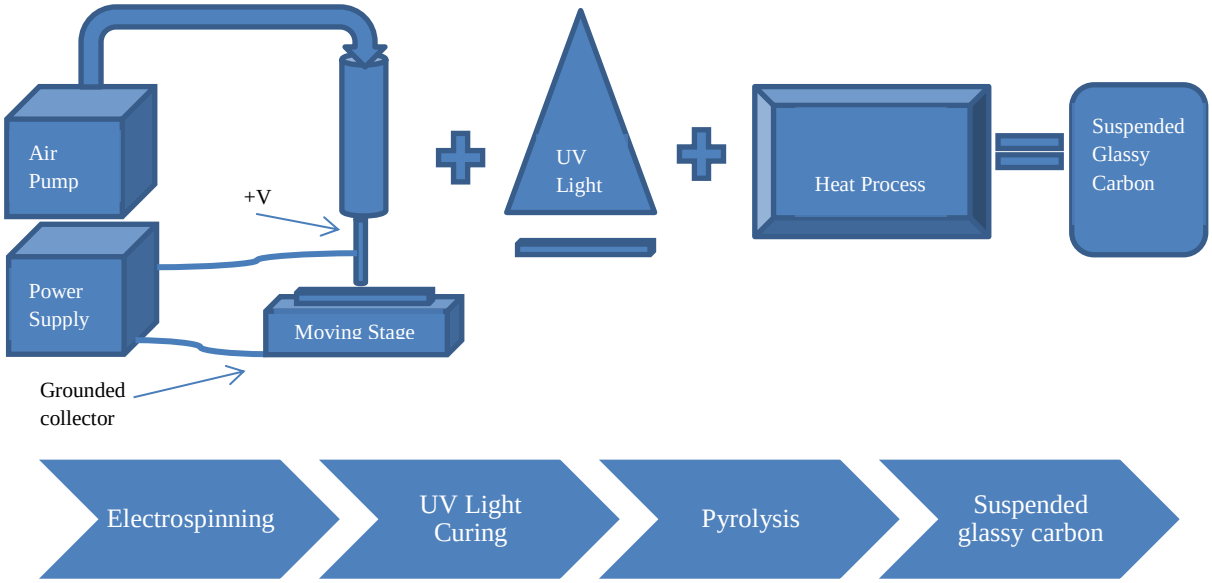

Figure 2.16 Nanofiber production process using NFE

2.4 Pyrolysis Process

The electrode structures and deposited fibers are converted from polymer solutions into glassy carbon using a heating process called pyrolysis. This heating process has to be carefully controlled in order to obtain the desired results. The temperature from the pyrolysis furnace is incremented in a controlled manner by segments. As depicted in figure 2.18, the temperature is first maintained at 20 Celsius for 90 minutes then it is raised to 700 Celsius for 90 minutes. In the next programmed segment, the temperature is raised again to 900 Celsius and left there for 600 minutes, then it is brought down to room temperature. The increase of temperature is programmed to be around 10 Celsius degrees per minute.

There are two main device options to control the pyrolysis process. One uses a vacuum pump to create an inert environment inside the pyrolysis chamber. The other option uses nitrogen to fill in the chamber with an inert gas. The samples are placed inside a quartz tube, and then the heat treatment process can start on the pyrolysis furnace. The figure 2.17 shows a sequential diagram of the pyrolysis process.

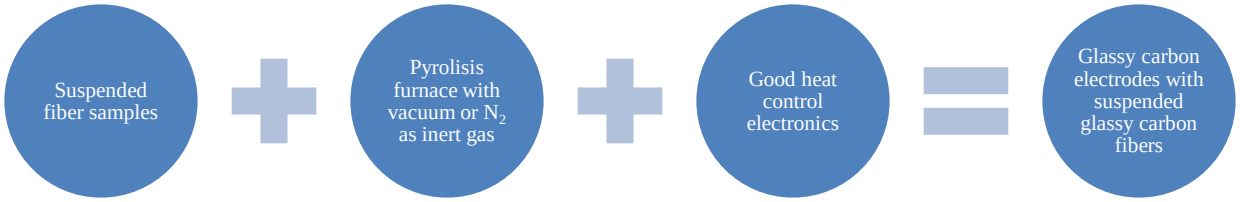

Figure 2.17: Pyrolysis process

The pyrolysis furnace used at the BioMEMS group at UCI uses N_2 and it was shown in the picture that appears in figure 2.15. Figure 2.18 shows the control program parameters used to set up the pyrolysis furnace.

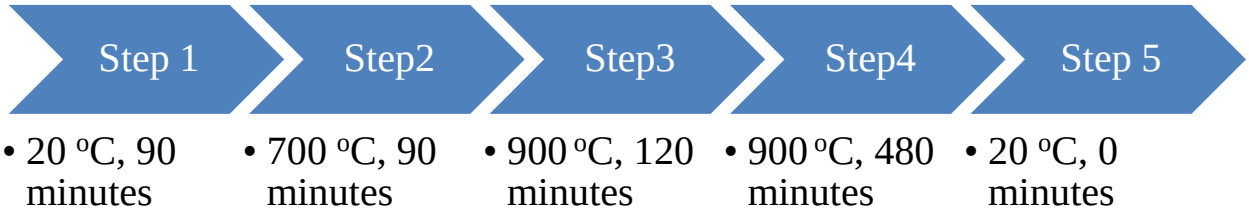

Figure 2.18: Steps showing the Pyrolysis control parameters

2.5 Summary

This chapter describes the fundamental processes to fabricate nanofiber structures and their associated support structure. Three processes are discussed:

1. Support electrode development using photolithography
2. Electrospinning methods which include FFE and NFE as the basis for the nanofiber sample fabrication in this research project.
3. Pyrolysis process to consolidate the finished fiber.

The following chapters will focus on the characterization methodologies, applications, modeling and experimentation to test the nanofibers.

Chapter 3

Electromigration and Joule Heating

This chapter describes the fundamental principles of electromigration (EM), and its use as a companion physical phenomenon to induce nanoconstrictions and nanogaps in metallic nanowires. Moreover, Joule Heating effects are described as a phenomenon to obtain the same nanoconstrictions and nanogaps on suspended carbon nanofibers. A brief description of carbon as the material from which the nanofibers are made is also provided as well as some of its properties. In addition, selected techniques to shape carbon structures are mentioned. Finally, an overall description of nanofiber applications is also given.

3.1 Introduction

Electromigration (EM) is defined as the gradual displacement of metal atoms in a material when the current density is sufficiently high (above 10^6 A/cm^2), that causes the material atoms to drift in the direction of the electron flow [7]. The number of atoms passing through a specific cross sectional area per unit time is known as the atomic flux. A high current density can greatly accelerate the EM degradation of the material. When the current flows through the nanostructure, heat is generated due to Joule Heating and this increases the temperature of the material.

Historically, EM has been the major source for failure in integrated circuits (IC). This is particularly true in nanometer sized silicon technology. However, as mentioned at the beginning of this chapter, EM can also be used in a more constructive way. When properly controlled, EM can be used to generate nanocontrictions and nanogaps on metallic nanowires [7-43]; and graphene sheets [30].

On the other hand, carbon nanofibers are immune to electromigration [74]. The breakdown phenomenon observed on carbon nanofibers is mainly due to Joule heating which can be used on

suspended carbon nanowires to induce nanoconstrictions, nanogaps and/or mechanical deformations on the nanofibers.

Joule heating is also known as ohmic heating or resistive heating. This phenomenon occurs when an electric current goes throughout a conductor object while releasing heat. The heat released is proportional to the square of the current sent throughout the object (I^2R). Since the nanofibers used in this research have some finite electrical resistance, flowing a current through them generate heat that eventually modify their internal structure if the heat becomes high enough.

3.2 Electromigration in Metals

When EM is induced on a metallic wire, it can cause failure of the material. This failure could result in nanoconstrictions, or even in the formation of nanometric gaps between the metallic wires. The initially single metallic wire could therefore be shaped into a two nano-electrode configuration. According to [51], both the shape and size of the final nanometric gap depend on variables such as the metal´s grain structure and boundary distribution. Metals most often used for the fabrication of nanowires are gold, sodium [52], platinum, and palladium.

Depending upon the application, there are well established techniques to fabricate metallic nanowires. Such techniques include Electron Beam Lithography (e-beam), and Ion Beam Induced Deposition. As mentioned in chapter 2, the nanofiber samples used in this research are composed by glassy carbon, and they are fabricated by either FFE or NFE.

3.3 Nanocontrictions and Nanogaps by Electromigration

As mentioned previously, a method to generate nanoconstrictions consists of controlling the EM degradation. Thus, by passing a large enough current through a nanowire, a nanoconstriction or a mechanical rupture can be generated depending on how well this control action is exerted. This procedure is reported for metal nanowires [1-49] and for graphene sheets [30].

Another method consists of using vacuum to enhance the control operating conditions in EM, such that metal nanowire nanoconstrictions can efficiently be generated. Rupture of nanowires depends on the current density needed to induce a material breakdown. Thus, material and geometric properties of the nanowires have to be taken into account when predicting the rupture point for the nanofibers. These issues, applied to glassy carbon nanofibers, will be further described in chapter 6, Joule heating model, and chapter 8, experimental setup design.

3.4 Nanocontrictions and Nanogaps by Joule Heating

Figure 3.1 shows the first experiment where a successful nanofiber constriction was generated using our first nanofiber sample set. Unless otherwise mentioned, this and subsequent SEM pictures that appear in this dissertation come from nanofiber samples fabricated at UCI and observed with the SEM from Universidad de Monterrey (UDEM).

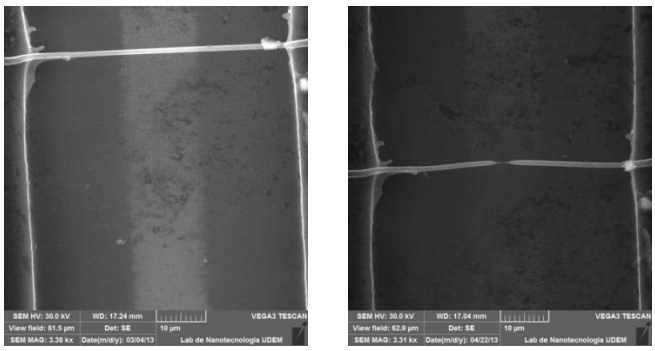

Figure 3.1: Before (left) and after (right) images of a nanoconstriction

The figure 3.2 shows a zoom-in view from the same sample depicted in figure 3.1. From figure 3.2, even though the fiber is apparently broken, by measurement of electrical parameters proves that there is still an electrical connection. The electrical readings obtained from that experiment suggests that the fiber is still making electrical contact, since it still shows the flow of a small electrical current and its resistance increased from 4.5 kΩ to368 kΩ. Technical limitations on the SEM used to take the images, does not allow obtaining a clearer image when the minimum feature size goes below ~100 nm.

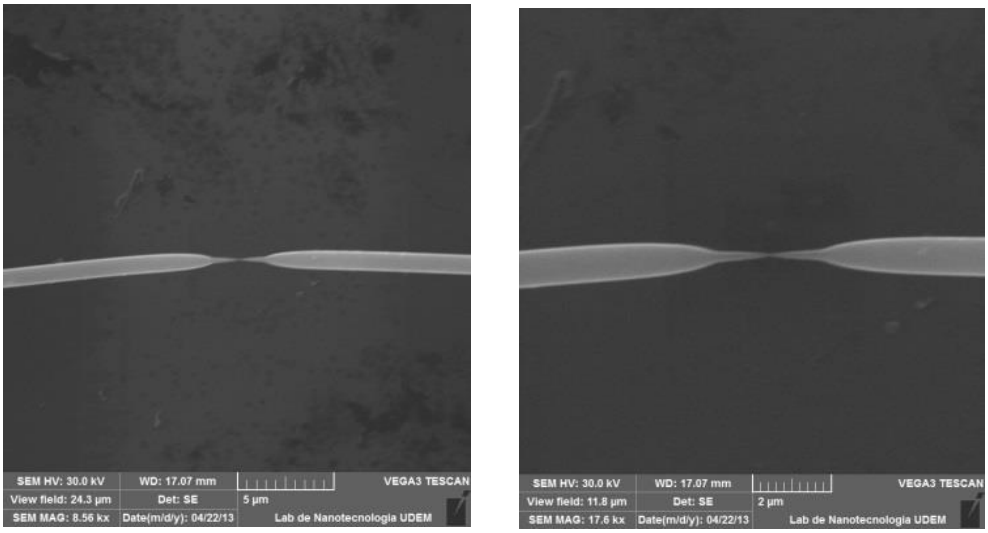

Figure 3.2: Zoom-in view from first obtained nanoconstriction

Joule Heating can also be used to generate controlled nanogaps. Although the main objective of this manuscript is to electrically characterize glassy carbon nanofibers, a particular objective is to consider using the methodology to generate nanogaps by controlling the breakdown phenomena.

Figure 3.3 shows a "before and after" image from the first nanogap observed during the development of the experiments for this manuscript. Figure 3.4 illustrates a zoom-in view of the same sample as in figure 3.3. Electrical recording signals show that no current was circulating throughout the fiber before the end of the experiment. Therefore, visual (SEM image) and electrical signal confirmation for the nanogap were obtained.

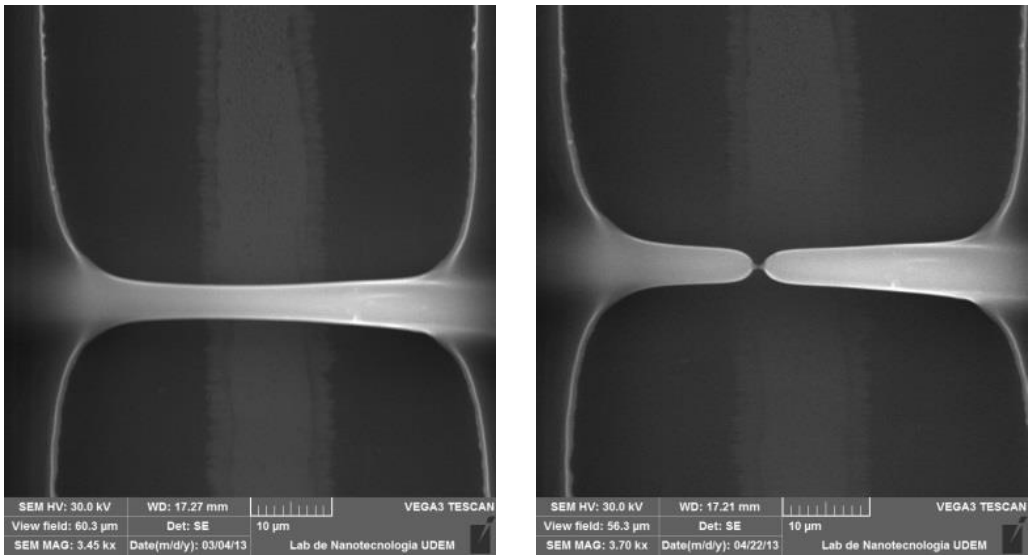

Figure 3.3: Before and after image from first observed nanogap

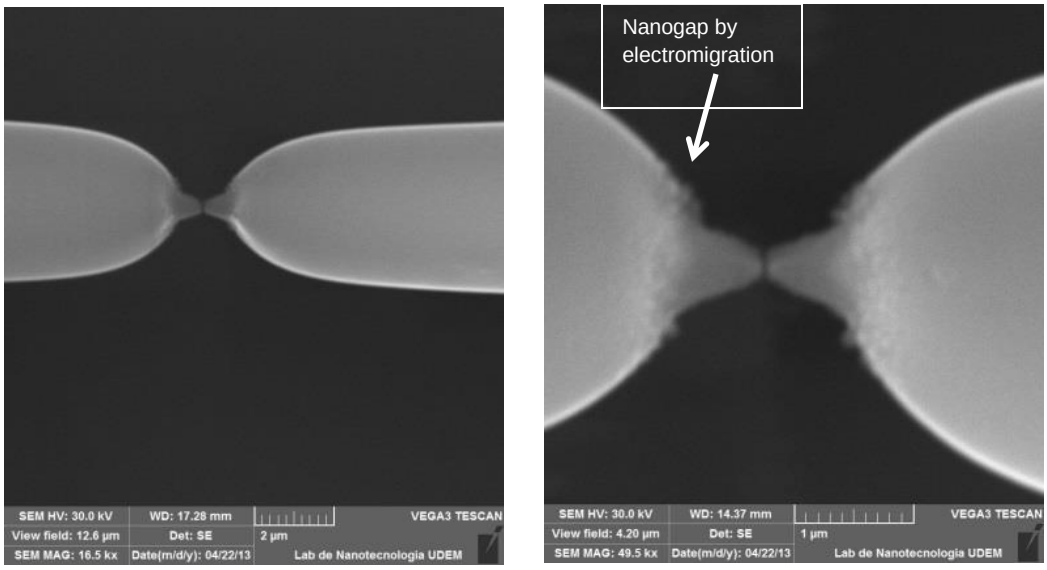

Figure 3.4: Zoom-in view for first observed nanogap

3.4.1 Molecular electronics

In this subsection it will be briefly described the nanotechnology area of molecular electronics, and its basic components as well as the importance of generating nanogaps.

Microfabrication is approaching the limits for silicon based technology (microelectronics). Alternative approaches to overcome that limit are being investigated. One of such approaches is molecular electronics, which in turn could use molecules and nanogaps in some of their designs. Therefore, the generation of nanogaps allows moving forward into the area of molecular electronics. In molecular electronics, single molecules, or small groups of molecules are used as components in several applications (i.e. electronics). Nanogaps made from conductive materials could be the basic structural electrode unit for new transistors, sensors, and circuits designs. The area of molecular electronics has been improved recently due to an enhanced ability to fabricate contacts and gaps of nanometer size. A small number of molecules can be accommodated in between the nanogaps of nanometer sized electrodes. Figure 3.5 illustrates the concept of a device where a source/drain pair is connected with a nanowire having a middle nanogap. The nanogap can be filled up with a molecule in case of a biosensor or with a nanosphere in case of single electron tunneling device (SETD).

Molecular devices require of at least a nanoscale aperture (nanogap) and a way to arrange molecules within it. There are two main methods to obtain nanogaps: The first known as break junction technique, the second known as electromigration (for metal electrodes). These two methods provide a base structure for certain molecules to self-assembly on its metallic surface. For non-metals, such as carbon fibers, Joule heating instead of electromigration is the phenomenon by which nanogaps are obtained (this work). Self-assembling molecules on non-metallic surfaces could be used for carbon nanogaps.

The break-junction technique requires a thin wire or fiber fabricated on top of a flexible substrate. Flexibles substrates can be made from i.e. polyimide. After combining the fiber and flexible substrate the wire is notched (i.e. e-beam lithography) to facilitate breakage. Finally, the fiber is broken by bending the flexible substrate in a controlled manner. Bending of the substrate and control of the nanogap can be accomplished by a piezoelectric actuator (i.e. ceramic actuator) positioned under the substrate.

Electromigration, as explained in section 3.1 and 3.2, is the physical phenomenon by which metallic nanogaps can be obtained. The amount of electrical current is controlled to generate a nanogap. The conductance or resistance of the wire is monitored to provide a control loop during nanogap formation. When the current density is small, nothing changes. The nanogap is formed

once the current density becomes large enough for the metal ions to be moved by electromigration (i.e. a change in conductance or resistance is detected). Individual or several molecules self-assembled on the nanogap could be also electrically studied using these two methodologies.

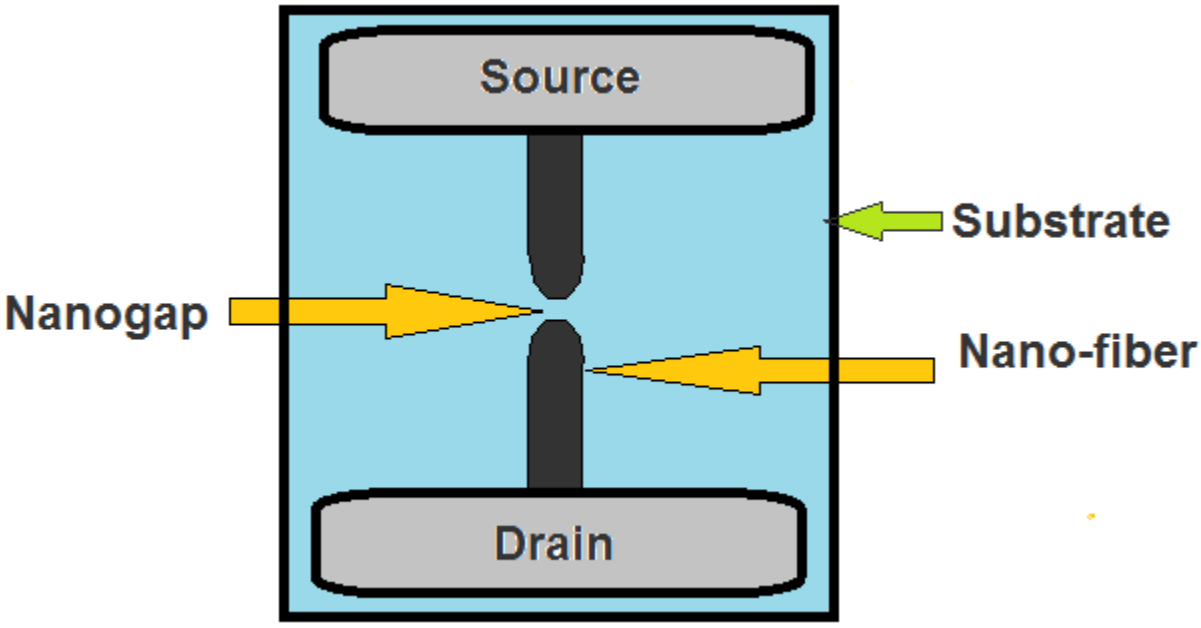

Figure 3.5: Conceptual nano-gap structure to build a molecular device

3.5 Carbon

Carbon has several allotropes or different physical forms in which this element can exist. Some of the allotropes of carbon include graphite, diamond, and amorphous carbon. The allotropic form defines the carbon's physical properties (intrinsic properties). Examples of these include:

1. Diamond, the hardest natural occurring material known, which has a very low electrical conductivity. The internal crystal structure of diamond presents a bond between a set of four carbon atoms with other four carbon atoms. Therefore no free electron is left to conduct electricity through the conduction energy band.
2. Graphite, which is a soft material which has a completely different crystal structure which provides a very good current conduction. In graphite, each carbon atom is covalently bonded to only three neighboring carbon atoms, forming layers (planes) of hexagonal network as shown in the figure 3.6. The fourth valence electron of each carbon atom remains free enabling its easy flow in the direction of the planes in the graphite material. This free electron is the reason why graphite has a higher electrical conductivity than diamond.

Furthermore, carbon is the basic building block of nature; therefore it is by definition bio-compatible. Carbon with its many forms has found many possible applications including, but not limited to, biosensors, implantable devices, chemical sensors, next generation transistors (cross-linked fibers, carbon nanotubes), and batteries. Carbon also has important applications in the BioMEMS field.

Two microfabrication processes available to produce carbon structures include Focus Ion Beam (FIB) and Reactive Ion Etching (RIE). However, these techniques are time consuming and expensive. Screen printing is yet another option to microfabricate structures based on carbon. However, screen printing has a poor repeatability and the resulting devices may have varying properties between one another.

The carbon structures used in this research are fabricated using a process called Carbon MEMS (C-MEMS). Here the initial procedure is to construct the underlying carbon electrodes to support the fibers, as mentioned in chapter 2. C-MEMS process has been refined by professor Madou's BioMEMS group at UCI. It allows obtaining well defined carbon structures. Reviewing the process explained in chapter 2, a photoresist is patterned by photolithography and then passed through a pyrolysis process at high temperatures (around 900^{o}) in an inert environment (oxygen free). Tuning of the photolithography conditions provide good results in the final

carbon structures. The structures obtained by the C-MEMS process can have a wide range of geometries, as well as resistivity and mechanical properties.

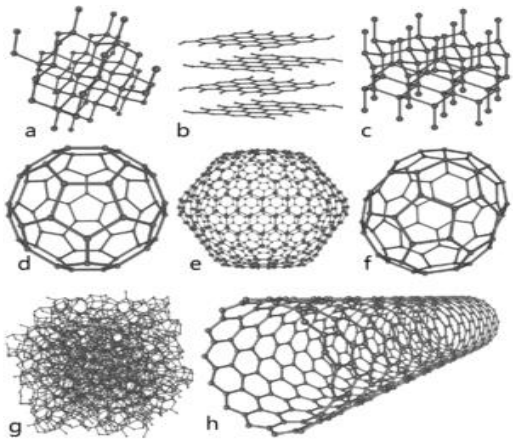

Figure 3.6: Carbon allotropes

Figure 3.6 shows eight allotropes of carbon: a) Diamond, b) Graphite, c) Lonsdaleite, d) C_{60}, e) C_{540}, f) C_{70}, g) Amorphous carbon, and h) Single-walled carbon nanotube. The allotropes of carbon, besides diamond and graphite, are briefly explained in the next lines:

c) Lonsdaleite (also known as hexagonal diamond) forms when meteorites containing graphite strike the Earth. This transformation occurs due to the great heat and stress of the meteoric impact which can transform graphite into diamond but retaining its graphite hexagonal lattice.

d) C_{60} or Buckminsterfullerene is a spherical fullerene molecule. It is the most common fullerene molecule that naturally occurs on Earth. The discovery of this molecule has initiated to the exploration of fullerenes.

e) C_{540} similar to C_{60} but with 540 carbon atoms forming this molecule. It has several layers also known in general as bucky onions.

f) C_{70} similar to C_{60} but composed of 70 Carbon atoms instead of 60 Carbon atoms. It has a Carbon atom at the vertices of each polygon and a bond along each polygon edge. Laser evaporation of graphite was used to obtain this Carbon structure.

g) Amorphous carbon (also known as glassy carbon) is formed when a material (such as a polymer) containing carbon is burnt in an inert environment (i.e. vacuum furnace or a N_2 filled furnace chamber).

h) Single walled carbon nanotubes (SWNT) are formed from a single sheet of graphene. It has a cylindrical shape. SWNT can be further divided into zigzag, armchair, or chiral nanotubes. SWNT can show metallic or semiconducting behavior.

3.5.1 Glassy carbon

Glassy carbon, as its name implies, has a glassy-like appearance, and it can be obtained after pyrolysis of several types of polymers. The polymer (also called precursor) is then heat treated to obtain the glassy carbon. Glassy carbon is hard (very unlike graphite) and brittle [75]. Glassy carbon electrodes have a wide electrochemical stability window, and low cost. Glassy carbon nanofibers are used as the main case in point in the development of experiments, observations, modeling and analysis in this research.

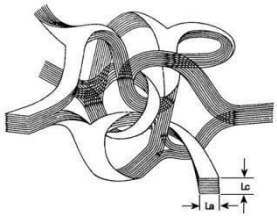

Figure 3.7: Glassy carbon structure, from [75]

3.5.2 Photoresist and pyrolysis

A photoresist like Microchem's SU-8 (or a combination) is used as the polymer in the nanofiber support structure and to produce the nanofiber itself which will eventually pass

through a pyrolysis process to be converted into glassy carbon structure. SU-8 is a negative epoxy photoresist that is optically transparent, and can react when exposed to near UV (365 nm) radiation. Once cured, it is very resistant to solvents, acids and bases and has an excellent thermal and mechanical stability.

A furnace specially designed for the pyrolysis processes is used. There are mainly two types of pyrolysis furnaces, one that uses vacuum and the other that uses nitrogen as an inert environment. During the process, care has to be taken to slowly ramp up the temperature to 900^{o} Celsius degrees, although the upper temperature limit may vary from reference to reference work, depending on the research objectives and available furnace capabilities. For the C-MEMS process described in 3.5, the samples are pyrolyzed in a N_2 atmosphere (oxygen free), in a special furnace at around 700^{o} C for about 90 minutes and then heat treated up to 900^{o} C. The heating rate used is around 10^{o}C/min. Then the heater is turned off, and the samples are cooled down to room temperature. The pyrolysis furnace needs a good temperature control to achieve the results for the samples used in this research.

The carbon that results from this pyrolysis process is supposed to be glassy carbon due to its amorphous look. The carbon structures after pyrolysis shrunk from their original size but they retain the same shape. This effect is used in advantage to generate tension on the suspended fibers. The shrinking effect is more pronounced at the top of the structures. The shrinking at the base of the structures is less pronounced due to the better adhesion of the photoresist to the substrate. Once the photoresist passes the pyrolysis process for the first time, it will not shrink noticeable after a second pyrolysis step. This same idea of C-MEMS process and pyrolysis can be further extended to generate several layers of carbon material.

3.5.3 Glassy carbon electrical/mechanical/thermal properties

Table 3.1 summarizes the electrical/mechanical/thermal properties of glassy carbon as reported in [61]. Although the polymer used to obtain the suspended glassy carbon nanofibers in this manuscript is different from just a SU-8 XXXX polymer, table 3.1 gives an overall view of the properties of glassy carbon as reported by several other research groups. Therefore, it is a good

starting point for our model evaluations (Chapter 4). Table 3.2 compares between some properties of glassy carbon nanofibers and carbon nanotubes just as a comparison point.

Table 3.1: Properties of glassy carbon

Glassy carbon	SU-1300	SU-2000	SU-2500
Density (g/cm^3)	1.61	1.58	1.55
c (nm)	0.72	0.707	0.695
L_c (nm)	1.5	1.7	2.4
Strength (MPa): "Bending"	107-127	130-160	70-100
Modulus of elasticity (GPa)	25.3-28.8	27.3-28.9	25-30
Resistivity (μΩ.m)	45-50	40-43	38-41
Thermal conductivity ($W/m.^oK$)	3.7-4.5	5.2-6.4	6.4-7.5

In table 3.1:

a) Density of any substance is its mass per unit volume.
b) c (nm) refers to intraplanar microcrystalline size.
c) Lc(nm) refers to interplanar microcrystalline size.
d) Strength (MPa) refers to the bending stress of the material. It defines the bending moment of failure stress in bending of a material when subjected to a bending load. The bending strength value represents the value at which the material deforms permanently after a bending moment is applied to it.
e) Modulus of elasticity (GPa) is also known as Young Modulus. It is the ratio of tress to strain. This parameter is useful to describe elastic properties of linear objects such as wires that are stretched or compressed.

f) Resistivity (μΩ.m) is a measure of how much resistance the material possesses to the flow of electrons. Temperature range of 20 ^{o}C to 500 ^{o}C.

g) Thermal conductivity (W/m^{o}K) refers to the property of materials to conduct heat. A material with high thermal conductivity value means that the material conducts heat rapidly compared to a material with lower thermal conductivity. Temperature range of 20 ^{o}C to 500 ^{o}C.

Table 3.2: Comparison between glassy carbon nanofibers and carbon nanotubes

	Glassy Carbon nanofibers	Carbon nanotubes
Average diameter size	80 nm - 4μm	1.2-1.4 nm
Density	1.49 – 1.61 g/cm^3	1.33-1.40 g/cm^3
Tensile Strength	33 – 75 GPa	~150 GPa
Young's Modulus	25.3 – 30 GPa	1 – 6 TPa
Thermal conductivity	3.7 – 7.5 W/m^{o}K	~3000 W/m^{o}K
Electrical resistivity	6000-14000 μΩ.cm	~100 μΩ.cm
Cost	~$10 usd/gr or less	~$100 usd/gr

3.6 Nanofibers and Their Applications

This section presents some nanofiber applications in different areas of engineering and technology. The nanofiber related applications include: filtration, affinity membranes, tissue engineering scaffolds, release control, sensors, energy conversion and storage, reinforcement and molecular electronics. Moreover, some research work performed at the medical school laboratory of the Tecnológico de Monterrey is illustrated where commercial aligned poly caprolactone nanofibers were used to orient stem cell alignment.

Nanofibers are basically fibers with a diameter ranging from below 1 μm to just a few nanometers. In this research, the method used to obtain nanofibers is electrospinning, followed by a heat treatment; both were explained in Chapter 2.

3.6.1 Applications

A partial list of nanofiber applications which have leading roles in technology are: filtration, affinity membranes, tissue engineering scaffolds, wound healing, release control, catalyst and enzyme carriers, sensors, energy conversion and storage, reinforcement of materials, and sound absorption [3]. The research in C-MEMS glassy carbon nanofibers, however, will have much more impact in solutions regarding sensor devices, and tissue engineering. Nevertheless, key role applications are described to have a broad idea of their importance in different fields of engineering and technology.

1. **Filtration**. When fibers are spun in a non-controlled manner, a fiber mat is obtained. This fiber mat could function as an air or liquid filter. These filters can remove pollutants from air or water. The removal of particles is determined by several factors. For example, larger particles could be blocked on the surface of the fiber mat, and smaller particles that may pass the filter surface could still be collected by static electrical attraction. Thus the filter physical structure (fiber diameter and intermesh distance, matrix structure, thickness of the mat, pore size, etc.) influences the filtration efficiency of the fiber mat.

2. **Affinity membranes**. Nanofibers can also be functionalized via incorporation of functionalized materials on the polymer solution, or via surface chemistry and coating techniques. Functionalizing of membranes may be useful to creating self-assembled layers on the fibers.

3. **Tissue engineering scaffolds**. This is a relatively recent area that has been paid a lot of attention due to their promise to general human health and recovery techniques. It

involves a wide range of disciplines due to its use of living cells and their manipulation to develop biological substitutes for implantation into the human body. These implantations intend to aid in tissue repair or tissue regeneration, like muscle, cartilage, bone, and so on. Tissue engineering also aims for the replacement, maintenance or enhancement of the function of a particular tissue or even complete organs. In order to make this a reality, one needs to combine efforts from different technologies, such as cell development, scaffold construction, and *in vivo* integration of the cell-scaffold combination. Regarding the scaffold, it needs to have the right design parameters, since it has been shown that depending on the designs parameters like material and fiber diameter, different results could be obtained [76-116]. For example, scaffolds intended to be used as supports for cell development should have a high porosity, high surface area, be biodegradable, have structural integrity to keep cell development in place, and most importantly be non-toxic and biocompatible for the particular cells used. If all the aforementioned requirements are fulfilled, then there will be a high probability to promote cell adhesion, proliferation, migration, and differentiated cell function (assuming stem cells are used). Nanofiber mats, can be designed in such a way that they would mimic the extracellular matrix (ECM), making them appealable to the cell culture. When one controls the orientation of the nanofibers mats (i.e. aligned nanofibers), it provides for topographic cues that will direct cell adhesion, spreading and development. [107]

4. **Release control**. In a controlled release system, the idea is that the active substance has to be loaded into a carrier or device, and then released at predefined and controlled intervals. This is the basic work principle on pills, the pill being the device/carrier and the powder inside being the active substance. Nanofibers can also be used as carriers for drug delivery. Particularly, electrospun nanofibers make it easier to load drugs on the polymer solution before being spun, and the high electric field applied in electrospinning have shown little influence on drug activity as reported elsewhere [108]. Nanofibers made from biodegradable polymers like PLA, PCL, poly D-lactide (PDLA), PLLA, PLGA, PVA, PEG, and PEO have been studied as possible drug delivery nanofibers for controlled drug release.

5. **Sensor devices**. They are almost in every monitoring, and control process we can imagine. Sensors are useful to detect chemicals in the environment, process control from industry to research, medical diagnosis, and even in defense applications. When nanofibers are fabricated (i.e. by electrospinning) one could obtain dimensions from nanometers to micrometers. Some of the characteristics of a good sensor are that it should have a small dimension, low fabrication cost, and preferably multiple functions aside from having a high sensitivity, good selectivity and reliability. Most of those characteristics can be met by electrospun fibers. High sensitivity and a fast response compel the sensor to possess a large specific surface area, and a highly porous structure. Again, these characteristics can be met by electrospun glassy carbon nanofibers. Several different approaches have been used by other groups to provide to the nanofibers with a sensing capability. For example, by adding sensing molecules into the fibers, or by applying a sensing material on the nanofibers surface via coating or grafting techniques. In fact, coating is one promising technique that could be used with the glassy carbon nanofibers studied during this work, in order to build a complete gas sensor. Electrical conductivity is also a very important property for a sensor device. In the case of glassy carbon as a material, it possesses a good electrical conductivity, again providing for a good material of choice to build sensors.

6. **Energy conversion and storage**. Normally, a battery has an element which has a porous structure of its own. A porous separator between the two terminals (positive and negative) of the battery can effectively stop the short circuit, but still freely allow for the exchange of ions. Therefore, a porous membrane of nanofibers with well interconnected pores, a suitable mechanical strength and high electrochemical stability could be a potential candidate as a battery porous separator.

7. **Reinforcement**. Nanofibers have been also reported to be able to reinforce different materials. Both, stiffness and strength of some reinforced materials can be considerably increased by such approach. [117]

8. **Molecular electronics**. As explained previously, fibers find interesting applications in the field of molecular electronics. Controlled nanogaps on fibers and a few molecules bridging that gap define the basics of a molecular device. Also, a new type of structure: the crossed nanowire arrays; can be used as the basic unit for the construction of memory and processor circuits. These crossed nanowires could possess a separation of a few nanometers, close to the size of molecules [118].

3.6.2 Stem cell orientation on aligned nanofibers

An experiment pertaining mesenchymal stem cells (MSC) and their adhesion and orientation along aligned nanofibers was performed. This experiment was conducted at the medical school of ITESM. The cells used for this study were Wistar rat mesenchymal stem cells. The objective was to evaluate their adhesion, proliferation and orientation along aligned fibers. The fibers are commercially available poly-caprolactone (PCL) nanofibers. The fibers have a size of ~750 nm and are aligned in one direction. Figure 3.8 shows images from MSC when cultured on a normal Petri dish. Observe that the cells are not preferably orientated in any direction. Figures 3.9 and 3.10 show fluorescence images of the results from this study in where aligned nanofibers were used as the substrate for cell adhesion and proliferation. Observe that the cells are aligned in the fiber orientation. The bright part of the cells is the nucleus while the rest is the cytoplasm. These results open the idea of using aligned carbon fibers as a substrate for future studies of MSC in where electrical stimulation is made possible.

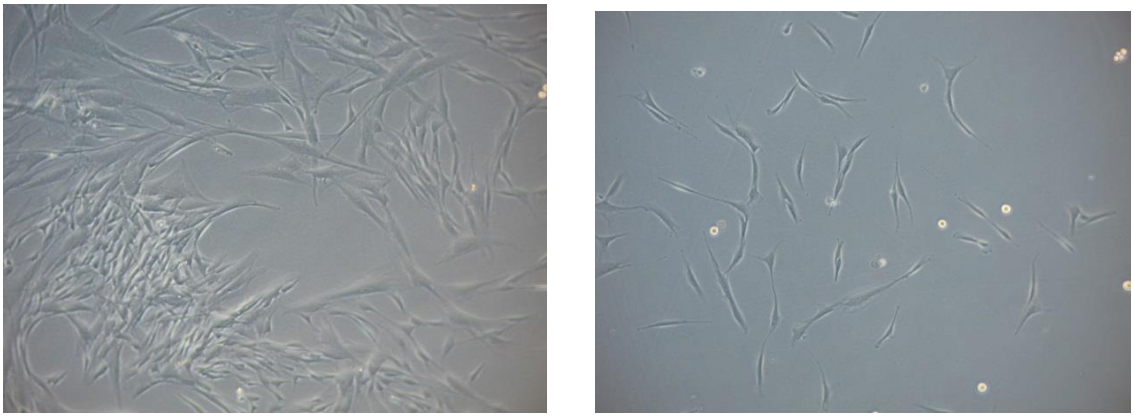

Figure 3.8 Stem cells cultured on a normal Petri dish

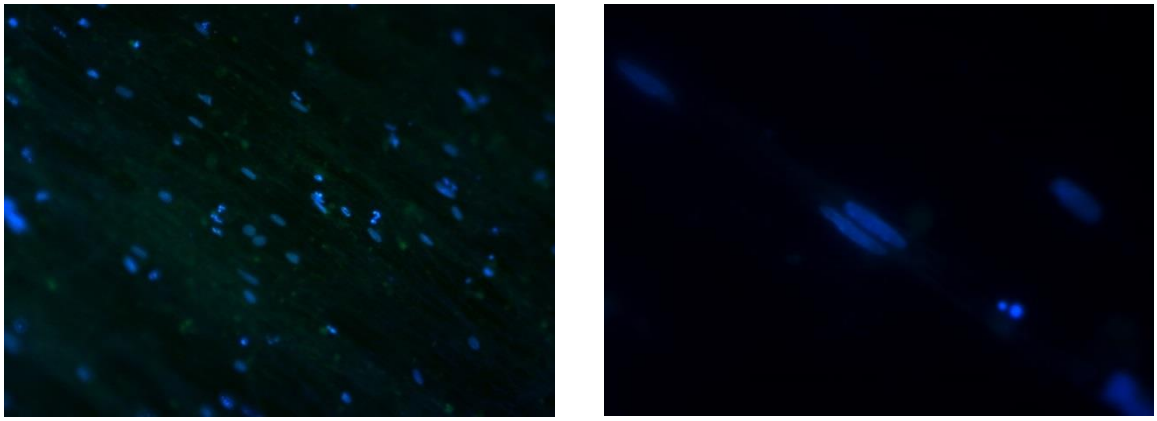

Figure 3.9 Stem cells cultured on aligned PCL nanofibers

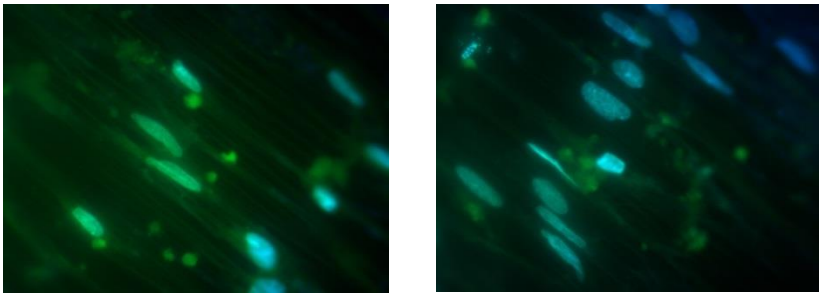

Figure 3.10 Stem cells cultured on aligned PCL nanofibers

3.7 Summary

This chapter discussed the EM phenomena and Joule heating for nanowires. The EM degradation phenomenon has been studied for years to develop nanogaps and nanostrictions in metal microstructures. Even though the glassy carbon nanofibers are immune to this phenomena, there are some fundamental concepts in metal EM that are well suited for their analysis in very thin glassy carbon nanostrictions. The Joule heating phenomena is fundamental in modeling the glassy fiber nanofibers to predict the formation of nanogaps and nanostrictions. A very detailed control of current through the fiber is necessary to obtain satisfactory results over nanofiber samples. Finally, an insight to possibilities in the field of molecular electronics is described where the conceptual view of applications of nanowires and nanogaps are presented.

In this chapter it was also discussed carbon as a working material, some of its physical and electrical properties as well as some of its allotropes. The process by which polymers are converted into amorphous carbon was also reviewed. A brief discussion on C-MEMS processes was also introduced to generate microstructures useful for these work objectives. Finally, possible nanofiber applications were described. One of such application (tissue engineering) describes a side research work that the author of this manuscript had the opportunity to complete. Such work included the study of stem cell orientation along PCL aligned nanofibers. Chapter 4 will build the mathematical model for the Joule heating phenomenon in order to predict temperatures changes in the nanofiber.

Chapter 4

Joule Heating Model

Carbon nanowires which are suspended between two carbon electrode walls are studied by applying a DC voltage in a controlled manner. The applied voltage induces a DC current that flows through the nanostructure. As explained in chapter 3, when a DC current is sent through a nanowire, it directly heats the wire and generates a heat exchange between the nanostructure and the control volume. This effect, known as “Joule Heating”, generates the breakdown phenomena on the carbon nanowires. What is the current required to generate a nanoconstriction or a nanogap on a carbon nanowire? What is the temperature that the nanowire reaches when exposed to such DC current levels? Those questions could be addressed using a mathematical model that relates the temperature to the control current flowed through the nanostructure. This chapter proposes a mathematical model of the heat transfer phenomenon having the temperature as the state variable in the nanofiber. Also some preliminary simulations of this model are discussed in order to prepare the way for reaching the experimental phases of this research in the following two chapters.

4.1 Heat Transfer Joule Heating Model Equations

An electro-thermal model, as proposed in [65] and [66], is used to simulate the heat exchange mechanism in the nanostructure. This model considers heat conduction on thin wires due to DC current flowing in the nanostructure. The suspended wires have a length “L”, and cross section “A” as shown in the figure 4.1. The nanowires are considered to be thin enough that the temperature is uniform at all points of the cross section. The temperature dependencies of electrical conductivity “σ” and thermal conductivity “k” are ignored. The conduction of heat on

the suspended nanowire could be described by the following one-dimensional partial differential equation:

$$\frac{\partial T}{\partial t} = k\frac{\partial^2 T}{\partial x^2} - v(T - To) + \frac{q}{\rho c} \tag{4.1}$$

Where, T is the temperature of the nanowire, the x axis goes along the length of the wire, and its origin is located at one end of the suspended wire, ρ is the density of the nanowire, c is specific heat, and the parameters k and *v* are defined as: k=K/ρc, v=Hp/ρcA. Moreover, K is the thermal conductivity, H is the surface conductance, p is the perimeter, T_0 is the ambient (plenum) temperature surrounding the nanowire, and $q=I^2/(A^2\ \sigma)$. At this point, we assume that no heat transfer occurs from the surface of the wire to the ambient, in other words, the second term (v(T-To)) is ignored. The solution to equation 6.1 is given by $T=T_1+T_2$, where T_1 corresponds to the steady state temperature, and T_2 corresponds to the transient temperature. Also, the temperature at both ends of the wire is denoted by T_0, and the temperature at any point in the wire at the beginning of the experiments (t=0) is T_0. According to [65], the solution of equation 4.1 is given by:

$$T_1 = \frac{q}{2K}(Lx - x^2) + T_0 \tag{4.2}$$

$$T_2 = \frac{2qL^2}{K\pi^3}\sum_{m=1}^{\infty}\frac{(-1)^m - 1}{m^3} exp\left[-k\left(\frac{m\pi}{L}\right)^2 t\right] \sin\frac{m\pi}{L}x \tag{4.3}$$

Even though the transient solution given by 4.3 is a series expansion, only the first term is considered as follows:

$$T_2 = \frac{4qL^2}{K\pi^3}\left\{-exp\left[-k\left(\frac{\pi}{L}\right)^2 t\right]\right\} \tag{4.4}$$

Equation 4.2 is the steady state temperature at any point along the suspended fiber during an experiment, and equation 4.4 models the transient temperature solution at the middle of the nanofiber (L/2). At this middle point the temperature of the nanofiber is maximum. Figures 4.1, figure 4.2, and figure 4.3 show the nanofiber cylindrical model, its transient temperature response, and its maximum temperature along the fiber axis using the following material properties [66]:

1. Nanostructure material: Platinum Pt.
2. Length L=100 μm.
3. Diameter d=800 nm.
4. Electrical current I= 6mA.
5. Electrical conductivity σ=9.45e+06 S/m
6. Thermal conductivity K=72 W/m^{o}K.
7. Density ρ=2.15e+04 kg/m^{3}.
8. Specific heat: c=134 J/kg^{o}K.

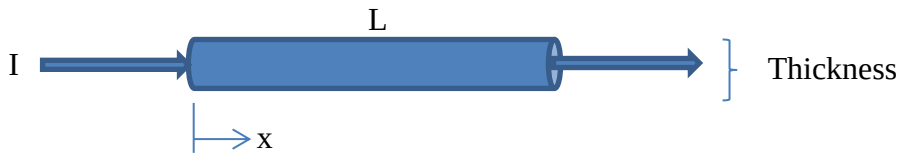

Figure 4.1: Suspended nanofiber cylindrical model

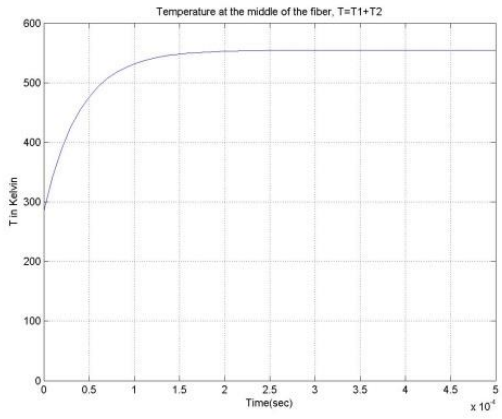

Figure 4.2: Transient temperature response for a platinum fiber

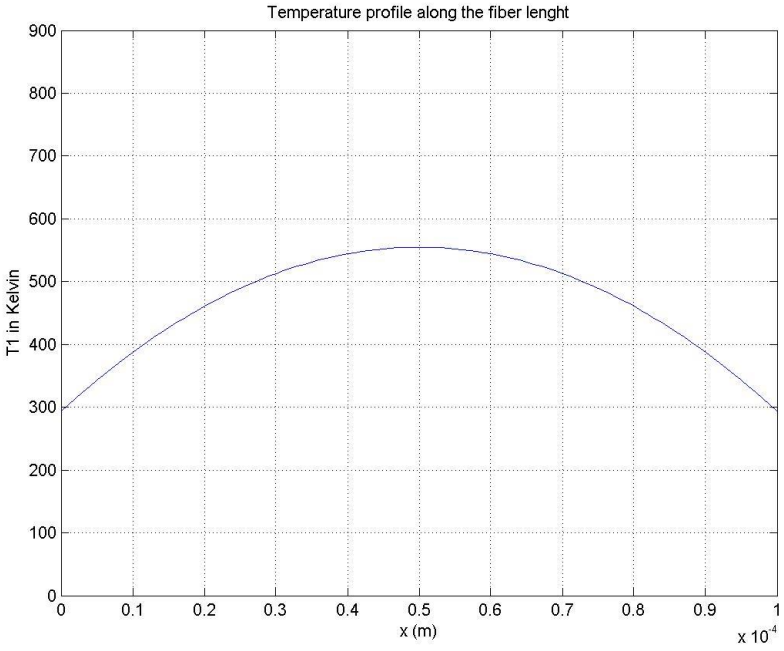

Figure 4.3: Temperature profile along the fiber x axis for a platinum fiber

As can be seen in figure 4.3, the maximum temperature occurs at the middle of the fiber. Making x=L/2, T_1max can be estimated from equation 4.2 as follows:

$$T_{1,max} = \frac{1}{8K\sigma}\left(\frac{IL}{A}\right)^2 + T_0 \qquad (4.5)$$

Figures 4.4 and 4.5 show results when material properties for carbon are used. The properties and parameters used to obtain those simulations are:

1. Nanostructure material: Carbon C
2. Length L=100 μm.
3. Diameter d=1200 nm.
4. Electrical current I= 380μA.
5. Electrical conductivity σ=7379 S/m
6. Thermal conductivity K=6.3 W/m^{o}K.

7. Density ρ=2267 kg/m^3.
8. Specific heat: c=716.51 J/kg^{o}K

Note that the maximum temperature in those simulations is below 3600 ^{o}C, which is the melting point of carbon. According to [66] there is a small discrepancy between theoretical calculations and experimental data. A correction function is obtained experimentally and used to give a better estimation of the temperature at the center of the fiber (Tohmyoh, H. 2013).

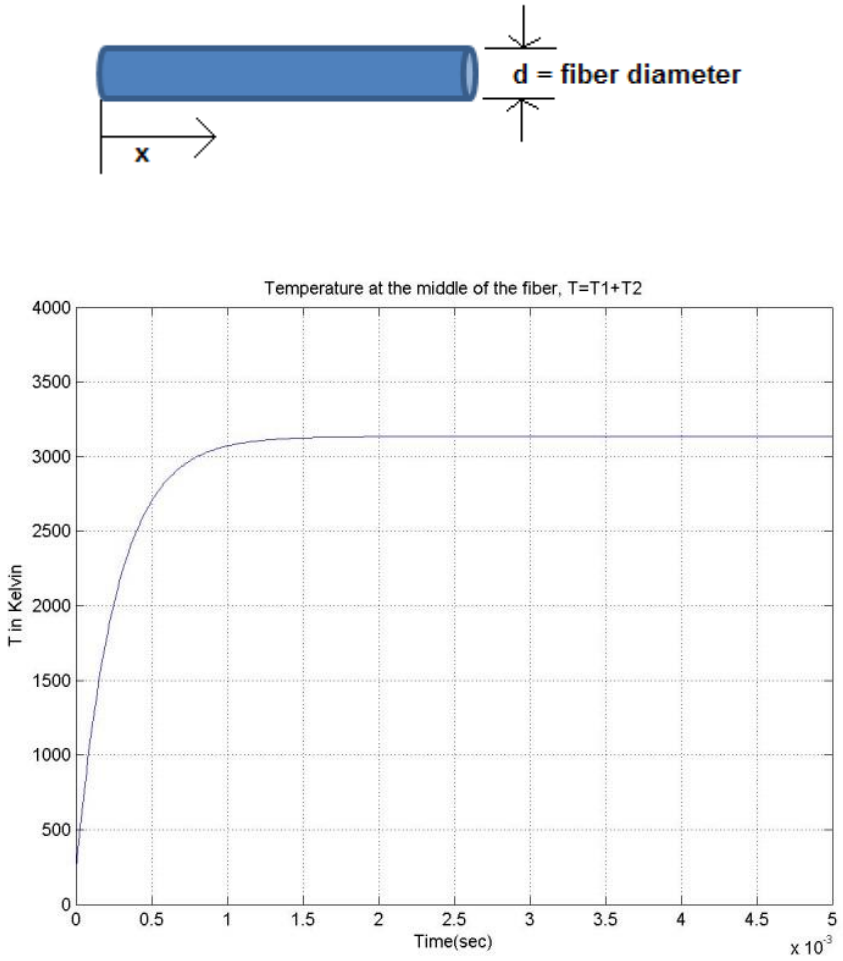

Figure 4.4: Transient temperature response for suspended carbon fiber

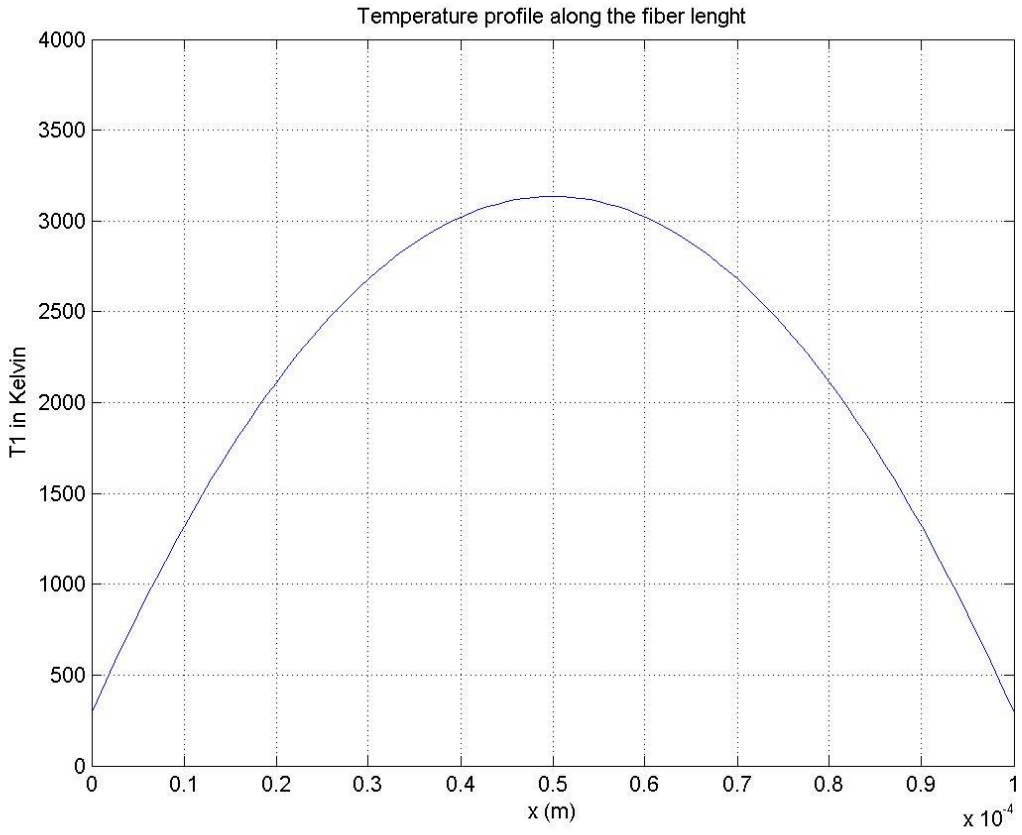

Figure 4.5: Temperature profile along the fiber x axis for suspended carbon fiber

Tohmyoh [66] uses a correction function, f, to correct between experimental and theoretical results for temperature increase along the nanofiber which flow a DC current. The function f takes into account the experimental current required to cut the wires by means of Joule heating. This function is given by:

$$f = \frac{I_o}{I_{exp}} \tag{4.6}$$

In equation 4.6, I_o is the theoretical current to cut the nanowire and it can be calculated as follows [66]:

$$I_o = \sqrt{(T_M - T_0)8K\sigma}\left(\frac{A}{L}\right) \tag{4.7}$$

As we mentioned earlier, K is the thermal conductivity and σ is the electrical conductivity of the nanowire. Also, T_M is the melting temperature point of the nanowire (assumed to be 3600 ^oC in this research), and T_0 is the ambient temperature in °K. Finally, the steady state temperature at the center of the fiber using the correction function f is given by:

$$Tc = \frac{1}{8K\sigma}\left(\frac{ILf}{A}\right)^2 + T_0 \tag{4.8}$$

Equations 4.6 to 4.8 will be used in section 6.4 to show the experimental results for the temperature at the middle point of glassy carbon suspended nanofiber samples.

4.2 Steady State Model Derivation

This research considers a simple steady state model that is used to represent an experimental setup in which an incremental current step is going to be used. The intention to use a steady state model is to remove the transient response and focus in the phenomenon response after the nanowire reaches steady and stable conditions.

Let us start by defining the general heat equation in Cartesian coordinates:

$$\frac{\partial}{\partial x}\left(K\frac{\partial T}{\partial x}\right) + \frac{\partial}{\partial y}\left(K\frac{\partial T}{\partial y}\right) + \frac{\partial}{\partial z}\left(K\frac{\partial T}{\partial z}\right) + \dot{q} = \rho c_p \frac{\partial T}{\partial t} \tag{4.9}$$

Assume that K is constant and rearrange equation 4.9 to:

$$\rho c_p \frac{\partial T}{\partial t} = K\left[\frac{\partial^2 T}{\partial x^2} + \frac{\partial^2 T}{\partial y^2} + \frac{\partial^2 T}{\partial z^2}\right] + \dot{q} \tag{4.10}$$

Considering that the suspended carbon nanofiber varies the temperature only in the x direction (longitudinal axis) and using the model from figure 4.1, the derivatives with respect to y and z are eliminated as follows:

$$\frac{\partial T}{\partial t} = k\frac{\partial^2 T}{\partial x^2} + \frac{\dot{q}}{\rho c_p} \tag{4.11}$$

In equation 4.11, thermal diffusivity k = K / ρc_p, represents the ability of a material to conduct thermal energy relative to its ability to store thermal energy. To obtain the steady state response let $\frac{\partial T}{\partial t} = 0$ and assume that the temperature at the end points of the nanofiber (electrode carbon walls) is T_o, room temperature. Also, change the origin x=0 such that the points x=$\pm\frac{L}{2}$ are the nanofiber´s end points in contact with the carbon electrode walls. The solution is found by integration as follows:

$$\int -\frac{\dot{q}}{\rho c_p} dx = \int k\frac{\partial^2 T}{\partial x^2} dx \tag{4.12}$$

$$k\frac{\partial T}{\partial x} = -\frac{\dot{q}}{\rho c_p} x + C1 \tag{4.13}$$

$$kT(x) = -\frac{\dot{q}}{\rho c_p}\frac{x^2}{2} + xC1 + C2 \tag{4.14}$$

The constant C1 can be obtained from 4.13 using $\frac{\partial T}{\partial x} = 0$ at x=0, which is the center of the nanofiber. The constant C2 can be obtained using the temperature boundary conditions at the end points of the nanofiber. This is substitute T(x=$\pm\frac{L}{2}$) =T_o in equation 4.24 as follows:

$$kTo = -\frac{\dot{q}}{\rho c_p}\frac{\left(\frac{L}{2}\right)^2}{2} + C2 \tag{4.15}$$

$$C2 = kTo + \frac{\dot{q}}{\rho c_p}\frac{L^2}{8} \tag{4.16}$$

Now the maximum steady state temperature of the suspended carbon nanofiber is given by:

$$kT_{max}(x = 0) = -\frac{\dot{q}}{\rho c_p}\frac{0^2}{2} + (0)x + kTo + \frac{\dot{q}}{\rho c_p}\frac{L^2}{8} \tag{4.17}$$

$$kT_{max}(x = 0) = kTo + \frac{\dot{q}}{\rho c_p}\frac{L^2}{8} \tag{4.18}$$

$$T_{max} = To + \frac{\dot{q}}{K}\frac{L^2}{8} \tag{4.19}$$

Equation 4.19 gives the maximum temperature obtained at the center of the suspended carbon nanofiber. The electrical current flowing through the nanofiber will generate the heating; therefore we need to express heat flow in terms of current. Substituting $\dot{q} = \frac{I^2R}{V}$ (joule heating) into equation 4.19 we obtain the maximum temperature reached at the center of the suspended carbon nanofiber when an electrical current flows through it.

$$T_{max} = \frac{I^2 R}{8K}\frac{L^2}{V} + To \tag{4.20}$$

Note that equation 4.20 could also have been obtained directly from equation 4.5 by substituting electrical resistance as follows:

$$R = \frac{\rho L}{A} = \frac{L}{\sigma A} \tag{4.21}$$

Combine equations 4.5 and 4.21 to obtain:

$$T_{max} = \frac{1}{8K\left(\frac{1}{\rho}\right)}\left(\frac{IL}{A}\right)^2 + T_0 \tag{4.22}$$

$$T_{max} = \frac{1}{8K\left(\frac{1}{\frac{RA}{L}}\right)}\left(\frac{IL}{A}\right)^2 + T_0 \tag{4.23}$$

$$T_{max} = \frac{RAI^2L^2}{8KLA^2} + T_0 \tag{4.24}$$

$$T_{max} = \frac{I^2 RL}{8KA} + T_0 \tag{4.25}$$

Define fiber volume as V=AL, then equation 4.25 is converted to:

$$T_{max} = \frac{I^2 RL^2}{8KV} + T_0 \quad (4.26)$$

Equation 4.26 is the same as equation 4.20. It represents the maximum temperature at the center of the suspended fiber. This is a similar result for the steady state component described by equation 4.8, except for the compensation factor f.

4.3 Neuron Temperature Field Model

Hodgking-Huxley [119] developed a very comprehensive electrical model of a neural cell membrane system for dynamic nerve impulse transmission in biomedical applications. A heat flow nanofiber model can also be derived using the Hodskin-Nuxley model but instead of using a potential field (membrane potential), we can use a temperature field (nanofiber temperature).

Figure 4.6 illustrates the proposed electrical model of the nanofiber with an associated capacitance, conductance and current flows. In this case we develop the model considering the following parameters and variables:

1. Temperature difference between media (internal and external): $\Delta T=T-T_o$
2. Heat capacitance of the nanofiber: C
3. Heat conductance per area of the nanofiber: G
4. Heat flows of the nanofiber: Q_T (due to temperature gradient) and Q_q (induced by current flowing).
5. Cross sectional area of the nanofiber: A
6. Radius of the nanofiber: r

The temperature field partial differential equation for the nanofiber is:

$$\frac{\partial^2 \Delta T}{\partial x^2} = C\frac{\partial \Delta T}{\partial t} + G\Delta T - Q_q \tag{4.27}$$

Use the following parameter transformation to make the thermal system analogy:

$$C = \frac{1}{k} = \frac{\sigma c}{K} \tag{4.28}$$

C is the heat capacitance of the fiber from the internal to the external media.

$$G = \frac{\nu}{k} = \frac{H\ p}{K\ A} \tag{4.29}$$

G is the heat conductance of the nanofiber from the internal to the external media using a DC current flowing.

$$Q_q = \frac{q}{\rho c k} = \frac{q}{K} \tag{4.30}$$

Q_q is the stimulus heat flow rate added to the nanofiber due to the temperature field.

$$Q_T = \nabla \cdot \nabla (\Delta T)\Big|_x = \nabla^2 (\Delta T)\Big|_x = \frac{\partial^2 \Delta T}{\partial x^2} \tag{4.31}$$

Q_T is the Laplacian, divergence [$\nabla \cdot$] of the gradient [∇] of ΔT, of the temperature field considering only the longitudinal axis x (unidimensional problem) as shown in the figure 4.6.

Using the appropriate substitutions, equation 4.27 can be transformed to:

$$\frac{\partial^2 \Delta T}{\partial x^2} = \frac{1}{k}\frac{\partial \Delta T}{\partial t} + \frac{\nu}{k}\Delta T - \frac{q}{\rho c k} \tag{4.32}$$

$$\frac{\partial^2 \Delta T}{\partial x^2} = \frac{\rho c}{K}\frac{\partial \Delta T}{\partial t} + \frac{H\, p}{K\, A}\Delta T - \frac{q}{K} \tag{4.33}$$

Also, rearranging terms in equations 4.31 and 4.32 the following equation is obtained:

$$\frac{\partial \Delta T}{\partial t} = k\frac{\partial^2 \Delta T}{\partial x^2} - \nu \Delta T + \frac{q}{\rho c} \tag{4.34}$$

Which is the same heat flow equation 4.1 presented in section 4.1. The relevance of this model stands on the possibility of using the wave equation to predict the propagation of sudden temperature changes due to step changes in joule heat flow (impulse in Q_q) across the fiber. In this case the equation 4.32 could be transformed to obtain a model in terms of a joule heating pulse propagation velocity. Assuming steady state conditions and constant pulse velocity the

following wave equation can be substituted in 4.32, 4.33 or 4.34 to estimate the temperature time solution having a Θ as the propagation velocity:

$$\frac{\partial^2 \Delta T}{\partial x^2} = \frac{1}{\Theta^2} \frac{\partial^2 \Delta T}{\partial t^2} \tag{4.35}$$

Therefore:

$$\frac{1}{\Theta^2} \frac{\partial^2 \Delta T}{\partial t^2} = \frac{1}{k} \frac{\partial \Delta T}{\partial t} + \frac{\nu}{k} \Delta T - \frac{q}{\rho c k} \tag{4.36}$$

Equation 4.36 is a second order ordinary differential equation that can be used to obtain the temperature profiles of the nanofiber if an initial guess to the propagation velocity constant is given.

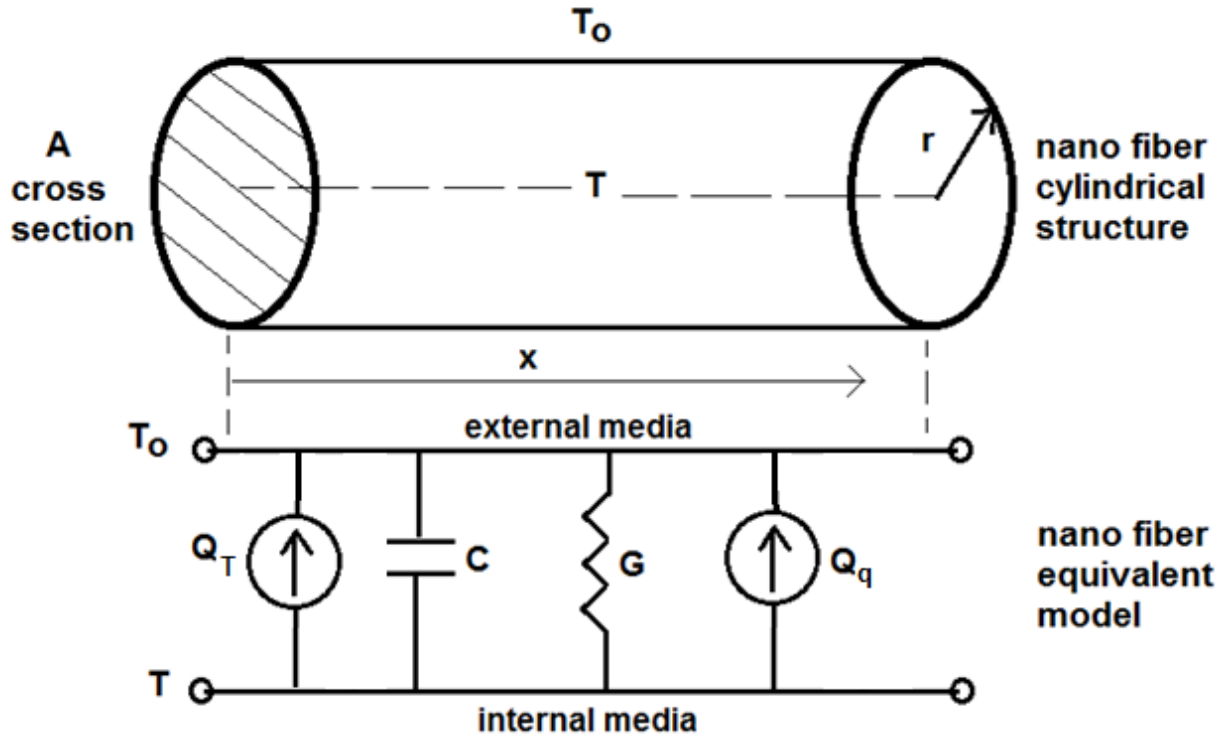

Figure 4.6: Neuron Temperature Field Model of the Nanofiber

4.4 Summary

This chapter presented the Joule heat conduction model of the nanofiber in order to predict temperature profiles when a control current is passed through it. The mathematical model includes the heat conduction, heat capacity and the heat stimulation terms which are part of a second order parabolic partial differential equation having the nanofiber internal temperature as the state variable. The transient and steady state solutions are described and used to perform some elementary simulation exercises using platinum and glassy carbon fibers. Finally, a neuron temperature field model describes an analogy to the Hodgkin-Huxley´s neural cell membrane electrical model posed in the 1950´s. The mathematical model presented in this chapter will be used to predict nanofiber´s temperature profiles in the generation of nanoconstrictions and nanogaps.

Chapter 5

Data Acquisition and Post-Processing Algorithms

This chapter describes the control and data acquisition system implemented in this research to induce the nanoconstrictions and nanogaps over the glassy carbon nanofibers. The system includes the instrumentation which interact directly to the electrode support system, the software programs to perform the control experiments over the nanofiber and the post-processing software programs to develop electric variable calculations, filtering on the gathering data. Those software programs implement algorithms to control different experiments on the glassy carbon nanofiber sample set up.

5.1 Overview

The basic concept behind EM enabled nanoconstriction and nanogap formation is to control an input signal that starts the EM on the nanofibers, while having a feedback loop on the status of the fiber itself. This input signal can be a DC voltage or an electrical current. The input signal has to be ramped up so it can reach the point at which EM starts in the specific sample. Once EM starts, and depending on the desired outcome (nanoconstriction or nanogap formation), the input signal characteristics have to be controlled. The feedback loop allows knowing the status of the fiber during the complete duration of the experiment.

One possible way of knowing the status of the fiber during the duration of the experiment is to measure its electrical resistance. The electrical resistance is expected to change during the experiments performed in this research with the nanofiber samples. There are different schemes to obtain the electrical resistance of a cylindrical wire. One way is to measure the voltage and

current in the sample and then use the Ohm´s law to obtain the resistance accordingly. Figure 5.1 illustrates the measurement scheme where the "Load_sample" represents the nanofiber structure, the "Power_Supply" provides the voltage to be applied, the "Known_resistor" limits the current flowing through the nanostructure and the Switch turns on or off the applied voltage to control the experiment. Having voltage across the "Load_sample" and current through the "Known_resistor" readings enables us to obtain the electrical resistance at any point in time by using Ohm´s law.

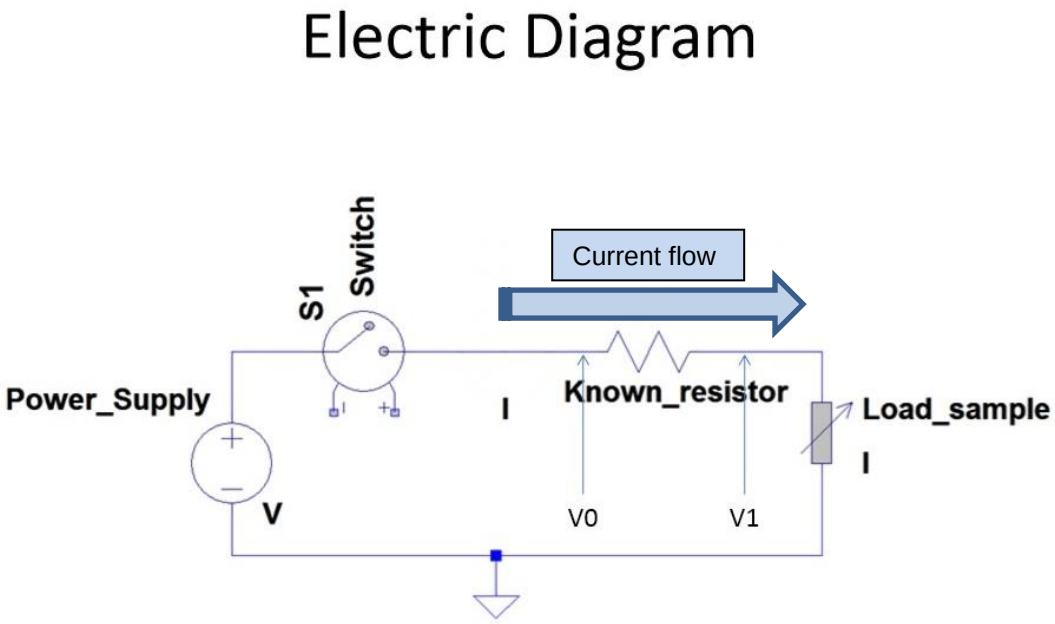

Figure 5.1: Electrical resistance measuring scheme

$$R = \frac{V}{I} \tag{5.1}$$

The "Known_resistor" has a value of 660 Ω. The switch is a commercial relay that is used to open the circuit at the end of the experiment.

5.2 Data Acquisition System

The data acquisition system (DAQ) used is the National Instrument (NI) myDAQ [120] system. This is a low-cost, USB powered, portable DAQ system that allows multiple Input/Output data gathering to measure electric signals coming from the controlled sample experiments. It includes two 16 bits analog inputs, and also two 16 bits analog outputs. These analog ports will be used as oscilloscope (analog inputs), and control signals (analog outputs). Aside from analog signals, myDAQ also allows for digital signal generation. This DAQ system also has several power supplies. These power supplies are +5 V, +15 V, and -15 V.

This DAQ system has several useful applications to measure voltages and currents, as well as complete oscilloscope and multi-meter built-in options. However, none of those applications has the complete functionality required to accomplish a nanoconstriction or nanogap control as required in this research. A complete set of custom-made control routines using LabVIEW [121] are implemented in graphical programing to perform the nanostructure control functions. Those custom-made control graphical programs drive all the required input-output signals in order to properly execute the control algorithms.

5.3 Control Routines

Figure 5.2 shows a flow chart of the complete data acquisition routine. This program was the first one used to try to observe changes on the suspended glassy carbon nanofibers based on applying a ramp up voltage on the fiber. The flow chart blocks in Figure 5.2 are explained as follows.

Start. All electrical connections must be completed before starting with any experiment. The Labview program automatically controls the outcome of the experiment.

Set initial voltage and maximum input current. In this process step, the initial voltage must be set. This initial voltage value is the starting point from which the input control voltage signal starts to ramp up in a linear fashion. An initial voltage of 0.5 V can be chosen as the start point. Based on initial experiments it was found that a voltage of 0.5 V did not damage the nanofibers.

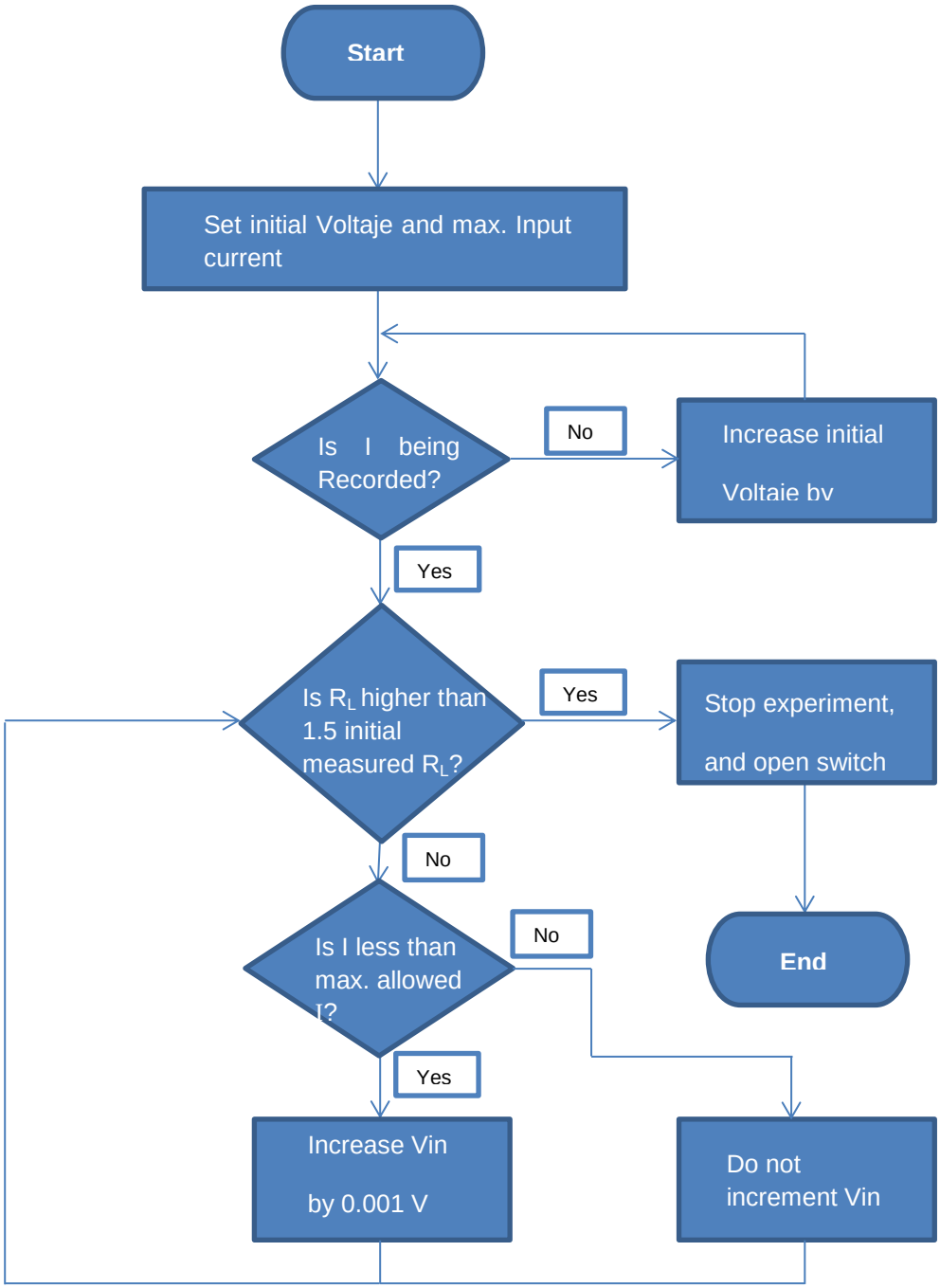

Figure 5.2: Flow chart for data acquisition routine, constant voltage increment

The maximum input current in this section can be selected in a range of 10 μA to 25 mA, which is the maximum current that the DAQ electronics can provide. After initial tests, it was found that the current required from the DAQ board to cut the carbon wires was no more than 10 mA for the carbon nanofiber samples used. If an unknown sample is going to be tested, this input current value could be set to the maximum current of 25 mA. This allows the Labview control program to work and regulate the input signal on its own. The maximum allowed input current can also work as a current limit to save the carbon sample, when knowledge is available about the maximum electrical current that a nanofiber can withstand before failure (i.e. 400 μA).

Is I being Recorded? This first decision step signals the beginning of the recording of the voltage input signals V0, and V1. When a high enough signal is seen from the DAQ at V0, and V1 position (see figure 5.1), an electrical current is calculated. This completes all the necessary signals for the control program to automatically control the outcome of the experiment.

Is R_L higher than 1.5 initial measured R_L? This decision step compares the actual electrical resistance measured from the fiber against 1.5 times R_L, where R_L represents the initial resistance value as measured by the DAQ at the beginning of the recording step. If this condition is met, then the experiment stops. Otherwise, experiment continues. The 1.5 times value for R_L change was chosen after several first experiments. It was seen that this value gave a good trade-off between too low and too much resistance change. If a smaller value would have been chosen, the changes on the fiber thickness due to breakdown phenomenon may have been overlooked. If a larger value would have been chosen, then the fiber could be at risk of burning away.

Is I less than maximum allowed I? In this decision step, a comparison is made between the actual electrical current flowing throughout the series circuit (at present time) and the maximum allowed electrical current set at the beginning of the experiment. If the actual electrical current is less than the maximum allowed current, then the experiments could continue. This implies that the input control voltage signal should continue increasing in the next control program iteration.

If the actual electrical current value is higher than or equal to the maximum allowed current previously selected (from 10μA to 25 mA as described in "**Set initial voltage and maximum input current"**), then the input voltage control signal should stop increasing. This will continue to be true unless a new maximum and higher current limit is manually given to the program.

Increase Vin by 0.001 V. In this process step, the input control voltage signal is increased by the amount of 0.001 V. This voltage is the minimum voltage change (voltage resolution of the system) that the DAQ board can handle. This process step executes only after "Is I less than maximum allowed I" is true. Otherwise, this process step will be stopped. It is important to increase the voltage control signal in small steps. If larger increases were chosen then the fiber would be at risk of burning away without control. However, the smaller the step, the more data points generated during the experiment; and more post-processing computational time required to complete analysis from each experiment. The rather small value of 0.001 V as increase step was chosen because no prior knowledge to electrical input signals was available, regarding these glassy suspended carbon fiber responses.

Stop experiment, and open switch. In this process step, the experiment will stop. First, all the last registered data point will be stored in a file, and then a logical signal will be sent to open the switch (see figure 5.1). Once opening this switch, no electrical current flows throughout the suspended fiber.

End. In this step, we will already have all the data points saved and stored in separated .TDMS files. These .TDMS files are legacy file extensions from LabVIEW containing all the data points registered from the V0 and V1 input signals (see figure 5.1). TDMS files were chosen between several other data types for storing the sampled data, since it is the most efficient data type for fast processes while using LabVIEW.

Figure 5.3 shows an upgraded version of the logic from figure 5.2. This upgraded version was an effort to obtain a greater control on the glassy carbon suspended fiber thickness change

due to the breakdown. Experimental results from both flow chart logics, and implemented on the myDAQ system will be shown on chapter 6. Figure 5.3, shows two additional processes compared to the figure 5.2. The description of those two new elements is given below.

Is R_L increasing? This decision step is responsible for analyzing the value of the electrical resistance from the fiber during the entire experiment duration. When an increase in the fiber electrical resistance is detected, it will then move to the next process action. Otherwise, it will cycle in the previous control steps. The increase in resistance signals induces a change on the fiber diameter due to EM.

Decrease Vin change rate. This is the process step in which a variable voltage increase is obtained. It is a direct response to a detection of an increase in electrical resistance from the fiber sample. This step allows for a better control on the reduction of the fiber, at the moment in which breakdown happens due to a large current density.

5.3.1 Control programs for nanogaps, nanoconstrictions, and steady state experiments

This research provides with three different control programs, developed and tested in LabVIEW, to generate: a) nanogap, b) nanoconstriction and nanogaps using higher sensitivity control, and c) steady state experiments to eliminate transient effects. Each program is further described with some detail in the following paragraphs.

Nanogap generation. Figure 5.2 showed the general block diagram representation of the control program to generate diameter reductions (nanoconstrictions) over the carbon fibers. The program uses a constant voltage increment and it was useful to obtain nanogaps during the early experimentation with the nanofibers. An algorithmic sequence is shown as follows:

1. The control voltage range goes from 0.5 V to +10 V. The voltage control signal increase is defined as 1 mV per iteration. Set the maximum current limit I_{max} to be between 100μA to 6 mA. Set the known series resistance at R_s=660Ω.
2. Set and measure the initial nanofiber resistance at cycle i, $R_{f\text{-}i} = R_{f\text{-}initial}$, by measuring the voltages V1 and V0 (figure 5.1) and calculating the electrical current going throughout the nanofiber, $I_{f\text{-}i}$= (V0-V1) / R_s, and $R_{f\text{-}i}$=V1/ $I_{f\text{-}i}$.
3. The electric current and nanofiber resistances are measured at the next cycle, i+1, such that $R_{f\text{-}(i+1)}$ and $I_{f\text{-}(i+1)}$ are obtained through the data acquisition system. Use $I_{f\text{-}(i+1)}$= (V0-V1) / R_s and $R_{f\text{-}(i+1)}$=V1/ $I_{f\text{-}(i+1)}$.
4. Compare the fiber resistance, $R_{f\text{-}(i+1)}$ and $R_{f\text{-}initial}$. If $R_{f\text{-}(i+1)} > 1.5\ R_{f\text{-}initial}$, then the execution of the control program will stop and go to step 6, otherwise the execution proceeds to step 3.
5. Compare the currently measured electrical current against the current limit, I_{max}. If $I_{f\text{-}(i+1)} > I_{max}$, then the control input voltage stops increasing and the program execution goes to step 3. Iterate until the measured nanofiber resistance is greater than 1.5 times the initial measured nanofiber resistance.
6. Record measurements in output files to prepare data post processing.
7. Observations. It was found during experiments that this program can be used to obtain nanogaps. During experiments a constant voltage increase (ramp in V/sec) generates nanogaps. The nanogaps are generated because the imposed voltage could induce a current stress high enough to break the suspended carbon nanofibers (~0.05 mA to 10 mA depending on fiber geometry). Thus, this approach could generate a nanogap before the measured resistance could reach 1.5 times its initial value. A modification to this program provides a better control of the current flowing and it is explained next.

Nanoconstriction and nanogap generation using a higher sensitivity control. Figure 5.3 includes two modifications to increase the control sensitivity on the outcome of the experiments. It was found that this approach can obtain both nanogaps and nanoconstrictions. Two additional steps were included to the program in figure 5.2. An algorithmic sequence is shown as follows:

1. The control voltage range goes from 0.5 V to +10 V. The voltage control signal increase is defined as 1 mV per iteration. Set the maximum current limit I_{max} to be between 100μA to 6 mA. Set the known series resistance at R_s=660Ω.
2. Set and measure the initial nanofiber resistance at cycle i, $R_{f\text{-}i} = R_{f\text{-}initial}$, by measuring the voltages V1 and V0 (figure 5.1) and calculating the electrical current going throughout the nanofiber, $I_{f\text{-}i}$= (V0-V1) / R_s, and $R_{f\text{-}i}$=V1/ $I_{f\text{-}i}$.
3. The electric current and nanofiber resistances are measured at the next cycle, i+1, such that $R_{f\text{-}(i+1)}$ and $I_{f\text{-}(i+1)}$ are obtained through the data acquisition system. Use $I_{f\text{-}(i+1)}$= (V0-V1) / R_s and $R_{f\text{-}(i+1)}$=V1/ $I_{f\text{-}(i+1)}$. Nine cycles are required before proceeding to step 4: i+1 through i+9.
4. Evaluate the rate of change in resistance at every 8th point, such that $\Delta R = R_{f\text{-}(i+9)} - R_{f\text{-}(i+1)}$, let $R_{f\text{-}initial} = R_{f\text{-}(i+1)}$ and $R_{f\text{-}(i+9)} = R_{f\text{-}final}$. If $\Delta R > 0$ (positive rate of change) then the execution of the control program will go to step 5, otherwise the execution goes back to step 3.
5. If $\Delta R > 100$, then the control input voltage stops increasing and the program execution goes to step 6. Otherwise go to step 3.
6. If $R_{f\text{-}final} > 1.5\ R_{f\text{-}initial}$, then the execution of the control program will stop and go to step 7. Otherwise go to step 3 or use a manual stop.
7. Record measurements in output files to prepare data post processing.
8. Observations. By following this algorithm, the suspended carbon nanofibers will not suddenly break, thus increasing control over the nanofibers and obtaining both controlled nanoconstrictions and nanogaps when desired. Moreover, this algorithm can have a manual exit if an observer monitors its development and performs a manual stop at step 6.

Nanoconstriction and nanogap steady state experiments. Steady state conditions imply that the control signal must remain constant for some time to allow the temperature along the nanofiber to reach a steady state. Using the temperature transient equations from Chapter 4, it is estimated that the time required for the nanofiber to reach steady state is around 3 msec; therefore a control signal that stays in the active state for more than this amount of time will reach steady state according to the model prediction from Chapter 4.

1. The input voltage control signal is changed to a squared signal that stays in the active state (ON value) for 120 seconds, and then goes back to the off state (0 Volts) during 40 seconds. Each new cycle increases the value for the ON state by 0.5 V, being 0.5 V the initial default value for the ON state on the first cycle. The maximum range for the input voltage control signal is from 0.5 V to +10 V. The maximum current range for this program is 100μA to 6 mA.
2. Set and measure the initial nanofiber resistance at cycle i, $R_{f\text{-}i} = R_{f\text{-}initial}$, by measuring the voltages V1 and V0 (figure 5.1) and calculating the electrical current going throughout the nanofiber, $I_{f\text{-}i} = (V0\text{-}V1) / R_s$, and $R_{f\text{-}i} = V1 / I_{f\text{-}i}$.
3. The electric current and nanofiber resistances are measured at the next cycle, i+1, such that $R_{f\text{-}(i+1)}$ and $I_{f\text{-}(i+1)}$ are obtained through the data acquisition system. Use $I_{f\text{-}(i+1)} = (V0\text{-}V1) / R_s$ and $R_{f\text{-}(i+1)} = V1 / I_{f\text{-}(i+1)}$. Nine cycles are required before proceeding to step 4: i+1 through i+9.
4. Evaluate the rate of change in resistance at every 8th point, such that $\Delta R = R_{f\text{-}(i+9)} - R_{f\text{-}(i+1)}$, let $R_{f\text{-}initial} = R_{f\text{-}(i+1)}$ and $R_{f\text{-}(i+9)} = R_{f\text{-}final}$. If $\Delta R > 0$ (positive rate of change) then the execution of the control program will go to step 5, otherwise the execution goes back to step 3.
5. If $\Delta R > 100$, then the control input voltage stops increasing and the program execution goes to step 6. Otherwise go to step 3.
6. Verify the elapsed time in the virtual instrument and stop manually the experiment in about 60 to 70 s. Once stopped go to step 7.
7. Record measurements in output files to prepare data post processing.

8. Observations. This third program is useful for obtaining nanogaps, nanoconstrictions, and emission of light from the suspended carbon fibers when the experiment is run under vacuum (0.1 mbar). Manual stop is performed at step 6.

5.4 Post-Processing Algorithm

By themselves, the LabVIEW programs from the flow charts in figure 5.2 and 5.3 can perform a real time data acquisition and processing to obtain the electrical current flowing through the sample, electrical resistance from the fiber / sample structure, and according voltages. However, several post-processing algorithms were also implemented to analyze the recorded data. This will ensure that the recorded data is interpreted properly, since the same information will be obtained from two different processing approaches. The Matlab platform is used to perform the post-processing analysis of the data gathered by the LabVIEW software.

However, in order to get the data from the .TDMS files recorded after each experiment, a file type conversion between .TDMS and .txt is needed. Once the .txt file is obtained, Matlab can easily import and manipulate the data in vector form.

A low pass digital filter was also necessary to be implemented in Matlab to reduce noise from the recorded data. The signal as recorded is very noisy; a digital low pass Butterworth filter was implemented. Such filter is of the type IIR (Infinite Impulse Response) of 1^{th} order and its transfer function is given in equation 5.2.

$$H(z) = \left(\frac{0.0025+0.0025z^{-1}}{1-0.9950z^{-1}}\right) \qquad (5.2)$$

Figure 5.4 shows a schematic representation of the low pass filter realization in reduced form. Figure 5.5 shows the normalized frequency response for this 1^{th} order low pass Butterworth filter.

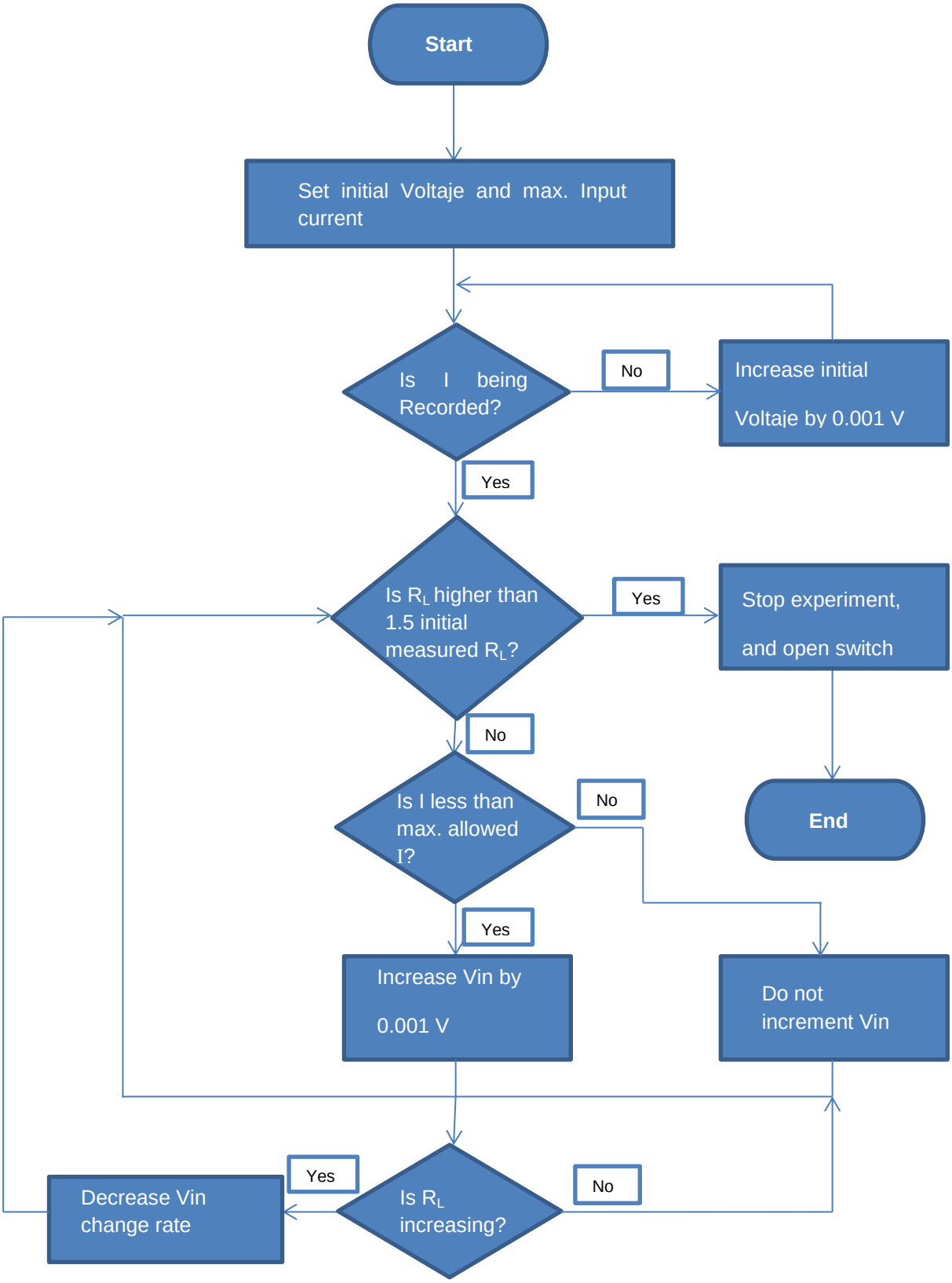

Figure 5.3: Flow chart for data acquisition routine, variable voltage increment

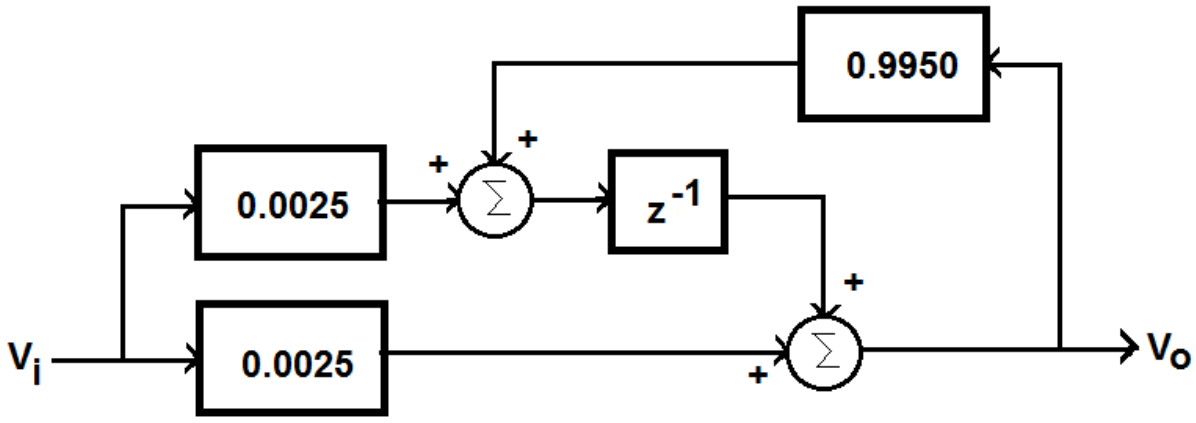

Figure 5.4: Low pass digital filter schematic

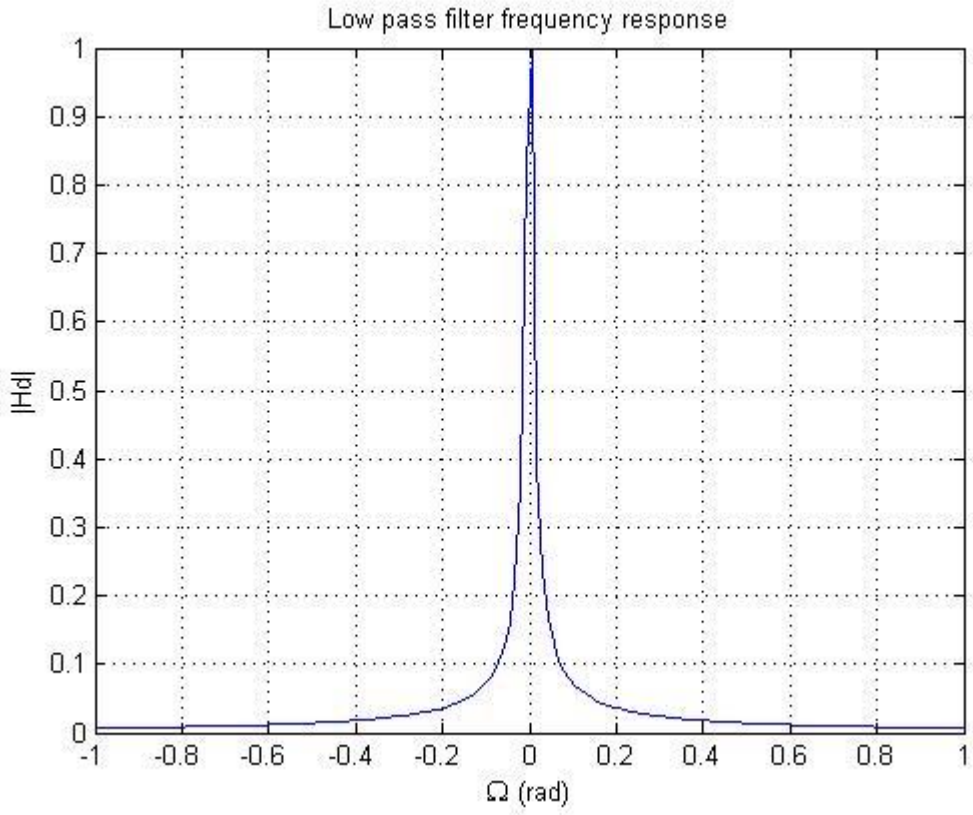

Figure 5.5: Normalized frequency response

Figure 5.6 shows the processing of an acquired signal before and after the filtering process. The signal after filtering is clearer and allows a better reading of the data than without it.

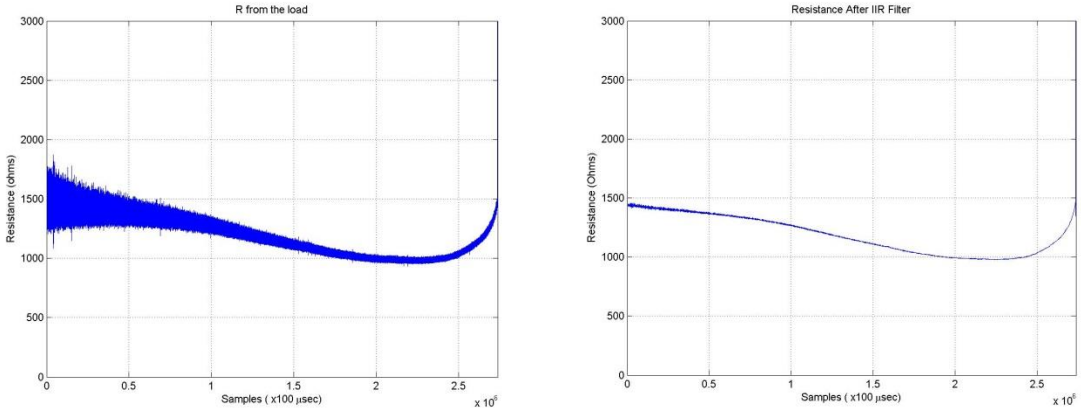

Figure 5.6: Signal before (left) and after filtering (right)

5.5 Summary

This chapter illustrated the data acquisition, control and post-processing routines used to perform the experimentation with the glassy carbon nanofibers. The data acquisition hardware includes a National Instruments MyDAQ multi-I/O data gathering systems which is programmed using LabVIEW as a programming language. The software program includes a set of routines that perform the control and pre-processing of data using graphical programming. Finally, the post-processing includes an IIR digital filter that removes noise and performs a smoothing action to the signal accordingly.

Chapter 6

Nano-fiber Experiments for Free Air Conditions

This chapter presents the experiments and the results obtained from the characterization and SEM observation of the glassy carbon nanofiber structure samples when exposed to free air operating environment. The experiment uses the instrumentation hardware and graphical programing software illustrated in previous chapters to expose the nanstructures to a controlled electrical current flow. The experimental methodology generates different nanostructure phenomena such as fiber constriction, fiber breakdown, nanogap generation, and fiber expansion deformation under program control.

6.1 Introduction

Many challenges rose while performing experiments with suspended glassy carbon nanofiber samples in order to characterize and model their behavior. Those challenges overcame complicated problems that were solved to reach a stable control over the nanoconstriction and nanogap formation on the glassy suspended carbon fibers. Those challenges induced questions regarding the nanofiber samples as follows.

1. How well is the carbon structure-fiber sample fabricated?
2. Is it possible to connect these structures to an external circuit by a good ohmic contact?
3. What are the geometry and size of the suspended glassy carbon fibers?

Other challenges are related to the signal acquisition, processing and control as follows.

4. Is the signal strong enough to overcome white noise by using a simple DAQ system?
5. Does it require a noise cancelling device?
6. Does the performance of the DAQ system have enough sensitivity to control the breakdown phenomenon on such nanofibers?
7. How does the PC analyze the collected data?
8. What signals are useful to control the fiber physical changes?

This chapter describes the methodology and experimentation in an effort to answer those questions. Moreover, modifications to the experimental setup and nanostructure shape will be provided as a direct result from this research.

6.2 Methodology

The very first aspect to complete before performing the electrical analysis is to know the initial geometry and dimensions of the nanofiber samples. This process requires the use of a SEM since the fiber dimensions are in the order of a less than 1μm to a little bit over 4.5μm. Once all the SEM images from the fiber samples are taken, electrical stimulation and sample analysis can follow.

Two important geometric dimensions to measure are the length and average diameter of the fiber samples. Figure 6.1 shows a general overview of how the measurements of fiber thickness were taken on each sample. At least fifteen different points along the fiber length were averaged to obtain the average diameter. In figure 6.2 it is shown an overview of all the sample average diameters; their standard deviation for each one of them is seen in tables 6.1. 6.2, and 6.3, for sample groups 1, 2, and 3, respectively. Figure 6.3 shows the length from all the fiber samples for each group.

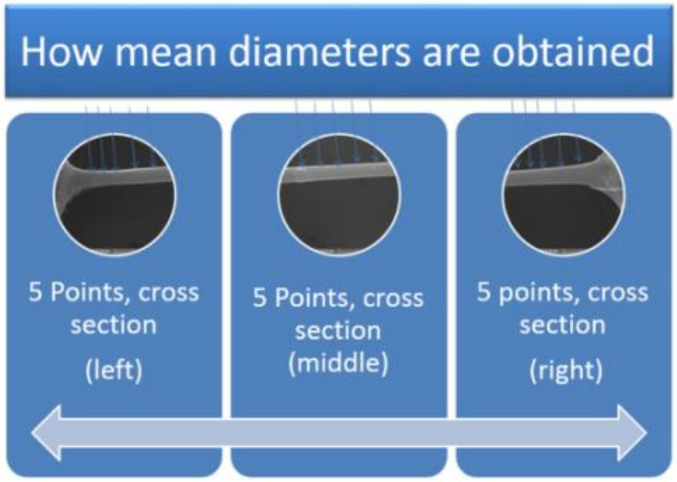

Figure 6.1: Measurement points of fiber thickness

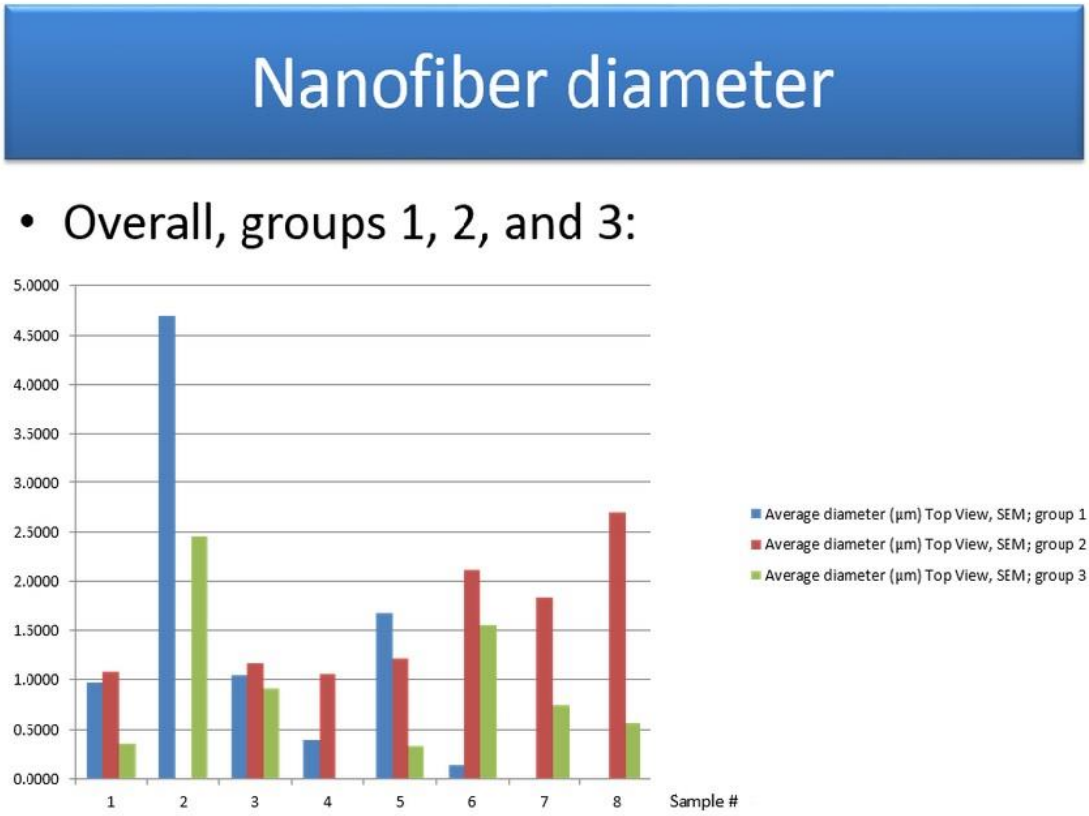

Figure 6.2: Average sample diameter

Table 6.1: Diameter and experimental characteristics of fiber samples from group 1

Sample #	Average diameter (μm) Top View, SEM; group 1	Std deviation top view, SEM (μm)	Average diameter (μm) Tilted, SEM; group 1	Std deviation tilted, SEM (μm)	Experiment name 1	Experiment name 2
1	0.9715	0.0610	0.9238	0.0882	First nanoconstriction*	
2	4.6928	0.8821	5.3312	1.3809	First nanogap *	
3	1.0449	0.0704	1.1735	0.0734	Test 2 / Test 3	Test 12
4	0.4039	0.1273	0.4687	0.1082	Available for testing	
5	1.6831	0.2321	1.6313	0.1410	Available for testing	
6	0.1473	0.0549	0.1676	0.0856	Available for testing	

Table 6.2: Diameter and experimental characteristics of fiber samples from group 2

Sample #	Average diameter (μm) Top View, SEM; group 1	Std deviation top view, SEM (μm)	Average diameter (μm) Tilted, SEM; group 1	Std deviation tilted, SEM (μm)	Experiment name 1	Experiment name 2
1	1.0770	0.1722	0.9905	0.1682	1 μm fiber*	
2	1.1680	0.7080	2.0460	0.7752	Test 45	
3	1.0551	0.0900	1.0492	0.1163	Test 52	
4	1.2202	0.1599	1.4250	0.2573	2 μm fiber*	
5	2.1207	1.1075	1.9523	0.6000	Test 46	
6	1.8456	0.2801	1.7917	0.2760	Available for testing	
7	2.7068	0.3640	2.8235	0.5254	Available for testing	

Table 6.3: Diameter and experimental characteristics of fiber samples from group 3

Sample #	Average diameter (µm) Top View, SEM; group 1	Std deviation top view, SEM (µm)	Average diameter (µm) Tilted, SEM; group 1	Std deviation tilted, SEM (µm)	Experiment name 1	Experiment name 2
1	0.3665	0.0733	0.3869	0.1051	Non-usable (carbon residues)	
2	2.4688	0.0488	2.4435	0.1246	Test 31	Test 34
3	0.9163	0.0944	0.9137	0.1004	Non-usable (carbon residues)	
4	0.3358	0.0995	0.3052	0.0408	Non-usable (several fibers available)	
5	1.5598	0.1463	1.5853	0.1396	Non-usable (carbon residues and damaged wall)	
6	0.7378	0.0598	1.2038	1.6218	Non-usable (carbon residues)	
7	0.5708	0.0644	0.6176	0.0831	Non-usable (carbon residues)	

Group 1 (µm)	Group 2 (µm)	Group 3 (µm)
• 52.39 • 43.48 • 46.32 • 51.72 • 46.20 • 51.08	• 69.85 • 47.10 • 64.98 • 79.86 • 61.82 • 66.25 • 57.47	• 82.36 • 74.56 • 76.15 • 84.17 • 80.33 • 82.20 • 80.36

Figure 6.3: Fiber length for fiber samples of groups 1, 2 and 3

6.2.1 Problems faced on sample structures

Some of the nanofiber samples fabricated came out with defects after pyrolysis. Those samples were not used right away unless a very detailed and complicated repair was performed. The experiments intended in this research required that a single suspended glassy carbon nanofiber was making electrical contact between the two carbon walls built over the support electrode platform.

One of the problems observed is that some samples had carbon residues (leftovers) touching the electrode walls. Figure 6.4 and 6.5 show residues from the electrode walls at either top or bottom of the glassy carbon structure.

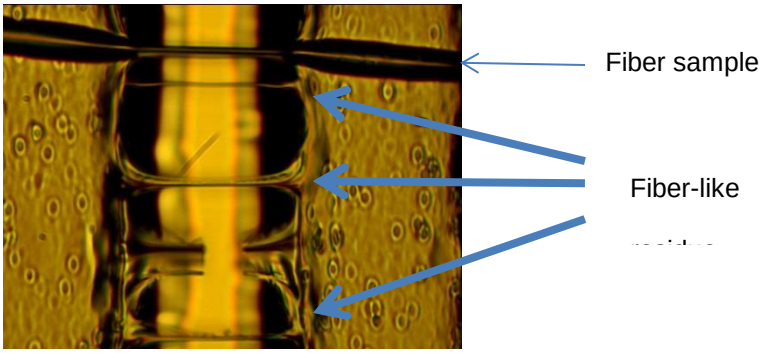

Figure 6.4: Carbon residues in fiber-like shape at top electrode walls

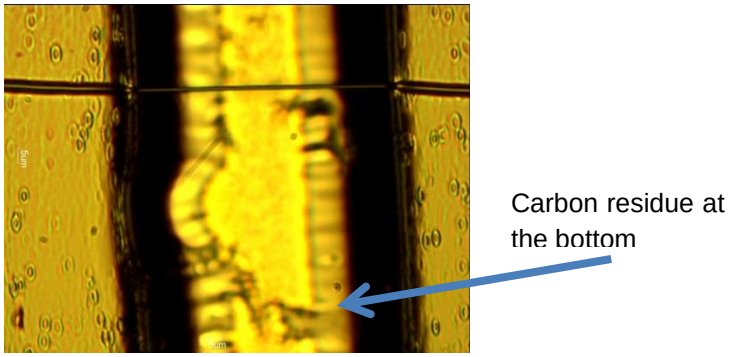

Figure 6.5: Carbon residues at bottom of electrode walls

To remove the top carbon residues a small force was applied using micromanipulator tips. Most of the samples that had fiber-like remains were “fixed” using this approach as shown in figure 6.6. For the samples with carbon residues at the bottom, one possible solution is to try to clean them with oxygen plasma. However, that option was not available at ITESM facilities, and this repair solution was not implemented.

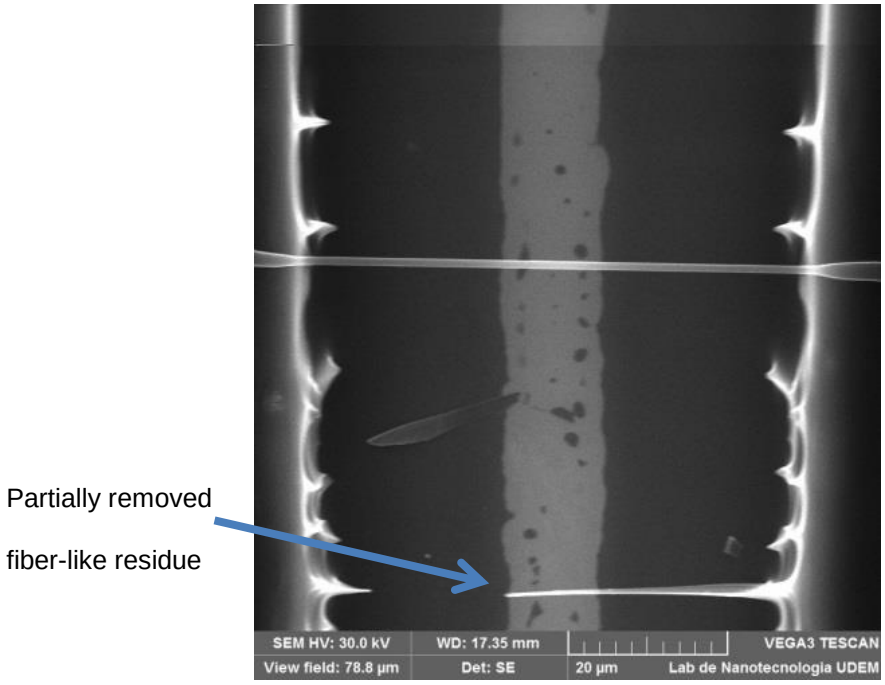

Figure 6.6: Carbon residues partially removed by micromanipulators

The figure 6.7 shows another problem where a wall structure fails during the manufacturing process. This makes it impossible to safely use this fiber in any test, since even the smallest touch with micromanipulator tips could remove pieces of carbon wall electrodes that are not properly fixed to the substrate. Also, the electrical resistance from this sample could greatly vary with carbon wall structure modification, making it more difficult to discern any fiber changes.

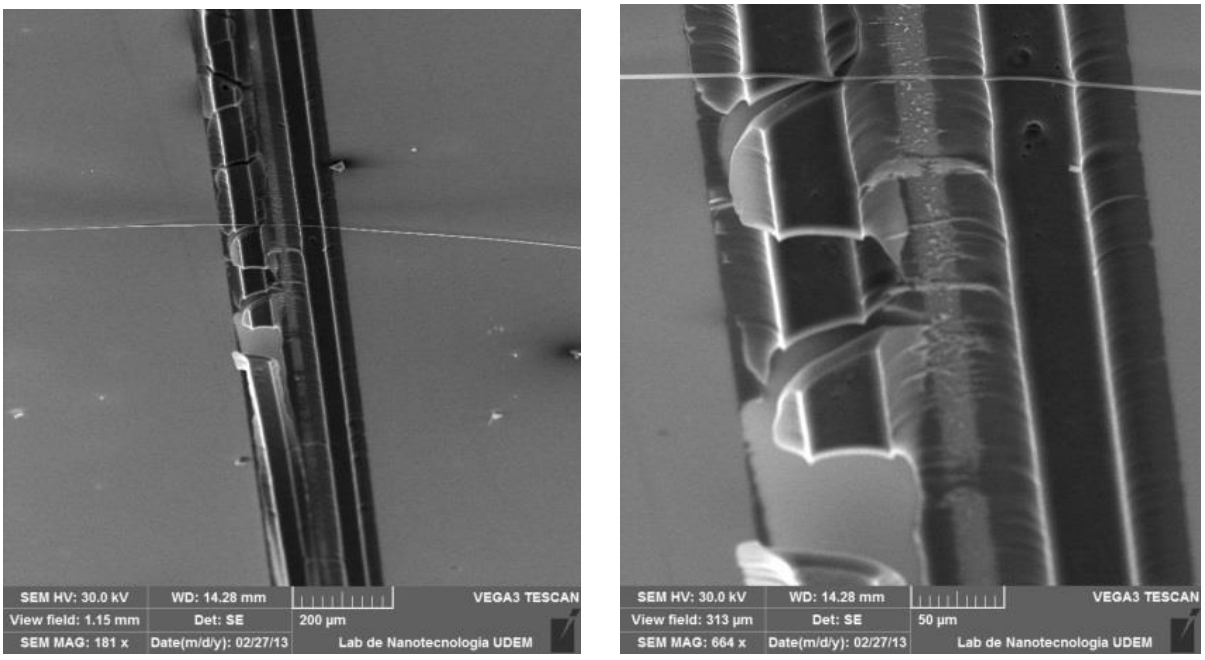

Figure 6.7: Carbon wall failure

6.2.2 Experimental setup under ambient conditions

After obtaining all the relevant geometric aspects from the fiber samples, and determining which ones have the necessary conditions to run the experiments, we are now ready to implement the experiment setup. Such setups can be seen in the pictures shown from figure 6.6. They consist of:

1. The Computer running the control programs.
2. The DAQ system (section 5.2) and additional electronics (section 5.1) having both, the signal conditioning and controller unit.
3. The probe station consisting of a microscope with several magnification lenses, and several micromanipulators.

Figure 6.8: Experimental setup: complete (left), micromanipulator station plus DAQ and signal conditioning (right)

The carbon electrode walls have a certain amount of electrical resistance seen from the contact pad to where the suspended fiber is located along the structure. In the average, an electrical resistance of about 2 kΩ can be measured from the contact pad to where the fiber is suspended. It is advisable to reduce the influence of the carbon electrode wall electrical resistance on the measured signals, in order to control the experiment results. This was especially true for fibers with thickness in the 2 µm range and thicker. In order to avoid the added electrical resistance from the electrode walls, the micromanipulator tips are brought as close as possible to the suspended glassy carbon samples. This will directly reduce the resistance seen from the DAQ system to where the fiber is located. Figure 6.9 shows the micromanipulator tips positioned close to the suspended glassy carbon fiber. It is fairly easy to break away the fiber if the micromanipulator tips are too close from it and one is not careful enough.

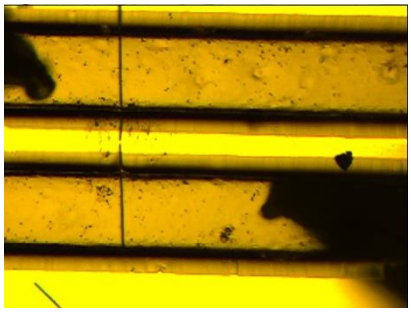

Figure 6.9: Micromanipulator tips in close proximity to the suspended carbon fiber

Once all the setup is ready, and the micromanipulator tips are as close as safely possible to the fiber sample, the experiment to control fiber changes is ready to start.

6.3 Experiment Results for Sample Fibers Operating in Free Air

The experiments performed with the nanofibers operating in free air were driven by control programs described previously in Chapter 5. While results came along and problems were encountered, several modifications to the control programs and/or setup were performed in order to obtain better experimental outcomes. The experiments were performed under the following operating conditions:

1. Normal laboratory conditions, open air, and at room temperature T=25°C and humidity of about 50%. The section 6.3.1 describes results from those experiments.
2. NI-DAQ data gathering system used to perform the data collection tasks and LabVIEW programming to drive the control over the electrical variables.

6.3.1 Experiment results under laboratory ambient conditions

The experiments under ambient conditions were run with the setup depicted in figure 6.8. Those experiments used the simple control program from chapter 5, figure 5.2. Basically, the program consisted of a data acquisition procedure, and a pre-processing routine working synchronously with added external circuitry. The experiment consisted of adjusting a constant current signal until the fiber breaks. Little or none prior experience about the possible consequences of having the fiber samples under electrical stress was available from previous experimentation at UCI. Constant currents between 100 µA and 300 µA for nanofibers having 500nm to 1,500nm were recorded from previous experiments at UCI. Therefore, a constant current signal based on this information was chosen for the experimentation performed at ITESM. For the results shown in figures 6.10 to 6.13, the electrical current was set to 800 µA, expecting to have a noticeable change on the suspended glassy carbon sample.

As can be seen in figures 6.10 to 6.13, the sample did change at the midpoint of the suspended glassy carbon. This was the first nanoconstriction observed during the experiments. In fact, the fiber sample did not break. The voltage and current signals recorded suggest that there was still an electrical current circulating throughout the sample before the experiment stopped (figure 6.14). If the fiber would have break, the voltage signal would have been pulled up to 10 V by the external circuitry because the fiber would operate as an open circuit. Instead, the voltage remained at 6.3 V for a few seconds before the experiment stopped completely after approximately 7.5 seconds. The measured resistance from this experiment went from an initial 4.498 kΩ to 367.9 kΩ after the experiment stopped. The final resistance of 367.9 kΩ is much higher than the original, but lower than a value that could be considered as an open circuit element, i.e. 1 MΩ or higher. The electrical resistance increment is due to the reduction in size of the fiber. In other words, the nanoconstriction produced by this experiment reduced the thickness of the fiber at the midpoint, increasing the electrical resistance (see equation 4.9). The initial thickness of this sample fiber was ~971.5 nm at the midpoint where the nanoconstriction was induced. The final thickness at the midpoint after the experiment stopped was ~146.9 nm. The current flowing throughout the fiber was 826.78 μA at the beginning of the experiment, and 17.47 μA at the end of it. The amount of power dissipated during the experiment was 257 μW, and the time period of the change is 500 msec. Yet another result observed for this experiment is that the fiber bent as seen in 6.10 and 6.12. This bending phenomenon was observed before during the measurements performed at UCI.

For the results shown in figures 6.15 to 6.18, the current was set to 5.84 mA which is the maximum allowed from the external circuitry. This was necessary due to the fact that this fiber sample had an original diameter of 4.69 μm, and such thick fiber withstands a higher electrical current before any noticeable change occurs. A nanogap was formed at the end of the experiment. This nanogap was confirmed by the voltage/current signals obtained during the experiment as seen in figure 6.19. The voltage went up to the maximum possible voltage (10 V), and the electrical current went down to 0 A, this indicates that there is an open circuit, and a breakdown in the fiber was induced, generating the nanogap. The electrical current went from 5.84 mA to 0.032 μA, which is considered as 0 A under this setup. The electrical resistance measured went from 536 Ω to 337 MΩ, where this last value is considered an open circuit. The

dissipated power during the experiment was 16.28 mW, and the time duration was around 7.5 seconds. The thickness of the sample fiber went from 4.69 μm at the midpoint to 414 nm after nanogap formation. Although it is difficult to finely observe the nanogap with the current SEM equipment used, a close approximation gives a nanogap distance of about 50 nm (+- 15 nm).

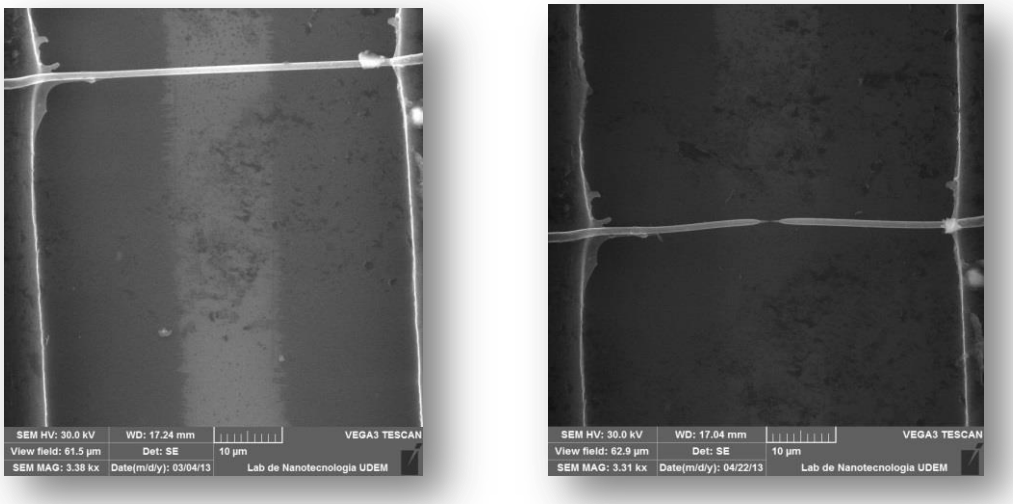

Figure 6.10: First experimental nanoconstriction, top view

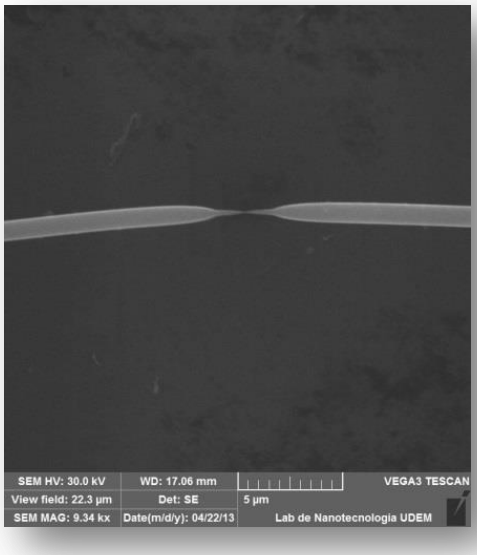

Figure 6.11: First experimental nanoconstriction, top view, zoom in

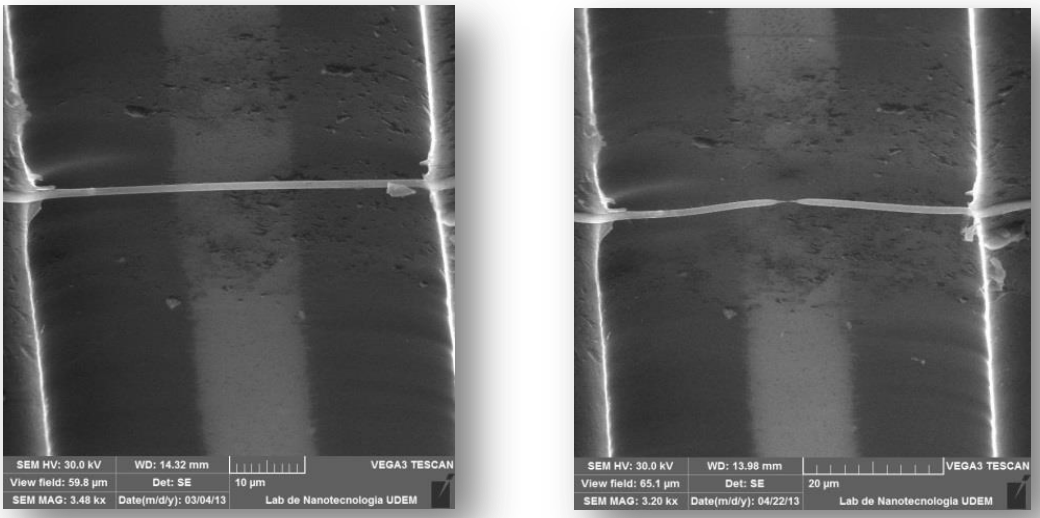

Figure 6.12: First experimental nanoconstriction, tilted view (60^{o})

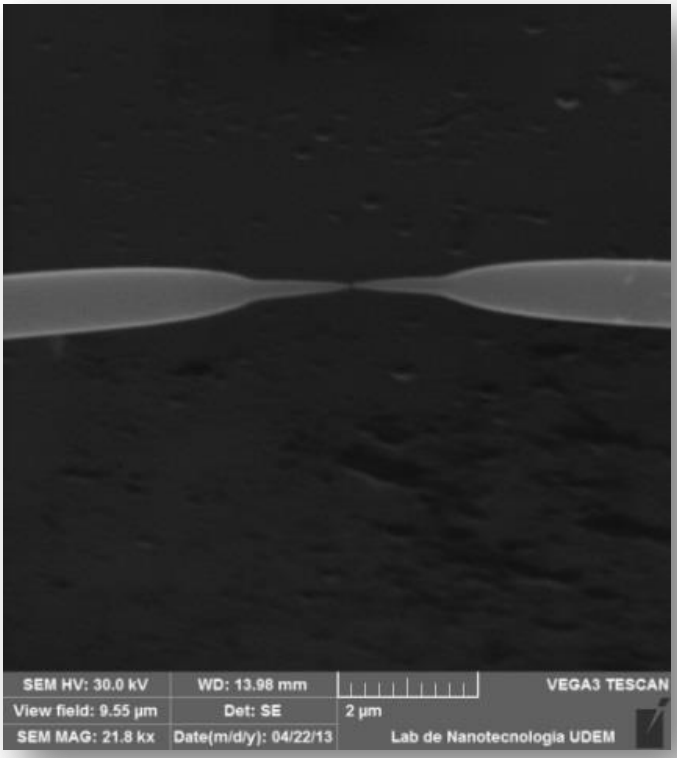

Figure 6.13: First experimental nanoconstriction, tilted view (60^{o}), zoom in

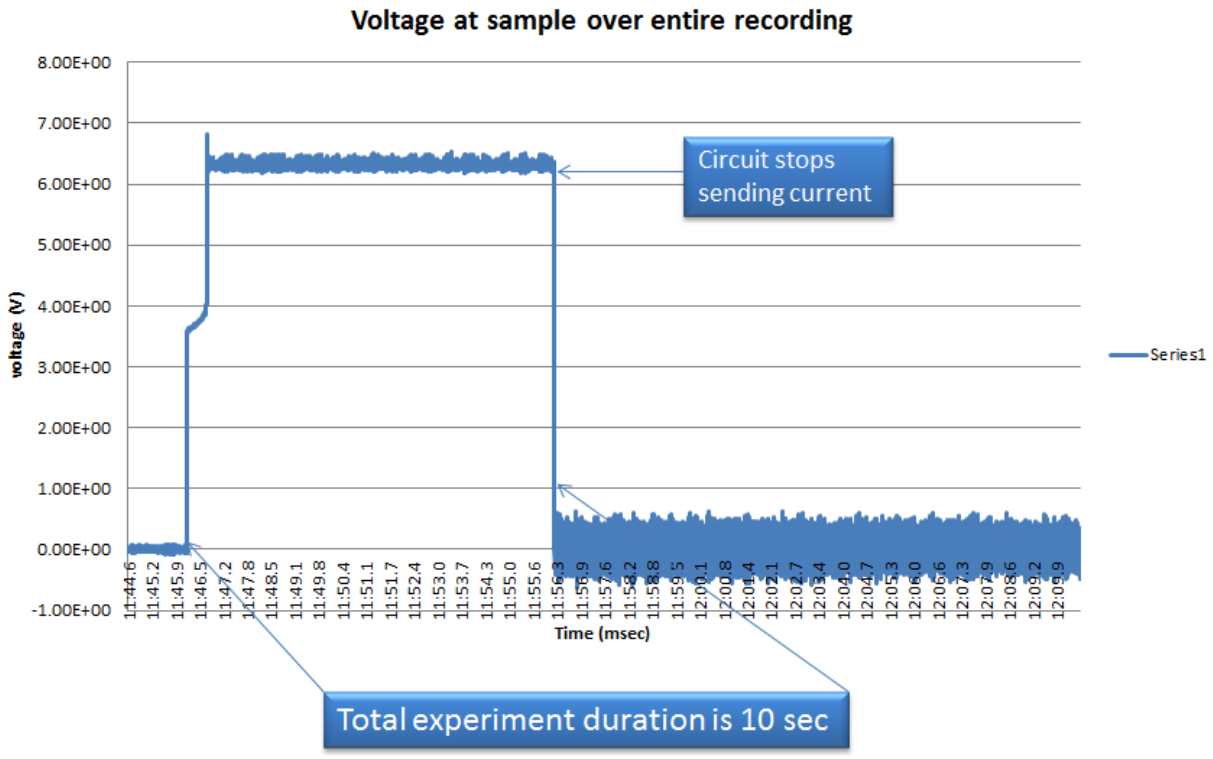

Figure 6.14: Voltage confirmation of electrically conductive sample

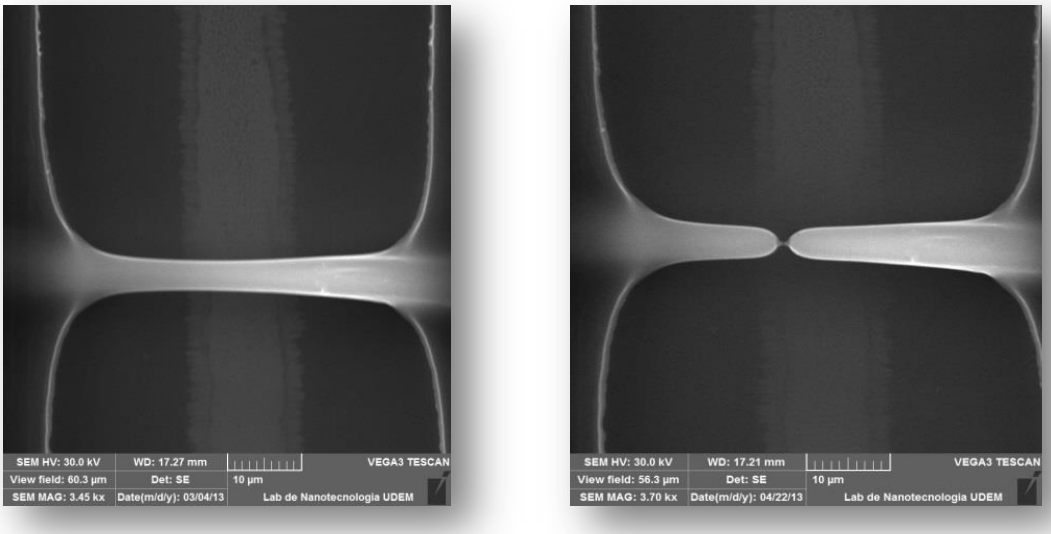

Figure 6.15: First experimental nanogap, top view

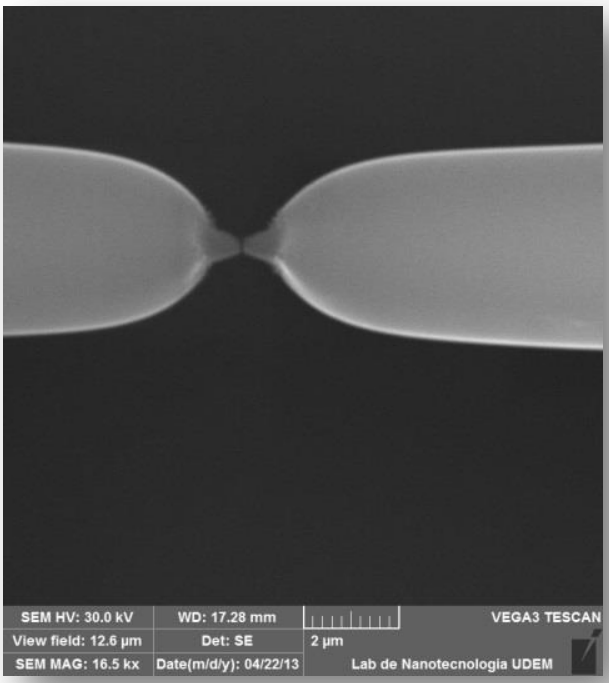

Figure 6.16: First experimental nanogap, top view, zoom in

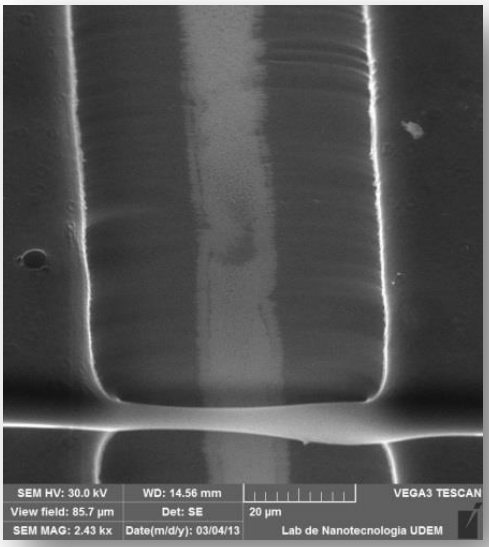

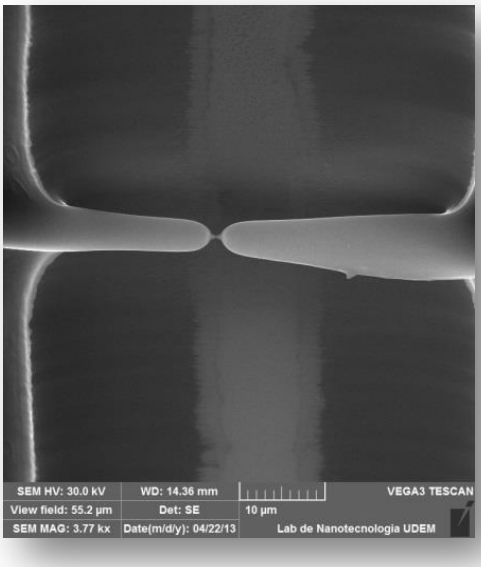

Figure 6.17: First experimental nanogap, tilted view (60^{o})

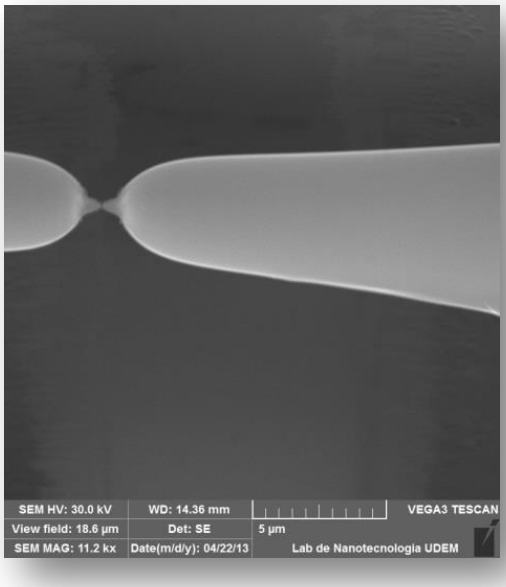

Figure 6.18: First experimental nanogap, tilted view (60^{o}), zoom in

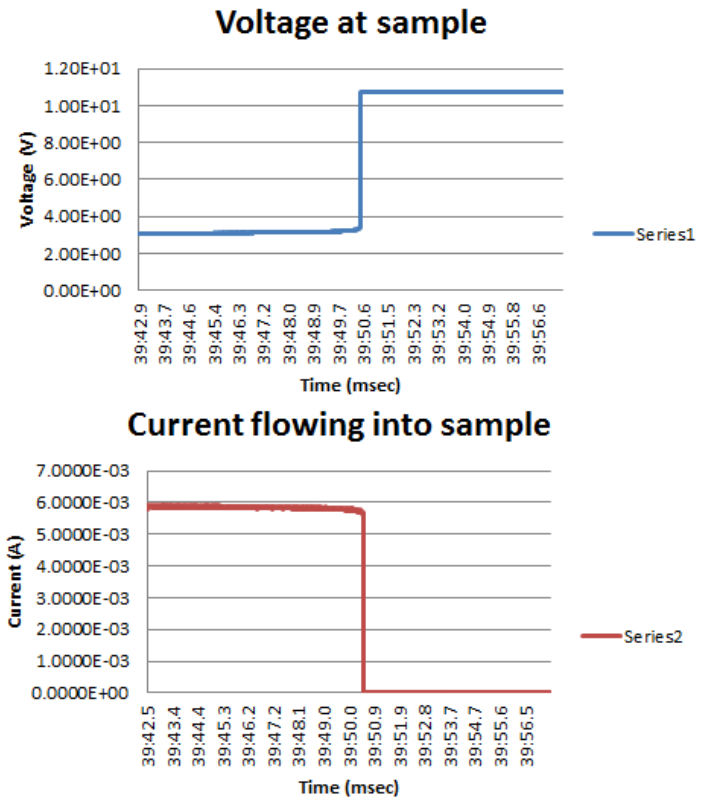

Figure 6.19: Nanogap confirmation by voltage / current readings

The results obtained and shown from figures 6.10 to 6.19 gave the first two important results that oriented the next steps in the experimental setup for this research. In one case, a nanoconstriction was produced and in the other case a nanogap was generated. Both experiments required a better control to condition the experimental outcome. Therefore, the next control program and experimental setup included a much better signal control and measurement capabilities than the earlier experiments. Instead of using a constant current approach, it was decided to change into a DC voltage signal that will slowly ramp up until a change on the fiber would be sensed. Then at this sensitivity point the experiment should be ideally stopped. Since the DAQ system used has two different analog output ports, using a voltage as the control signal was a best alternative and a straightforward approach. The logic for the control program at this stage was explained in chapter 5, figure 5.3.

A real time data acquisition program was implemented using the analog input ports from the DAQ system, and using the electric circuit as shown in Chapter 5, figure 5.1. However, there was still another problem as explained in 5.4. The measured voltages were very noisy, in other words, the real value for electrical resistance, current, and conductance was hidden behind the noisy signals. In order to recover the signal from the recorded data both LabVIEW control program and post-processing algorithms had data filters to remove the noise from the signal.

After the noise problem was solved, new experiments were performed. Changes from the previous setup to this new improved version are mentioned in the following paragraphs. Also, the calibration procedure for the DAQ system is explained to describe the instrumentation preparation procedures before a real test could be run. To consolidate the preparation, some experimental results will be shown with and without a noise filter in order to demonstrate the effectiveness of the filtering scheme.

The changes for in this new control program version are that the applied voltage was varied programmatically by the graphical programming software LabVIEW. The voltage range went from 0 V to 10 V which is the positive rail to rail voltage from the DAQ system used. The steps for the voltage change were set to 1 mV. A completely new LabVIEW interface was developed and used to control and observe the real-time results during the experiment.

Furthermore, a commercial variable resistor was used to test the software, simulate the sample electrical resistance, and calibrate the complete system. This variable resistor was connected in place of "Load_sample" from Chapter 5, figure 5.1. This calibration procedure helps in making sure that the complete systems works perfectly before a real sample would be used. Failure to do so could risk in one of the following scenarios:

1. The suspended glassy carbon fiber breaks without any control producing a waste sample.
2. Erroneous captured data for post-processing analyses causing a faulty experiment.

During the calibration procedure, a commercial resistor of 15 kΩ was chosen. This variable resistor could provide a similar electrical resistance to the one measured in previous experiments on suspended glassy carbon fibers. The voltage was varied from 1 V to 5 V in 0.001 V steps. Electrical current, resistance, and conductance were obtained during the experiment by the DAQ system and LabVIEW program. Figure 6.20 shows the results from the pre and post-processing routines after the calibration procedure. Only the first part of the experiment is shown. Remember that two separate routines were implemented to analyze the data, one for the real-time data acquisition using LabVIEW, and another for the MATLAB code as the post-processing algorithm.

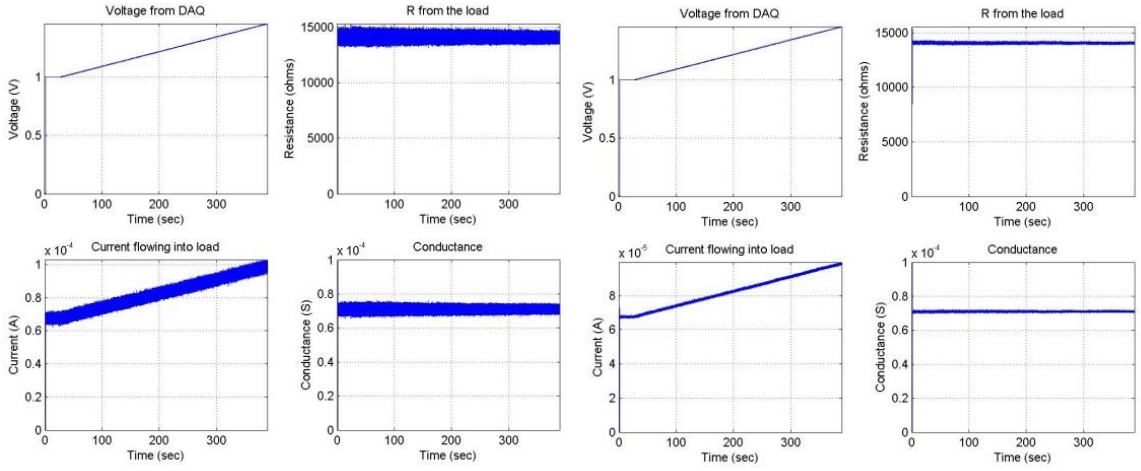

(a) **(b)**

Figure 6.20: Calibration step, (a) pre-calibration and (b) post-processing

Note that in figure 6.20 (a), the electrical resistance, current, and conductance signals carry the measuring experiment noise from the DAQ system. This noise is inherent to the circuitry and system, but it can be fixed by applying hardware or software low pass filters as mentioned in section 5.4. Figure 6.20 (b) shows the same previous calibration results but now applying a filtering scheme. A simple observation of figures 6.20 (a) and (b) illustrates a clear view of the benefits and effectiveness of the noise reduction filtering applied to the recorded data.

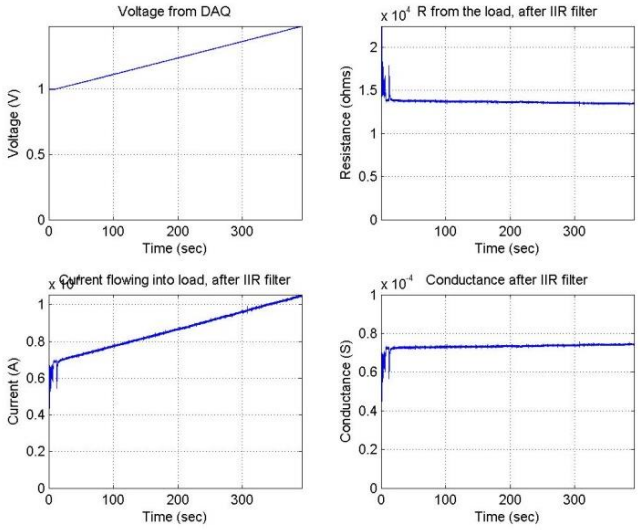

(a) First data segment

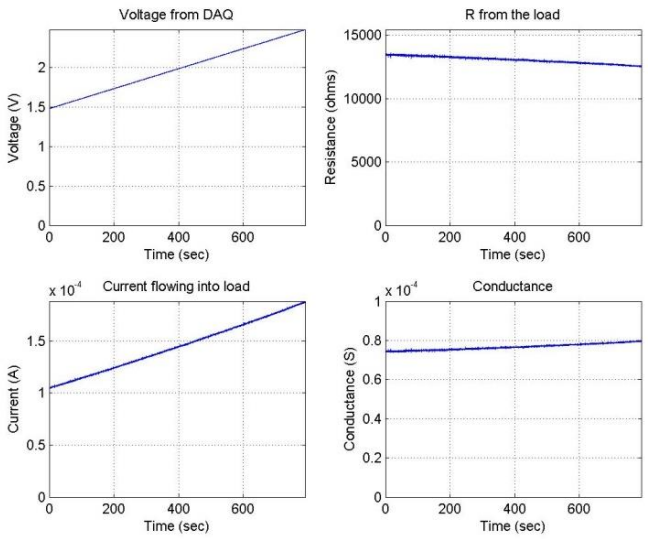

(b) Second data segment

Figure 6.21: Results from 1 μm diameter fiber

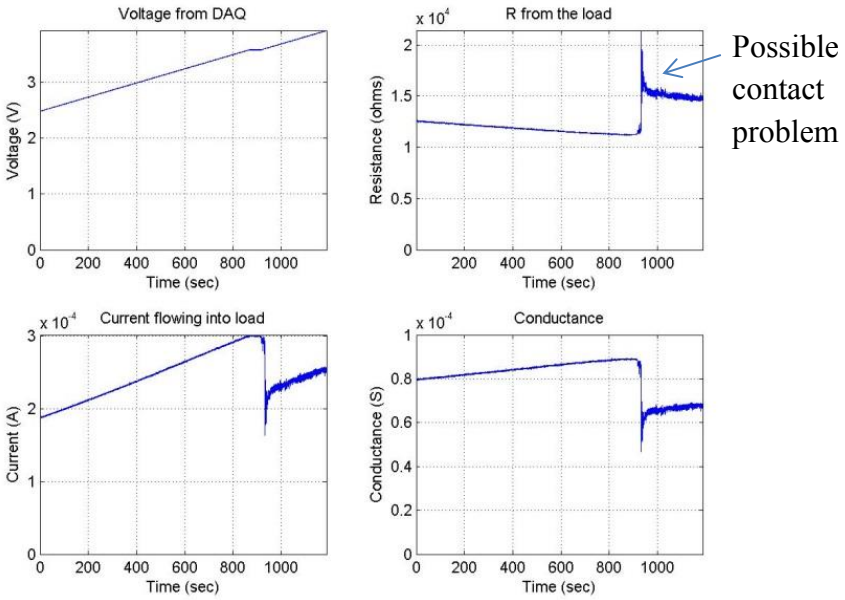

(a) Third data segment

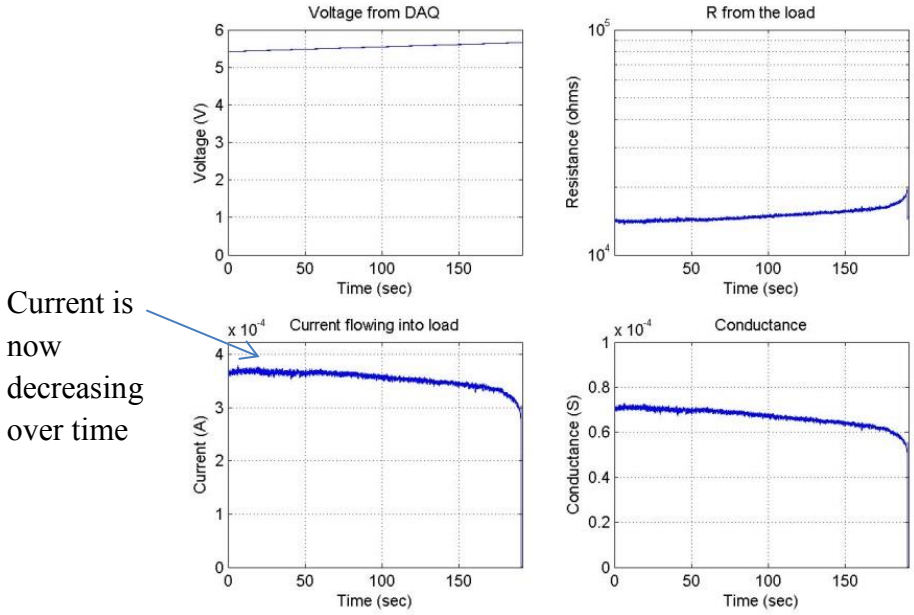

(b) Fourth data segment

Figure 6.22: Results from 1 μm diameter fiber (continued)

After the calibration procedure was completed, and good results were obtained, the experiments using real samples followed. In particular, a fiber sample with 1 μm diameter; and a fiber sample with ~ 2 μm in diameter were used during the following two experiments. Figures 6.21 to 6.22 show the results from the 1 μm diameter fiber; and figures 6.23 to 6.25 show the pre and post SEM images from this sample. This fiber broke, generating a nanogap similar to previous experiments.

The gap distance generated for this sample ranges from about 95 nm to 123.8 nm. The fiber thickness at the tip is approximately 161.9 nm (+/- 15 nm). The thickness reduction from the original thickness to the final thickness is about 80.46 % size reduction. The dissipated power needed at the fiber sample to create this nanogap was ~1.9 mW. A voltage of 5.45 V and a current of 367 μA was enough to start changing the fiber as seen it on figure 6.25. The final resistance before breaking of the fiber was approximately 20 kΩ, which is 0.33 times higher than the initial measured resistance.

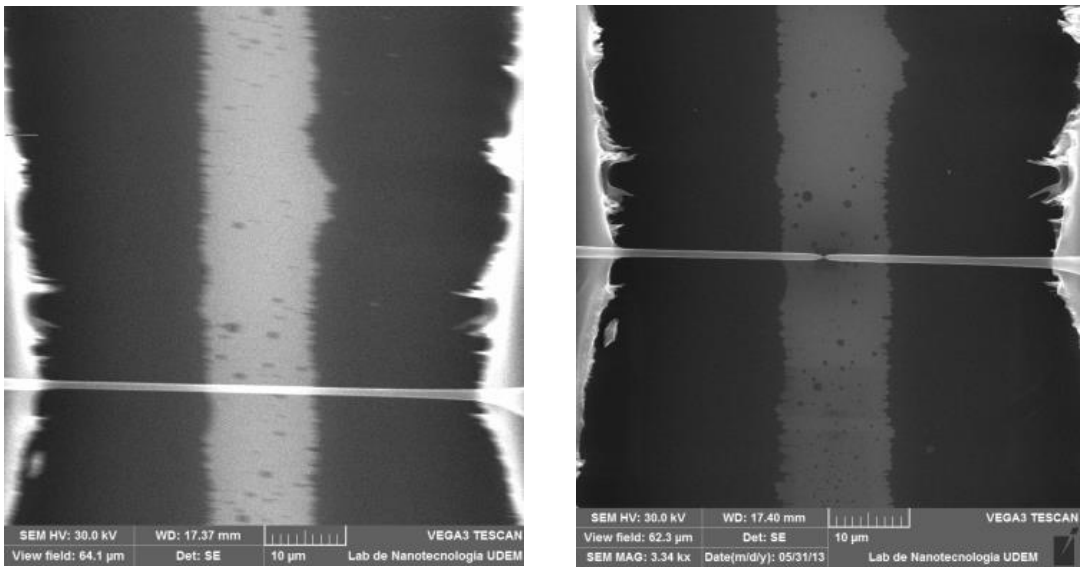

(a) **(b)**

Figure 6.23: SEM images from 1 μm diameter fiber, (a) pre and (b) post experiment, top view

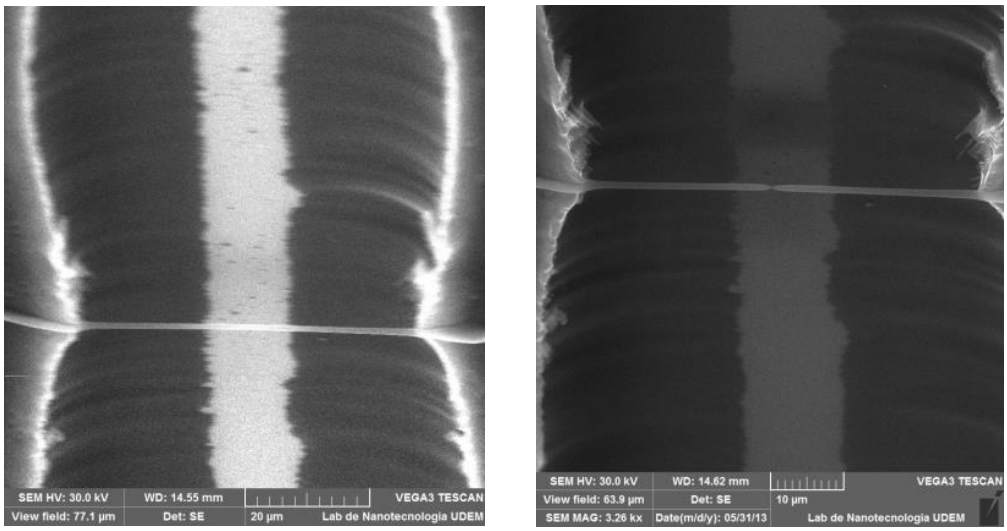

(a) **(b)**

Figure 6.24: SEM images from 1 µm diameter fiber, (a) pre and (b) post experiment, tilted view

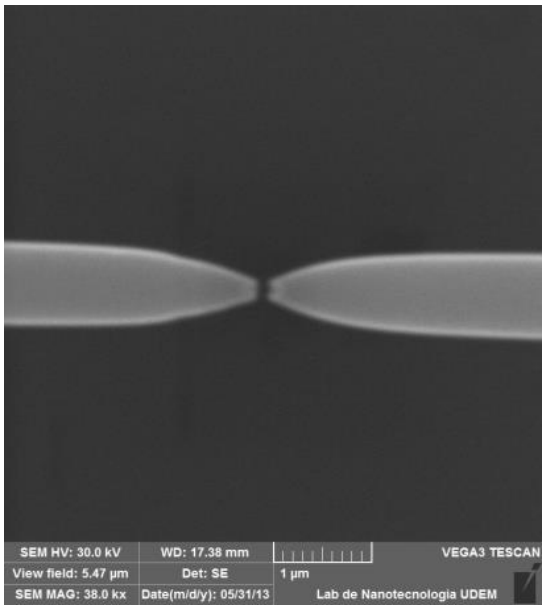

Figure 6.25: SEM image from 1 µm diameter fiber, zoom in, top view

This experiment was considered a success even though the fiber sample broke, generating a nanogap instead of a nanoconstriction. So far, two nanogaps have been generated in the research experiments. This experiment provided a detailed view of the data signals by setting the maximum sampling rate of the DAQ system to 1 sample for every 10 μsec. With the amount of data generated, additional post-experiment analysis was performed to higher extent. The post-experiment analyses and the deep extent of the post-processing allowed designing small modifications to the control program in order to gradually generate and control nanoconstrictions under software programming.

Another nanofiber sample test was run before a new experimental design modification provided the gradual control of a nanocontriction. In this case, a sample fiber of ~2 μm was used and the similar experimental conditions were chosen but one difference: the final voltage from the control signal was limited to a lower value than in previous experiments. The applied voltage was varied from 1 V to 4.08 V in steps of 1mV. This lower maximum voltage limit was used intentionally in order to avoid breaking the fiber sample. One assumption was made here: the fiber thickness could influence in the amount of maximum dissipated power by the fiber before breaking. For fibers of the same length, the thicker the fiber, the higher the electrical power required to break it. Therefore, by lowering the maximum input voltage it was intended to extend the experiment before breaking of the fiber. The result obtained during this experiment was that the fiber did not break, corroborating the assumption that a bigger fiber would require more power to form a nanogap. Figures 6.26 and 6.27 show the experimental results from this experiment and the SEM pictures of the nanofiber, respectively, in which no fiber change was observed.

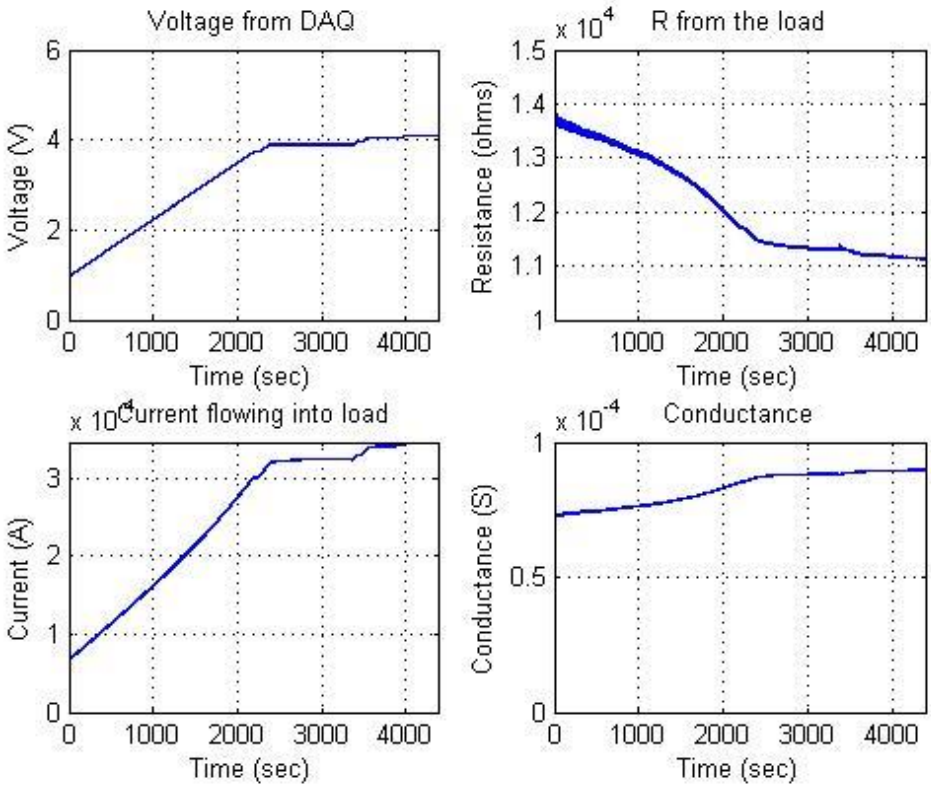

Figure 6.26: Electrical variables and parameters for experiment of 2 µm fiber

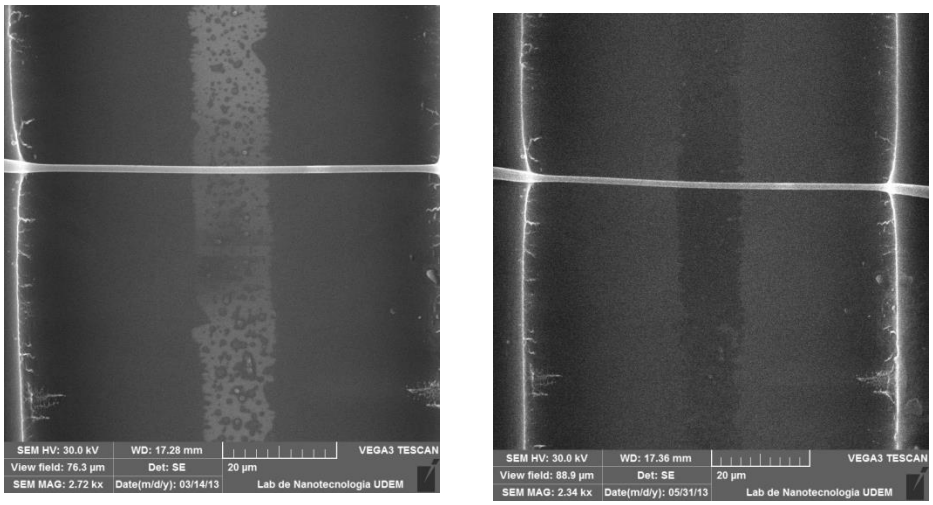

(a) **(b)**

Figure 6.27: SEM images for 2 µm fiber: (a) before and (b) after experiment

The maximum dissipated power during this experiment was ~1.3 mW. An electrical current of 345 μA was the maximum measured. No noticeable change was observed as shown in figure 6.27 (b). This controlled experiment result is consolidated in later sections that provide a comparison of different experiments. To facilitate the described experiments, a reference for each different experiment will be provided as Test 1, Test 2, Test 3, and so on.

After the preliminary test results where nanoconstrictions, and nanogaps were generated, experiments were designed to controlled thickness reduction (nanoconstriction) of a suspended micrometer fiber before the breakdown phenomenon occurs. Modifications to the control software are required to provide this gradual thickness reduction on the fiber. One modification consisted of changing the input voltage slope when increments in the electrical resistance are detected. The idea was to reduce the rate of input voltage increase to avoid an abrupt breakdown of the fiber and to permit a gradual change in the current flowing.

A 1 μm fiber sample was used to test this new idea. This sample had been used in two previous experiments performed using a constant step increase in voltage. Those experiments registered 165.69 μW and 1.6 mW of power dissipation and no apparent physical changes to its diameter were observed from SEM images due to the low dissipated power during both experiments. Those experiments are called Test 2, and Test 3, respectively.

Test 2 and Test 3 provide two reference experiments that show the possibility of having a controlled applied input DC voltage, inducing an electrical current through the suspended carbon fiber, without generating any geometric modification, as observed in figure 6.28. Suspended carbon fibers require a certain amount of dissipated power, in order to form a nanoconstriction which eventually could generate a nanogap. Experiment Test 12 is a continuation experiment using the sample from Test 2 and Test 3. The results from Test 12 are the first proof of a controlled experiment generating a nanoconstriction.

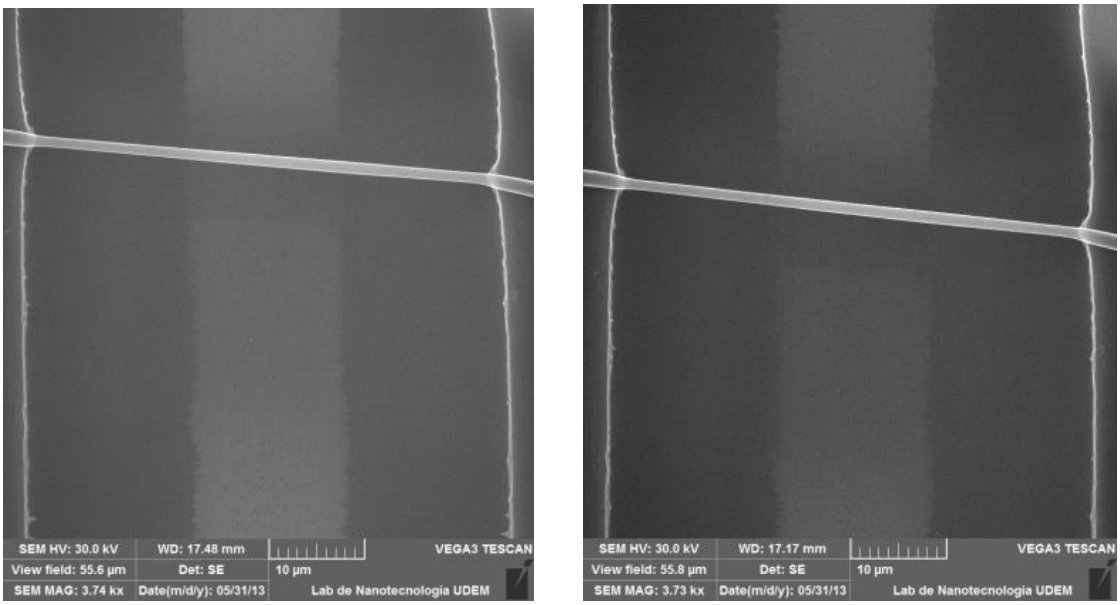

(a) **(b)**

Figure 6.28: SEM images from Test 2 (a) and Test 3 (b), no change observed

In Test 12, the modification to the control signal was implemented. Now, the control voltage signal decreases its ramp rate if the fiber electrical resistance increases ($\Delta R>100\Omega$) during the experiment. A variation was induced on the fiber thickness close to the center of the suspended carbon fiber without generating a nanogap. The maximum dissipated power for Test 12 was 1.7 mW which was higher than the power recorded from Test 2, and Test 3. Figure 6.29 show a comparison between Test 3 (before nanoconstriction) and Test 12 (after nanoconstriction). Figure 6.30 shows a close up view of the nanoconstriction from Test 12. In figure 6.30 visual guides t1 (993 nm), t2 (826 nm), and t3 (1059 nm) were added. The reduction in thickness was around 200 nm which roughly represents 20 % of the original fiber thickness at that particular point along the fiber.

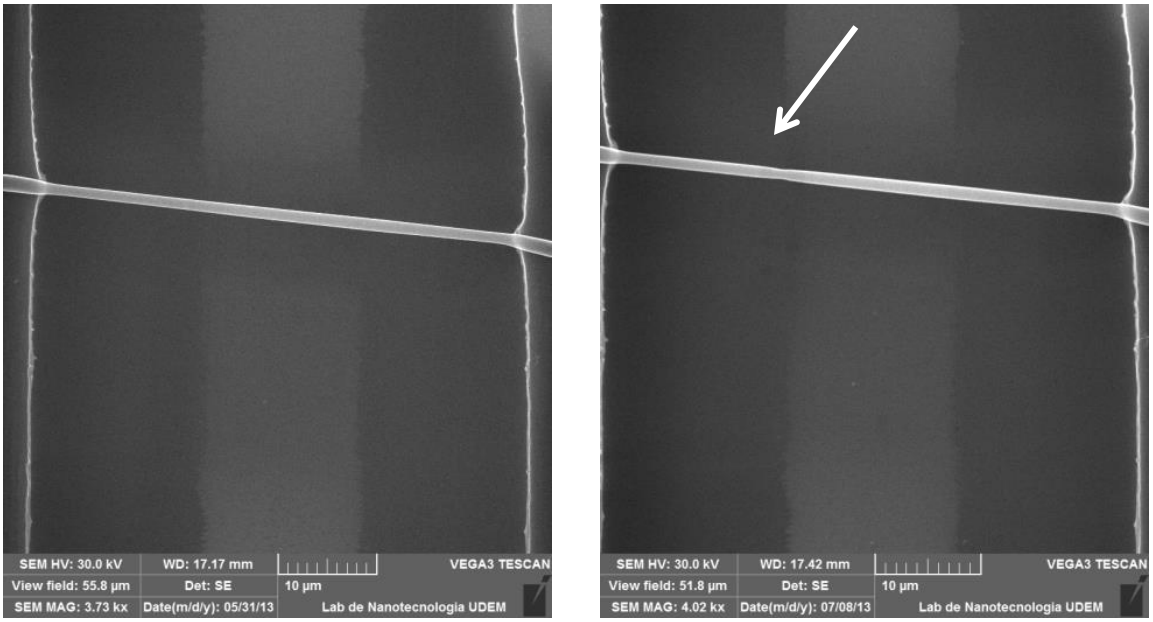

(a) **(b)**

Figure 6.29: SEM images from: (a) Test 3 and (b) Test 12

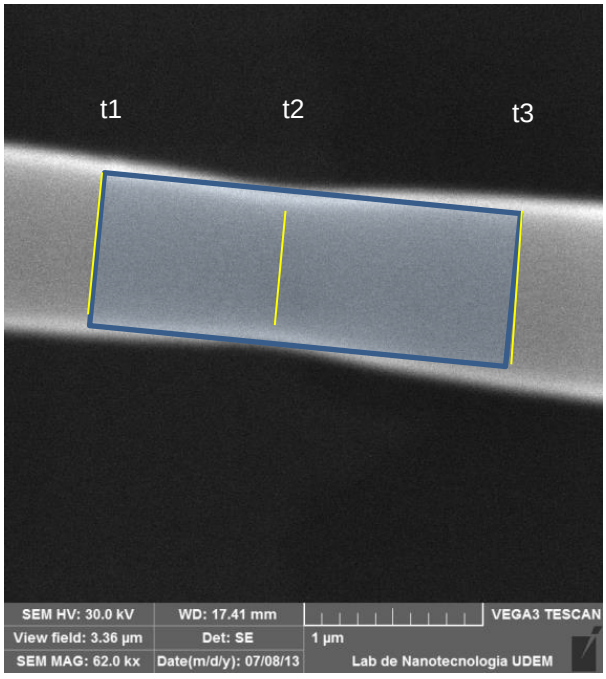

Figure 6.30: SEM images from Test 12, nanoconstriction

The figure 6.31 illustrates the recorded signals and parameters from Test 12: control voltage, electrical resistance, conductance, and current. As it can be seen, the slope for the control voltage signal ("Voltage from DAQ") changes at the moment in which a positive change in electrical resistance is detected. The time scale is the same for all the four inset graphs. This reduction in the ramp rate allowed for a much better control over the nanoconstriction formation. Figure 6.32 shows the power dissipation graph that illustrates a quadratic behavior up to detection of an increase in resistance. This ramp rate reduction induced a stop and reduced effect in the electrical current once the resistance change was detected.

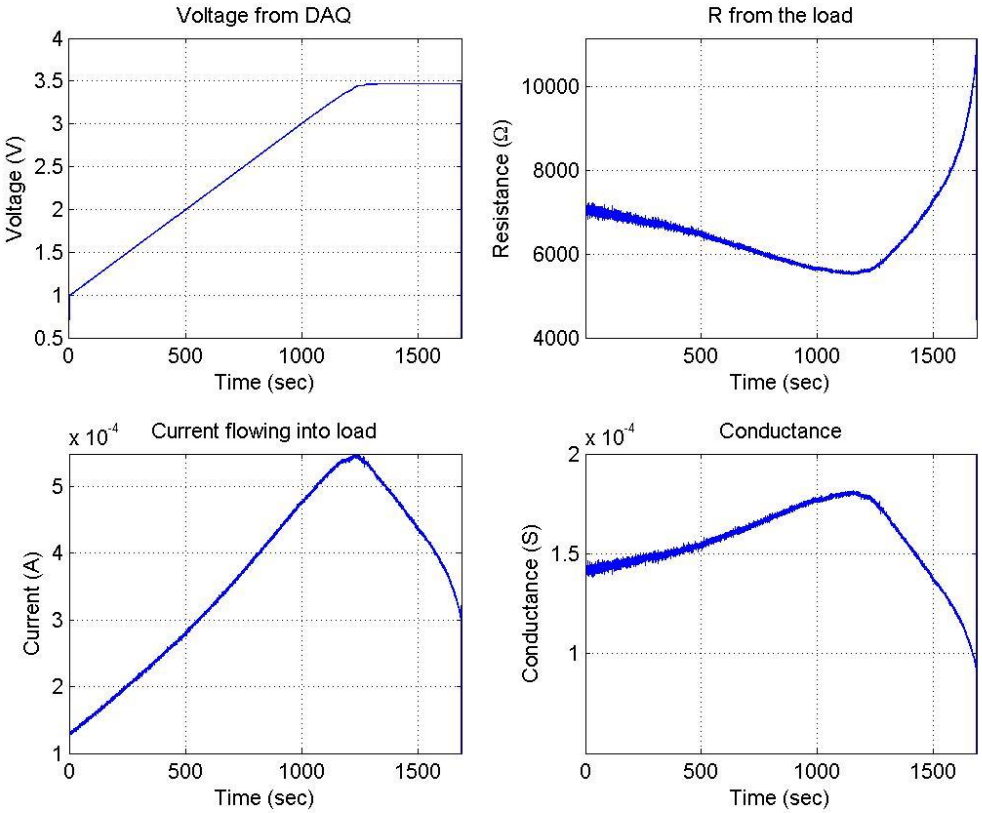

Figure 6.31: Recorded signals from Test 12, control voltage, resistance, conductance, and current

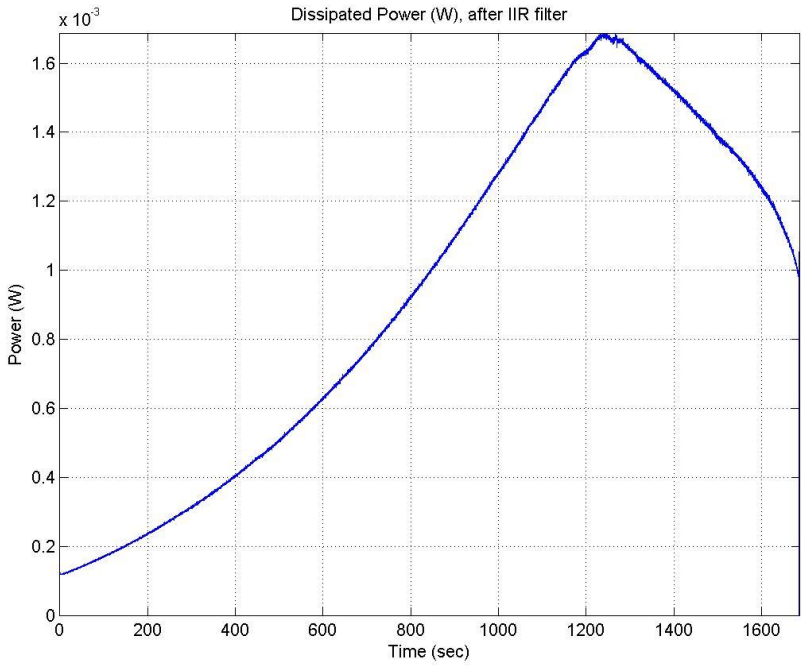

Figure 6.32: Power profile for Test 12

Figure 6.33 shows a bar graph with consolidation results obtained from the first set of experiments. The graph compares the dissipated power in mW from three different experiments using different samples of 1 μm in diameter. Figure 6.33 shows that for fibers of 1 μm in diameter, the dissipated power to generate a change at the middle of the fiber ranges from 1.7 mW to 1.9 mW. Therefore, the experiments performed over 1 μm fibers indicate an experimental maximum dissipated power threshold of 1.7 mW.

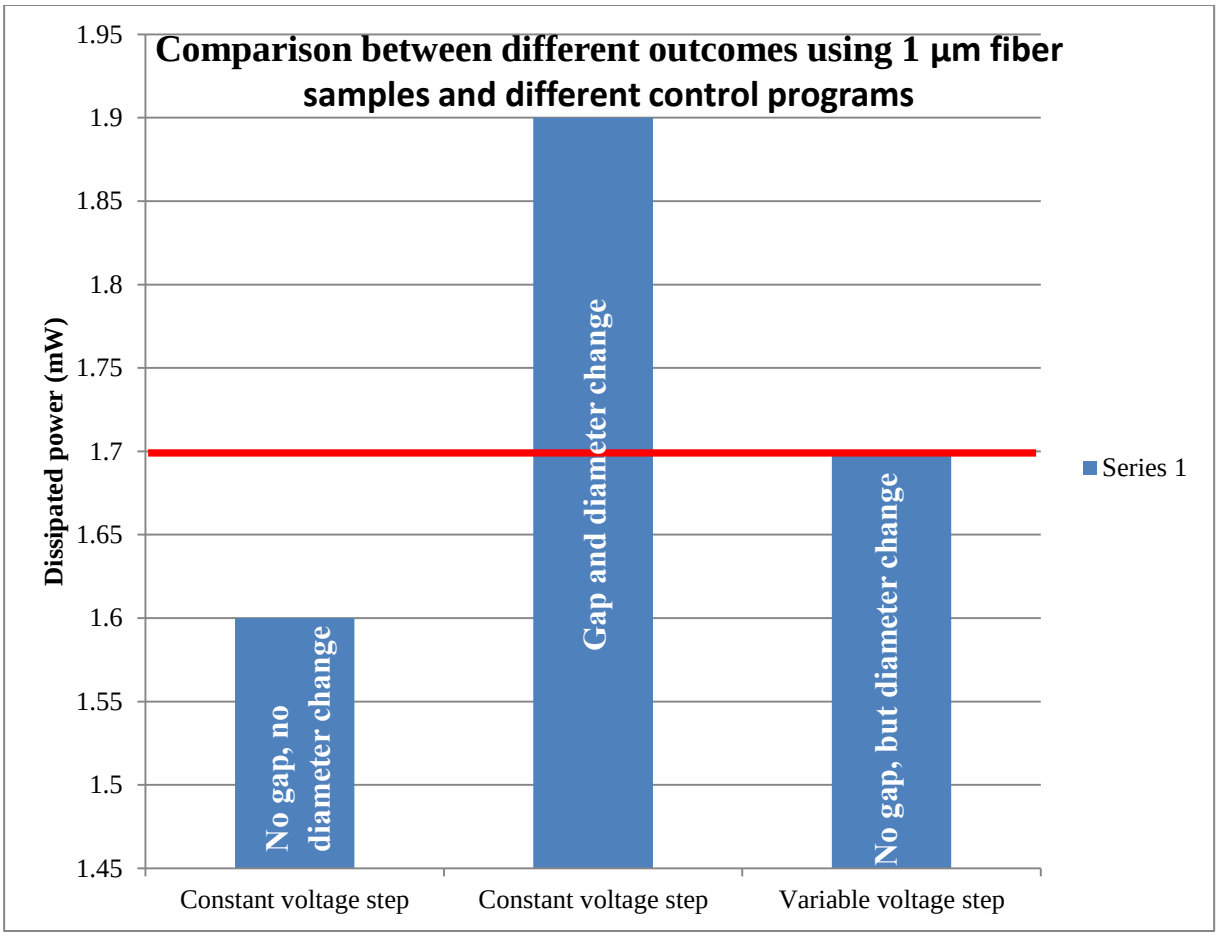

Figure 6.33: Experimental maximum dissipated power threshold for 1 µm fibers

Experiment Test 31 calls for a 2.44 µm fiber. The experimental conditions were the same as for Test 12. A small thickness constriction of ~170 nm to 197 nm was obtained with no gap formation. The maximum dissipated power reached was 6.1 mW. In figure 6.34 shows pre and post SEM view for this experiment. Figure 6.35 is a zoomed in view of the nanoconstriction for this sample, visual guides were also added. In figure 6.35, t1 is 2.514 µm, t2 is 2.317 µm, and t3 is 2.487 µm. The reduction obtained during this experiment corresponds roughly between 7% - 8% of the original fiber thickness at that point.

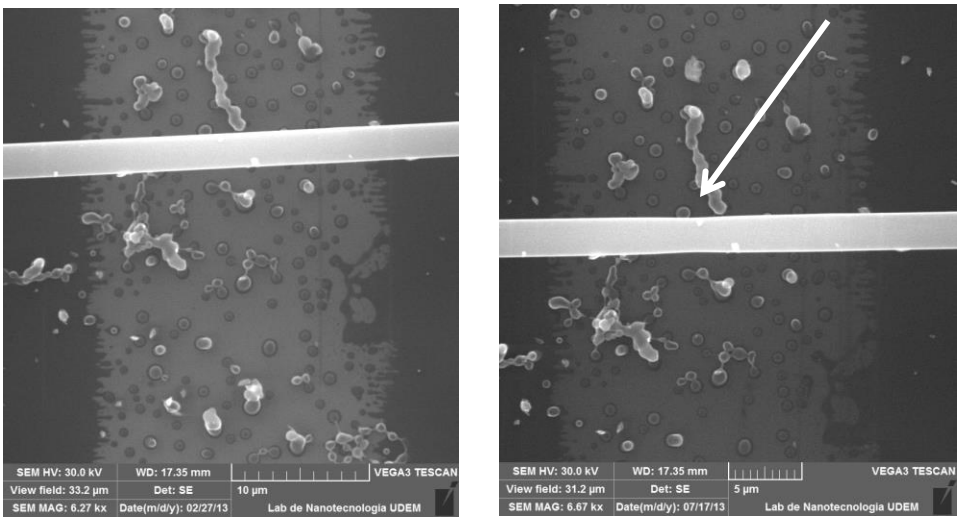

(a) **(b)**

Figure 6.34: Test 31 resulted SEM´s images for: (a) pre and (b) post esperiment

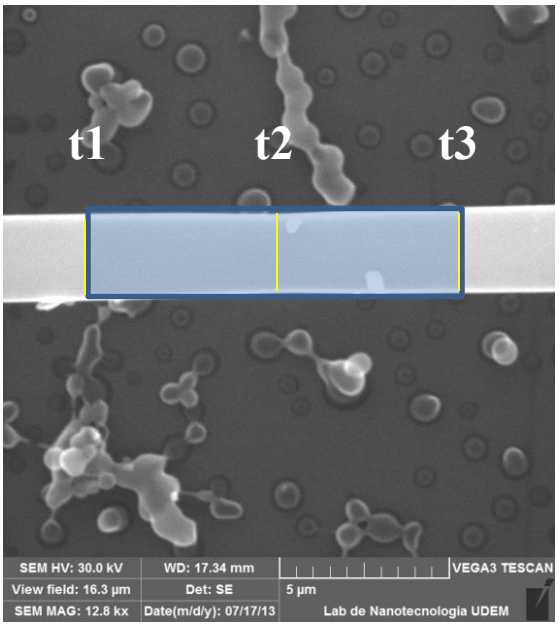

Figure 6.35: Zoom in view for nanoconstriction obtained in test 31

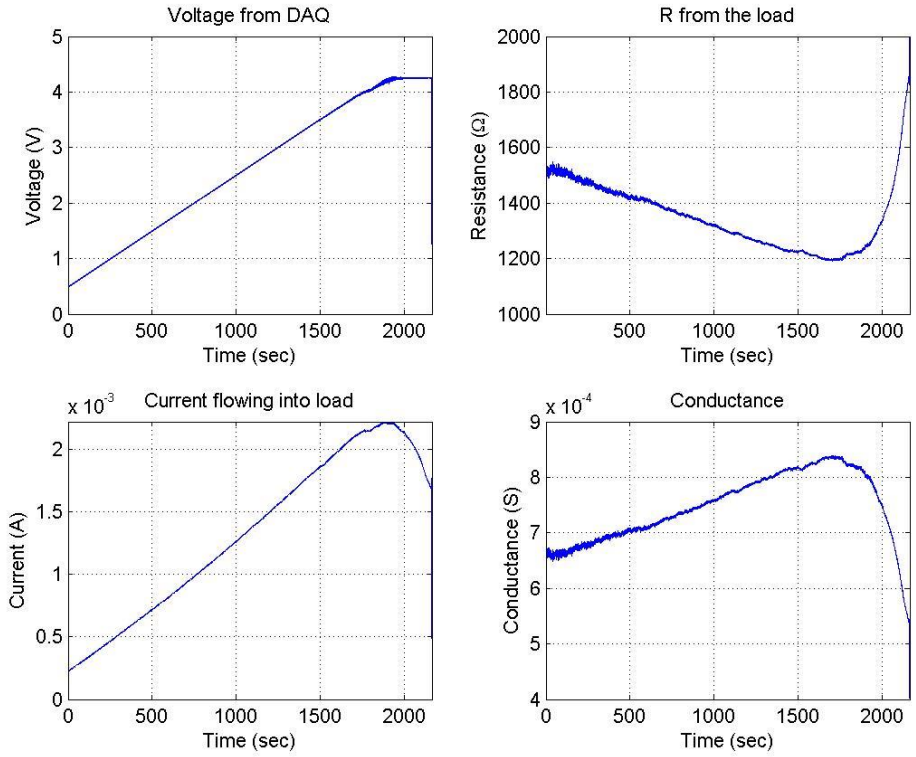

Figure 6.36: Recorded signals and parameters for test 31

Figure 6.36 illustrates signals and parameters recorded for Test 31. The graphs show the same shape as Figure 6.31 for Test 12. This sample has more than twice the diameter of the fiber sample in Test 12 (1 μm in thickness). Power and theoretical temperature profiles are described in section 6.4.

Test 31 presents a second situation where a controlled nanoconstriction was possible. This shows that controlled nanoconstrictions are possible if the appropriate experiment control is applied. In this case, 1 μm and 2.44 μm fibers resulted with nanoconstrictions generated artificially using electrical current flowing.

After Test 31, a question may be asked:

Is it possible to continue (further increasing) the same nanconstriction generated previously in the sample?

This question is answered by illustrating results from Test 34 that uses the same fiber sample and operating conditions as Test 31. Test 34 indicated that a further increase of a nanoconstriction is possible without reaching breakdown. Figure 6.37 shows the initial state for the fiber which comes directly after test 31, and the final state after test 34 in which the nanoconstriction has been augmented. The same magnification was used in both images for easy comparison. Figure 6.38 shows a zoomed in view of the augmented nanoconstriction for the Test 34.

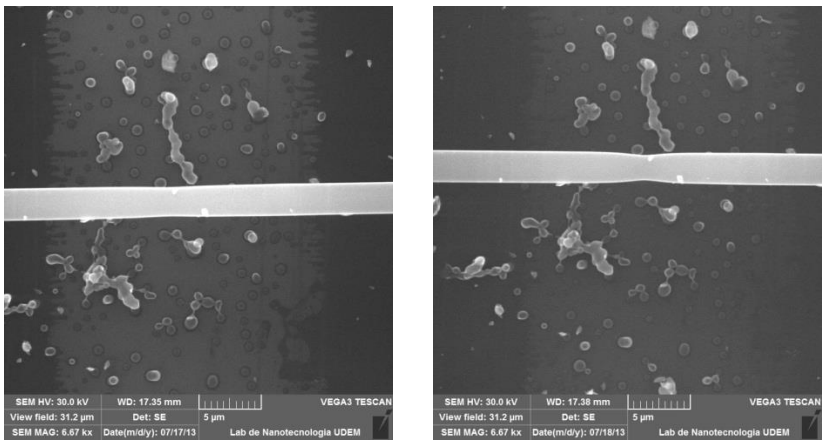

(a) **(b)**

Figure 6.37: Nanoconstriction: (a) after Test 31, and (b) after Test 34

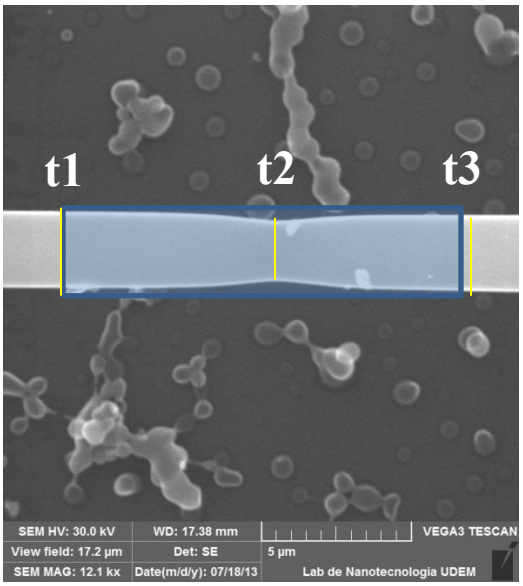

Figure 6.38: Zoom in view for Test 34

Mesurements in figure 6.38 are: t1 = 2.455 μm, t2 = 1.946 μm, and t3 = 2.455 μm. The reduction in thickness is ~509 nm. This reduction represents roughly 20.73% from the original fiber thickness after Test 31, at that particular point. The maximum dissipated power for Test 34 was 5.9 mW. This power is lower than the maximum reached in Test 31, indicating that fiber thickness limits the maximum dissipation that the fiber can sustain. The total amount of diameter reduction with respect to original fiber diameter is ~22.6% at the end of Test 34.

The results obtained in Test 34 proved that a controlled electrical experiment can drive a progressive nanoconstriction over a fiber sample under ambient conditions. Moreover, the maximum dissipated power is related to fiber geometry. In other words, a reduced diameter on the fiber sample required less power to continue its reduction, compared to its initial state.

6.4 Summary

This chapter described the experiments and tests performed to the nanofiber samples operating in free air. The experiment set up, instrumentation and hardware facilities are described and illustrated. Some modifications to the control program are also discussed. Experimental results show nanoconstrictions and nanogaps generated under electrical current control using the LabVIEW software and a dedicated data acquisition system. One fundamental outcome is the ability to control nanoconstriction progression over a nanofiber using electrical current control. The following chapter will present the nanofiber sample experiments performed using vacuum operating conditions.

Chapter 7

Nano-fiber Experiments for Vacuum Conditions

This chapter continues the description of experiments and the results obtained from the characterization and SEM observation of the glassy carbon nanofiber structure samples when exposed to vacuum operating environment. As mentioned previously, the instrumentation hardware and graphical programing software is used to control and expose the nanstructures to a controlled vacuum condition using a specialized chamber. The experiments and tests generate several nanostructure phenomena such as constriction, breakdown, nanogap and glowing generation under vacuum operation.

7.1 Experimental Setup under Vacuum Conditions

Contrary to the experimental setup from section 6.2.2 in previous chapter, the experimental setup in vacuum removes the oxygen from the ambient during the experiments. Removing the oxygen produces an environment in which the fiber may sustain longer the breakdown phenomena [47]. Some experiment results show a glowing phenomenon from the nanofiber itself. This phenomenon will be further described in this chapter.

Figure 7.1 shows a block diagram of the elements required to setup vacuum conditions. In this setup, no probe station was used because it was very difficult to include the micromanipulators inside the vacuum chamber. It was also difficult to use the microscope in order to attach the micromanipulator tips close to the suspended fiber. An ideal experimentation environment would be to have a vacuum chamber with embedded micromanipulators and a SEM. This way, the micromanipulator tips would be very close to the fibers, the electrical

resistance from the carbon walls would be minimized, and the experiment could have recorded live since a camera could have been easily mounted in the microscope. In fact, there are commercial SEM options to make this possible.

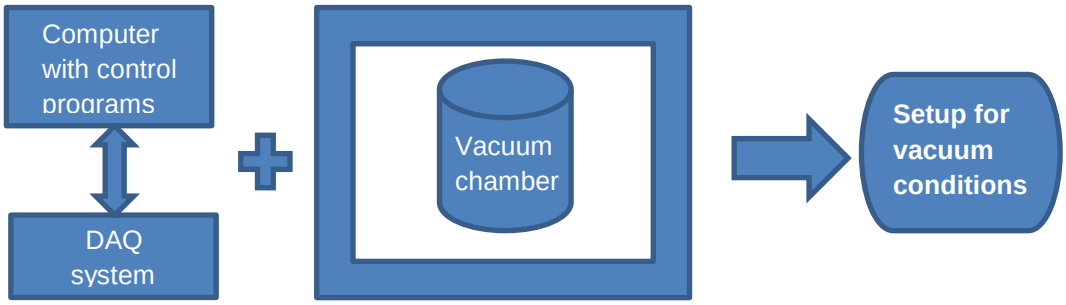

Figure 7.1: Setup for vacuum conditions

The equipment used as a vacuum chamber, available in the Engineering Labs at ITESM, is originally used in a carbon sputtering machine CED 030 [122]**.** This machine covers the non-conducting samples with carbon particles for SEM observations. In this setup, the DAQ system and associated instrumentation are interfaced with the nanofiber sample, inside the vacuum chamber, using a simple alligator clips connection inside the vacuum chamber. The vacuum chamber input / output ports are sealed with silicon. Figure 7.2 illustrates the vacuum chamber used for the experiments. The pressure that the chamber reaches is 0.1 mbar.

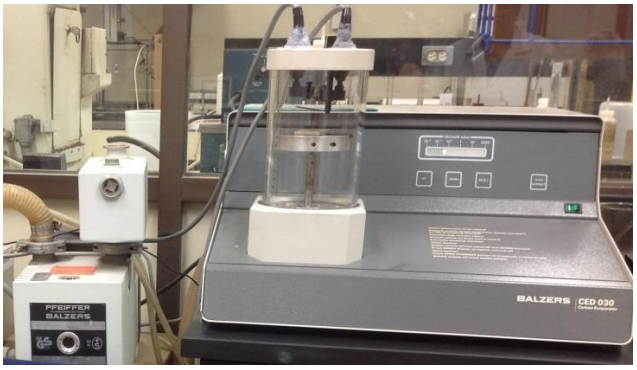

Figure 7.2: Vacuum chamber from carbon sputtering machine CED-30

7.2 Experiment Results for Sample Fibers Operating in Vacuum

Following the methodology described in section 6.2, the nanofiber experiments performed in vacuum were driven by the same control programs described previously in Chapter 5. The experiments were performed under the following operating conditions:

1. Vacuum conditions, performed once experience was gained for using the vacuum chamber at 0.1 mbars at T=25°C.
2. NI-DAQ data gathering system used to perform the data collection tasks and LabVIEW programming to drive the control over the electrical variables. The data acquisition procedures, data pre-processing and data post-processing were the same as for the free air operating condition tests.

7.2.1 Experiment results under vacuum conditions

A different set of experiments were run under vacuum conditions using the setup as explained in section 7.1. One of the objectives was to detect if any light emission was obtained from the suspended carbon fiber. This idea makes sense since the suspended carbon fiber in a vacuum environment is similar to the concept of a light bulb, except that instead of having a tungsten filament, a glassy carbon filament is now used. The samples under this setup will be exposed to the same methodology from section 6.3.1, using the slope voltage control program.

Two different samples were used to test this vacuum setup and to determine if glowing appears. Test 45 includes a sample holding multiple fibers with thickness ranging from 1.168 μm to 2.046 μm. The reason to use such a complex sample, in this first experiment, is that too few samples were available at the time of these initial vacuum tests and therefore a sacrifice sample was chosen.

Test 45 uses a vacuum pressure of 0.1 mbar. Also, silver paste was used to make electrical contact between carbon pads and alligator clips such that the external circuit (DAQ) have a

robust interaction with the sample. The experiment stopped because the voltage from the control signal reached 10 V, which is the maximum output voltage for the DAQ system used. No increase in resistance was observed during the experiment, and no fibers changes were registered after SEM imaging. The end result from this first experiment under vacuum conditions was that no glowing was observed. Figure 7.3 shows the results from Test 45, in which no change was detected in any of the suspended fibers that are visible in the corresponding SEM images.

It is difficult to analyze a sample with multiple and different contact points connecting the carbon wall electrodes. The electrical current going throughout each connecting structure, and therefore its power, are unknown under this complexity. Also, the total electrical current is divided between all the connection points between the carbon walls, making difficult to predict when the fibers reach a maximum dissipation. More power would be apparently dissipated on the nanofiber if the voltage reduces due to the resistance of the carbon wall electrodes. A new electrode design was planned to reduce the electrical resistance from the carbon walls and ohmic contacts. This avoids having a complex nanostructure with uncertainties in fiber residues that cause additional power consumption.

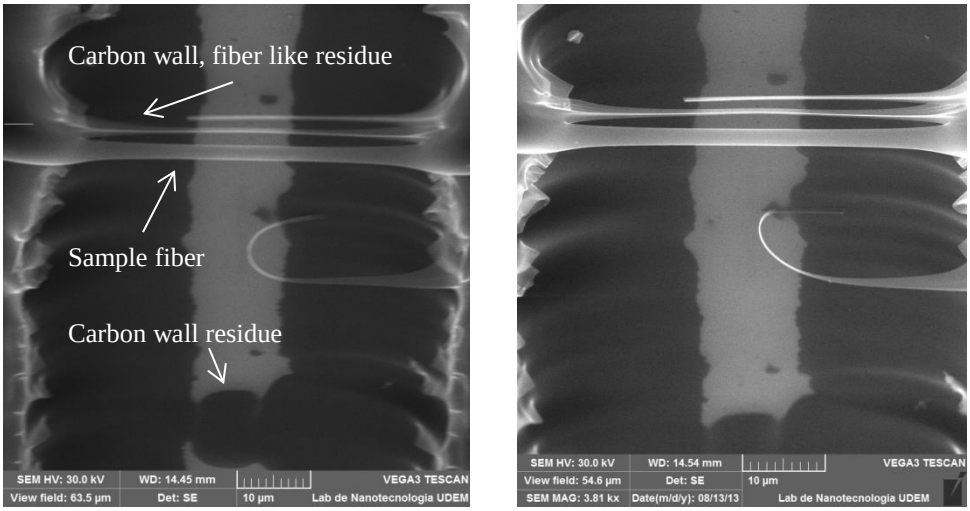

(a) **(b)**

Figure 7.3: Complex fiber sample: (a) before Test 45 and (b) after Test 45

The following experiment corresponds to Test 46. The sample fiber from test 46 had a diameter of ~2.12 μm, a vacuum operated at 0.1 m-bars and the same operating conditions as for test 12, test 31, and test 34. This time, a light emission (fiber glowing) was observed and recorded on video. The emission did not start right away but at approximately at the last part of the experiment. At the end of the experiment, the fiber broke due to an error in the initial configuration of the program. Figure 7.4 shows a sequence of frames from the video which captured the fiber glowing under vacuum conditions. Glowing intensity was higher as the voltage ramped up during the experiment.

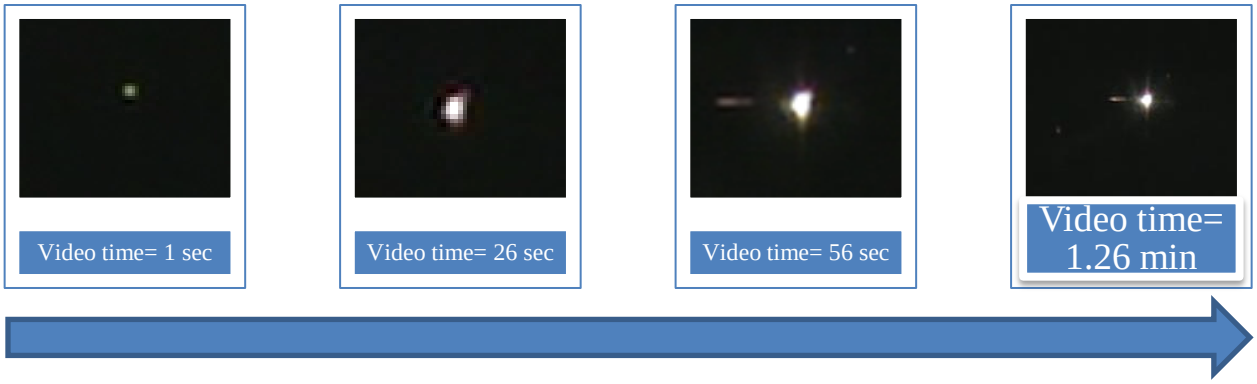

Figure 7.4 Glowing of the fiber under vacuum conditions

Figures 7.5, 7.6, and 7.7 show SEM images of Test 46:

1. At the initial conditions (before) and at end point conditions (after).
2. For the fiber having a zoomed view at 10μm and 1μm scales.
3. For the fiber having a 60° tilted view at 5μm scale.

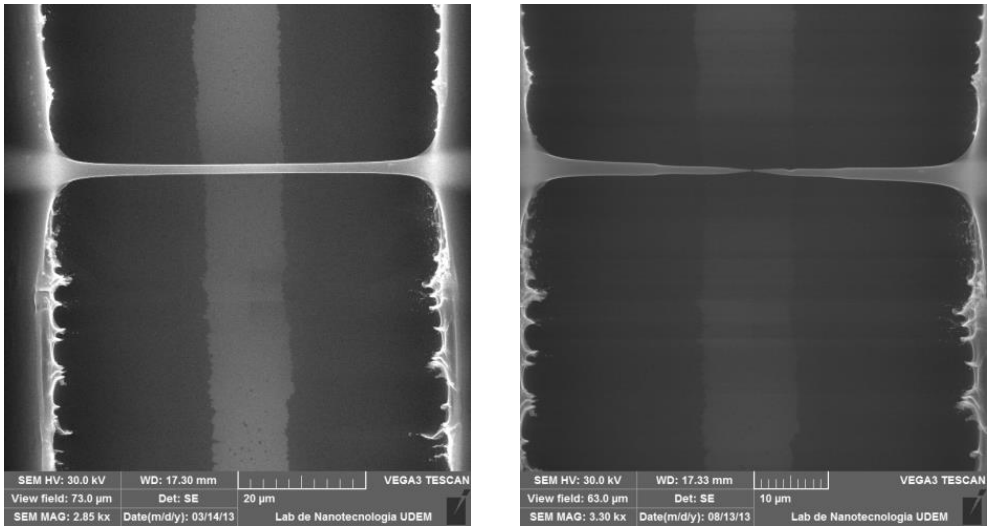

(a) **(b)**

Figure 7.5: Test 46: (a) before, and (b) after experiment

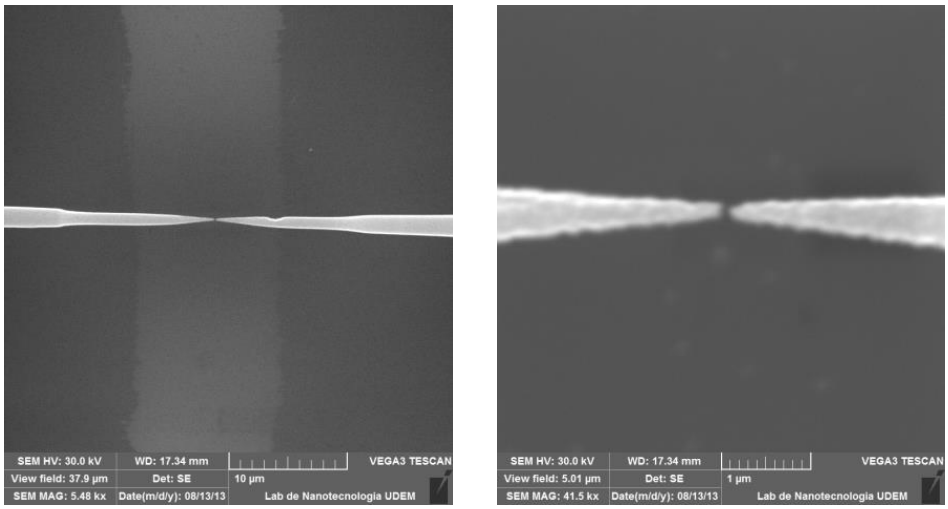

(a) scale 10 µm **(b) scale 1 µm**

Figure 7.6: Test 46, zoomed in views

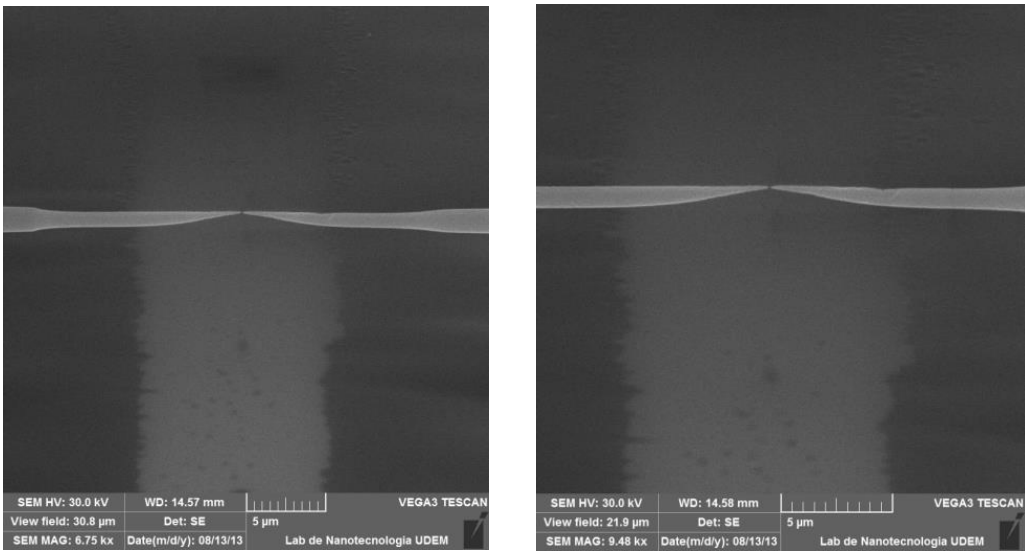

Figure 7.7: Test 46, tilted views (60^{o})

Figure 7.7 shows a nanogap in the suspended carbon fiber of ~ 78.95 nm. The reduction in diameter generated from its originally average of ~2.12 µm was 465 nm in thicker portions of the fiber to 1.98 µm close to the center of the suspended fiber. The image shows that the fiber is thinner close to the center which provides some evidence of the maximum temperature point during the experiment. This agrees with the Joule Heating model described in chapter 4. Figure 7.8 shows the recorded signals and parameters for Test 46.

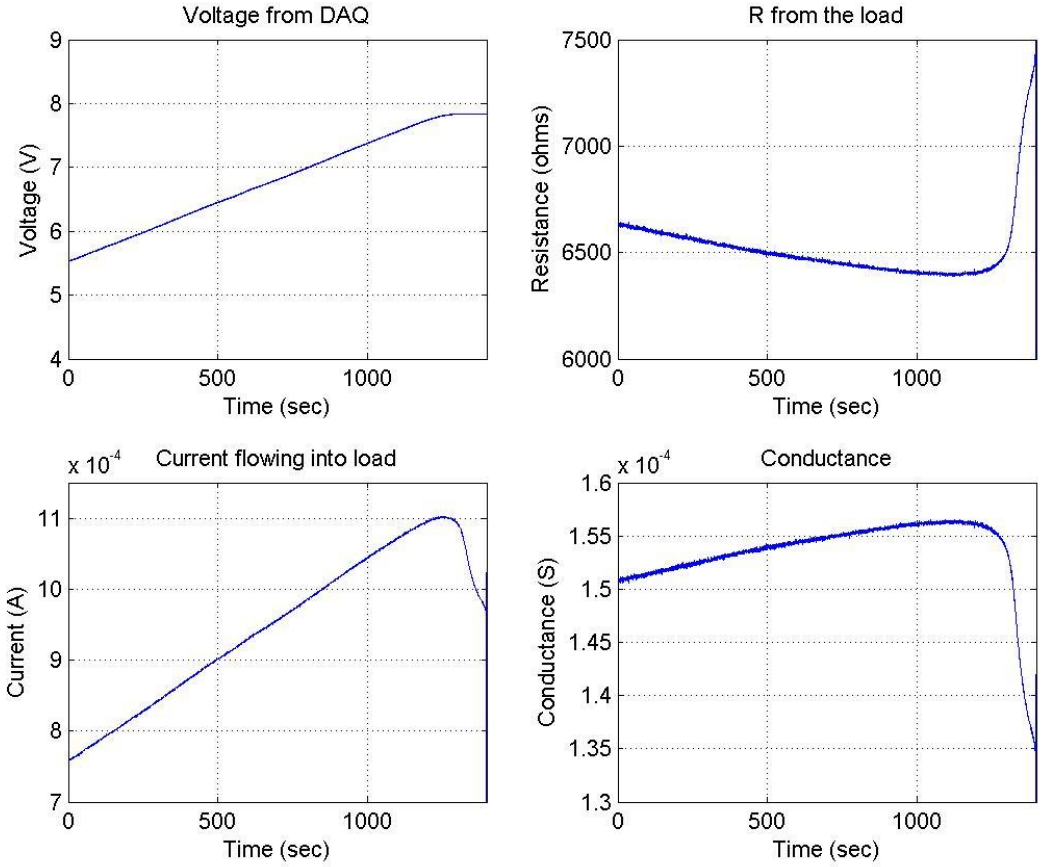

Figure 7.8: Test 46, recorded signals and parameters

Note that in figure 7.8, the signal behavior has the same shape as other experiments. The difference is that now the fiber glowed under vacuum conditions. This successful experiment gave the first evidence that glowing was possible from a suspended carbon nanofiber operating with a control current and under vacuum conditions.

A second sample was tested under vacuum conditions to try reproducing the glowing phenomenon. This experiment was Test 52 and the same operating conditions as for test 46 were used. The suspended carbon fiber had a diameter of ~1.22 μm and, again, a vacuum pressure of 0.1 mbar was applied. The fiber from this test also glowed but a glitch from the control program broke the fiber. The control signal went up again unexpectedly when it should have remained off. However, the glowing phenomenon was observed twice in Test 52. This evidence shows that

the phenomenon is replicable under those operating conditions. Figures 7.9 and 7.10 show the SEM test images before and after the experiment, and a close up view, respectively.

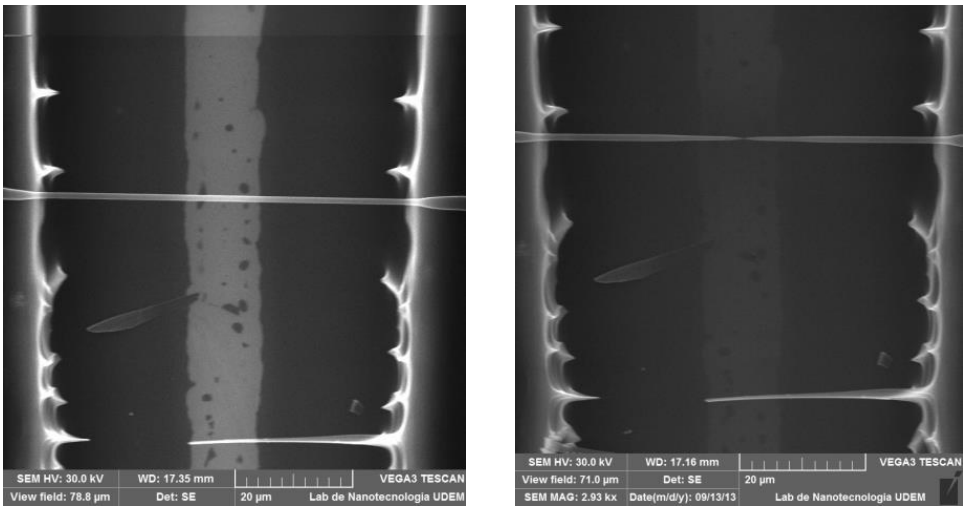

(a) **(b)**

Figure 7.9: Test 52; (a) before, and (b) after the experiment

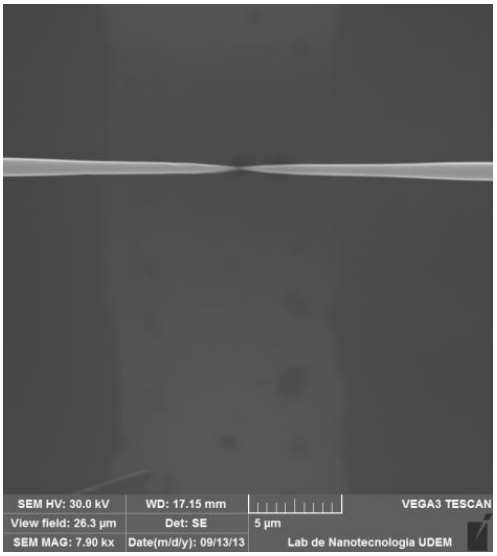

Figure 7.10: Test 52, zoomed in view

The gap size obtained after test 52 was ~91 nm. The carbon fiber gets reduced (original diameter 1.22 μm) by ~348 nm to ~991 nm depending upon the proximity to the gap. Again, the nanogap occurs at the middle of the fiber, reinforcing the argument that this point gets the highest temperature when an electrical current flow, according to the Joule heating model illustrated in chapter 4.

7.3 Power and Temperature Profiles

This section shows the power and temperature profiles from several successful experiments on which nanoconstrictions or nanogaps were generated. The profiles shown here include both, those obtained at free air and those obtained at vacuum conditions. This will provide a better insight of the electrical variables and dissipation needed to produce those changes regardless of the operating conditions.

Figure 7.11 illustrates the power profile for Test 2 and Test 12. They were run using ambient operating conditions and the same fiber sample. Test 2 did not show any variation on the suspended carbon fiber at a maximum dissipated power of 1.6 mW. A change in this particular sample came after Test 12, whose power profile is also shown in figure 7.11. This sample fiber changed only after the power went beyond 1.7 mW in Test 12. This characteristic illustrates that the carbon fiber exhibits an upper threshold power that induced a diameter change at the center of the fiber.

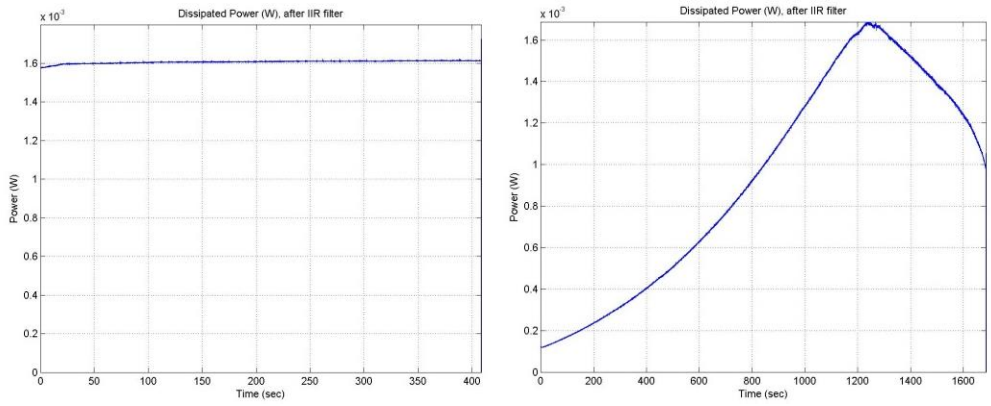

(a) **(b)**

Figure 7.11: Power profiles: (a) Test 2, and (b) Test 12

Figure 7.12 shows the power profile for Test 31 and Test 34. Again, they were run using ambient operating conditions and the same fiber sample. Test 31 illustrates a reduction in fiber diameter at the middle point of the suspended carbon fiber, but without generating a nanogap. Here, the maximum dissipated power was 6.1 mW. Test 34 shows a second reduction in fiber thickness, at the point. The maximum dissipated power for this second reduction was 5.9 mW, which is lower than the dissipation of Test 31. This shows that less electrical current was needed to induce a reduction on the carbon fiber for a thinner fiber when compared to a thicker one.

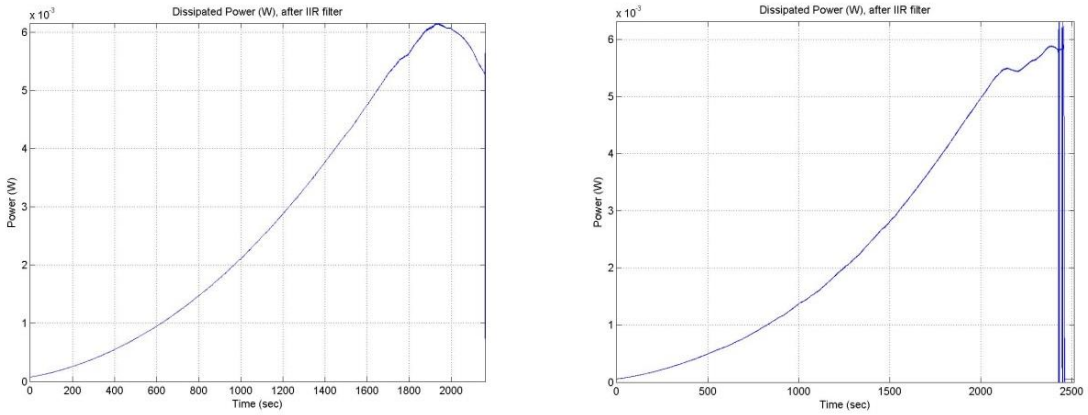

(a) **(b)**

Figure 7.12: Power profile for Test 31 (a) and for Test 34 (b)

Figures 7.13 and 7.14 show the dissipated power profiles from Test 46 and Test 52. Those tests were performed using vacuum operating conditions. The carbon fibers had initial diameters of ~2.12 μm and ~1.22 μm for Test 46 and Test 52, respectively. Figures 7.13 and 7.14 illustrate the expected outcome that the maximum dissipated power profile from Test 46 would have a higher peak than Test 52.

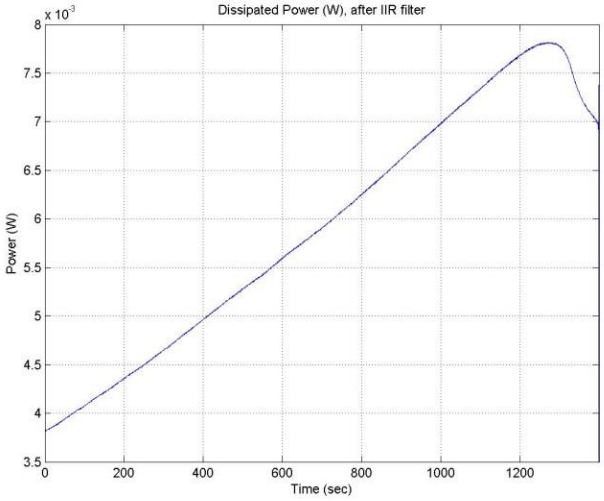

Figure 7.13: Power profile for Test 46

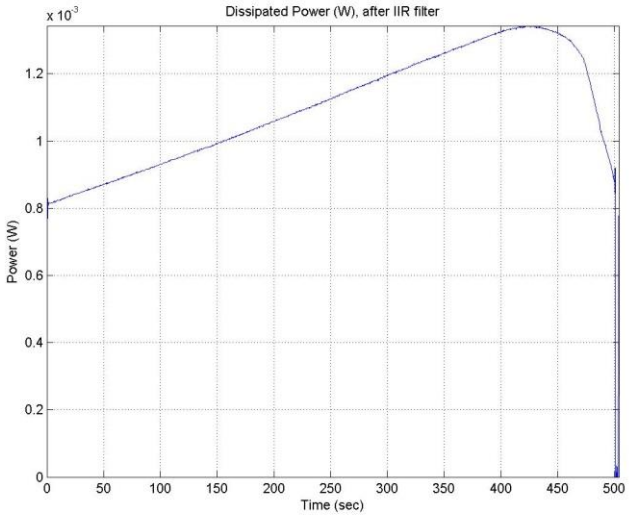

Figure 7.14: Power profile for Test 52

When comparing temperature profiles from different tests, an estimation of the maximum temperature can be made. For example, consider the temperature profile for Test 12 that appears in figure 7.11 (b). The dissipated power required to reduce this fiber at the middle portion was 1.7 mW. Using the recorded voltages and calculated current, nanofiber resistance, resistivity, and the equations from chapter 4 (equations 4.6 to 4.8), we can calculate the maximum theoretical temperature at the middle point of the suspended fiber. Figure 7.15 shows now the temperature profile indicating that the maximum reached temperature was around 3600°C. Now, the melting point for carbon is precisely that temperature and it was reached just at the moment when the dissipated power is at maximum. This appears to have the following implications:

1. If the electrical current sent throughout the carbon fiber reaches a maximum, then the carbon fiber constricts and reduces its thickness at the point of maximum heat.
2. Therefore, this point of maximum heat coincides at the middle of the suspended carbon fiber.
3. The experiment provides an initial validation of the Joule heating equations posed in chapter 4.

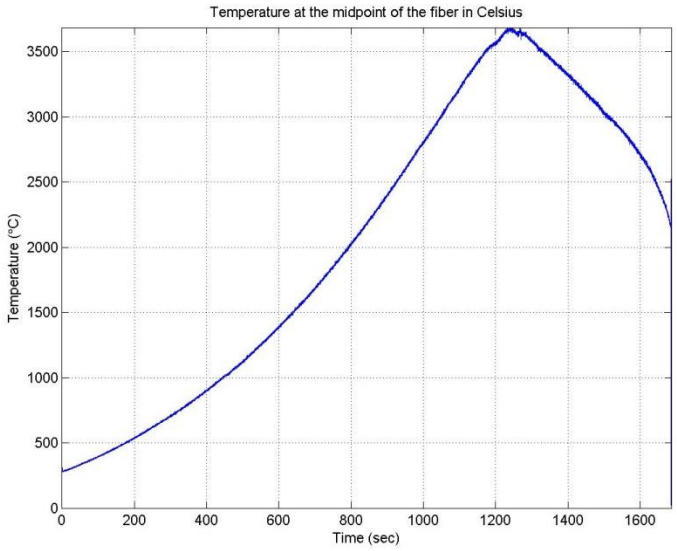

Figure 7.15: Temperature profile from Test 12

Consider now Test 46 performed under vacuum conditions. Figure 7.16 shows that the maximum theoretical temperature reached was again around 3600 ^{o}C when the power dissipated reached its maximum (figure 7.13). Let us now consider Test 52 with temperature profile appears in figure 7.17. The maximum theoretical temperature reached was again ~3600 ^{o}C when the power dissipated reached its maximum (figure 7.14). Those results are in agreement with test 12, and Test 46 as shown above. Note that the same equations were used to obtain both, the profiles shown in figures 7.15, 7.16, and 7.17.

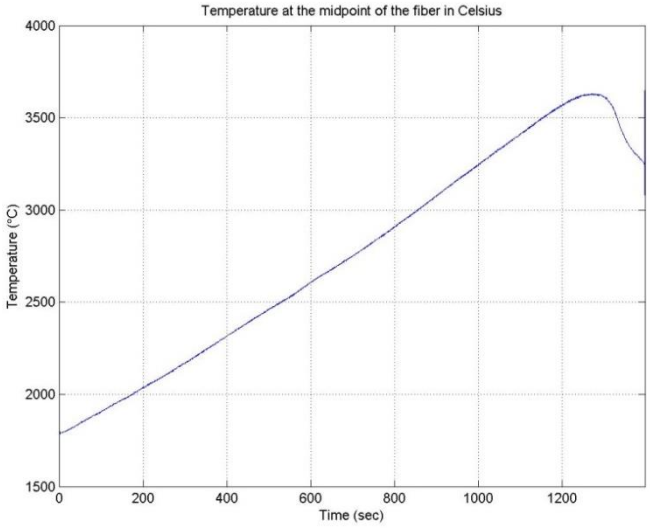

Figure 7.16: Temperature profile from Test 46

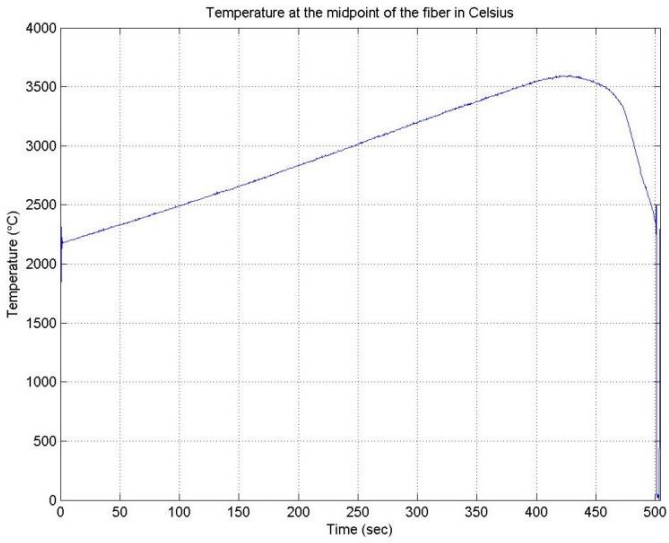

Figure 7.17: Temperature profile from Test 52

A truly exhaustive validation of the Joule heating temperature model could have been developed in this research, if a practical method to measure the physical temperature right at the middle of the suspended fiber would be available. However, the theoretical results obtained for the temperature profile on each experiment are all consistent. In other words, once the maximum dissipated power is reached the fiber will start to constrict and eventually break generating a nanogap (below 100 nm gap distance according to experimental data).

7.4 Proposed Modifications to Carbon Wall Electrodes

Previously, the electrode carbon wall design had an electrical resistance of around 2 kΩ per electrode. This electrical resistance is high to run experiments with suspended carbon fibers that have comparable electrical resistance. This implies that this electrode high resistance might overshadow small changes on the suspended carbon fiber performance. Therefore, the electrode resistance should be much smaller than the equivalent resistance of the fiber. An electrode design modification was proposed to decrease, as much as possible, the electrical resistance from the carbon electrode walls. Figure 7.18 shows the new electrode design proposed for the nanofiber sample experiments.

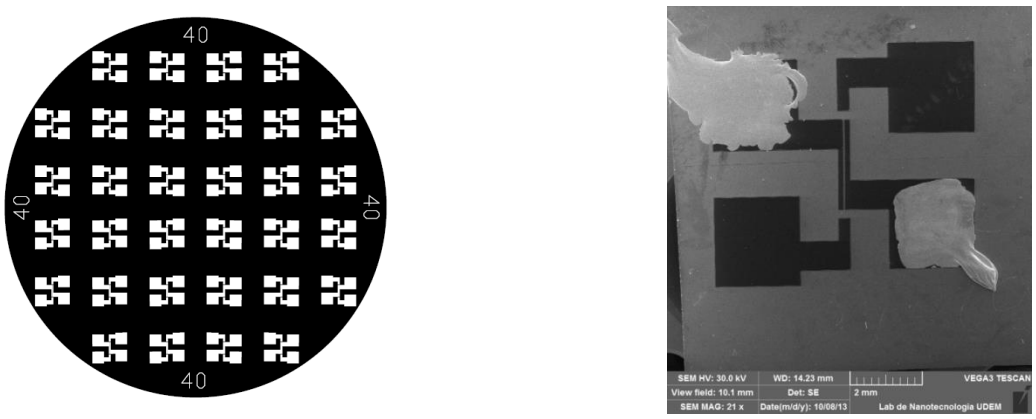

(a) Mask **(b) Electrodes with silver paste**

Figure 7.18: New electrode design

Tables 7.1 and 7.2 show the average diameter and their standard deviations from the top view and tilted view (60^{o}) of the suspended carbon samples from the new design for group 4 and group 5. Their respective lengths are depicted in table 7.3.

Table 7.1: Diameter and experimental characteristics of fiber samples from group 4

Sample #	Average diameter (μm) Top View, SEM;	Std deviation top view, SEM (μm)	Average diameter (μm) Tilted, SEM;	Std deviation tilted, SEM (μm)	Experiment name 1	Experiment name 2
1	1.1860	0.0667	1.1959	0.1172	Test 75	
2	1.3493	0.1809	1.2849	0.1390	Available for testing	
3	1.3105	0.1293	1.2880	0.2113	Test 68	Test 69
4	1.4463	0.0701	1.4591	0.1019	Test 66	
5	0.8707	0.0727	0.8802	0.0596	Available for testing	
6	1.1665	0.1784	1.1135	0.0789	Test 76	

Table 7.2: Diameter and experimental characteristics of fiber samples from group 5

Sample #	Average diameter (μm) Top View, SEM; group 1	Std deviation top view, SEM (μm)	Average diameter (μm) Tilted, SEM; group 1	Std deviation tilted, SEM (μm)	Experiment name 1	Experiment name 2
1	0.5498	0.0430	0.5789	0.0449	Available for testing	
2	1.2375	0.1745	1.1649	0.2149	Test 61	
3	0.5669	0.0952	0.6447	0.0992	Available for testing	
4	1.3650	0.2126	1.3400	0.1743	Test 62	
5	0.7194	0.0641	0.7420	0.0972	Test 64	
6	0.7964	0.0719	0.8059	0.0499	Test 77	
7	1.1293	0.1769	1.0309	0.1408	Test 65	

Table 7.3: Length of fiber samples from groups 4 and 5

Sample #	Length (μm) group 4	Length (μm) group 5
1	70.31	74.19
2	68.14	81.14
3	70.07	80.33
4	68.52	91.46
5	69.27	71.34
6	66.99	173.7
7		83.25

7.5 Steady State Experiment Results

A set of experiments in which the input control signal was held at fixed values was designed. The intention with this modification was to emulate a steady state for the temperature on the suspended carbon fiber and compare results with previous experiments using the variable change on the input control signal. For this "steady state" experiments, the input control voltage signal was held constant in the on state for 120 seconds, and then brought down to the off state for 40 seconds. The control signal was then increased in steps of 0.5 V after each cycle until the fiber would break or until a manual stop was activated.

Before the experiments on the real samples were run, a calibration step using a commercial resistor of 11 kΩ was performed. Figure 7.19 shows the results from this calibration. Only a few cycles up to the point of having 2 V in the input signal were used. After the calibration was completed, two samples from the new electrode design were chosen. One of the samples was left under ambient conditions, while the other sample was held at vacuum conditions during their respective experiments. Results from those first two experiments are shown as follows.

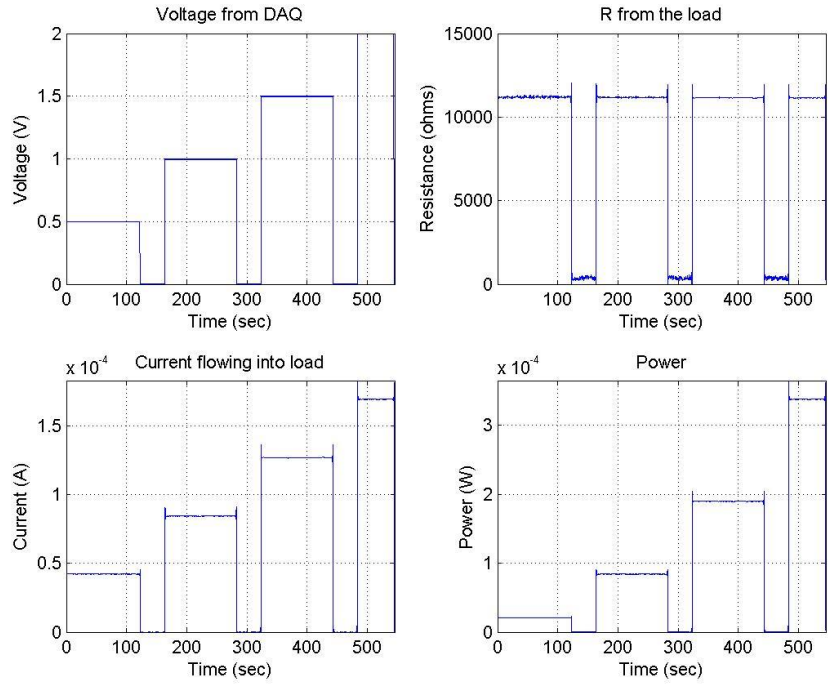

Figure 7.19: Calibration results for the steady state experiments

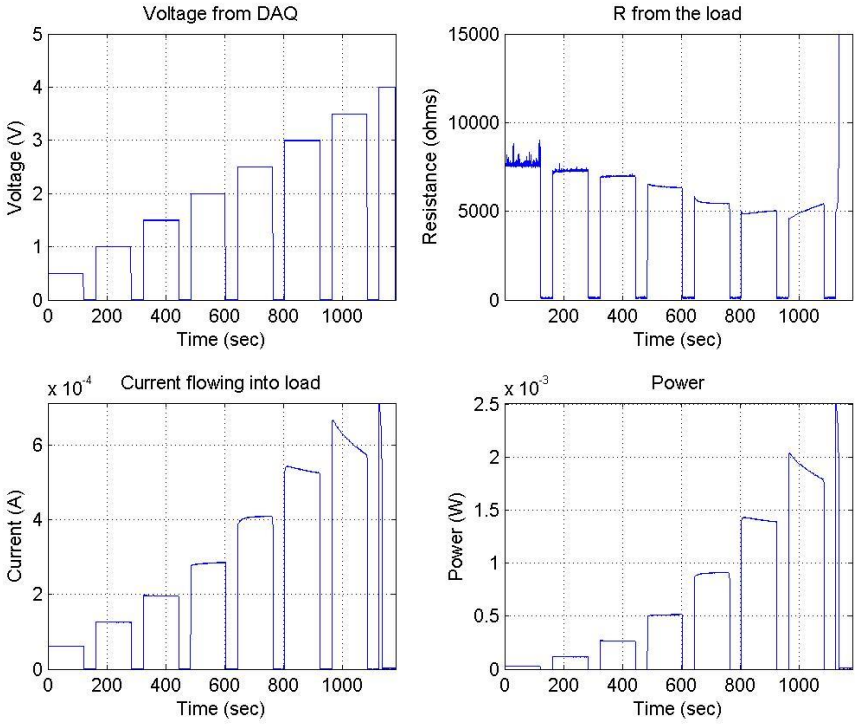

Figure 7.20: Test 61: Ambient conditions (open air)

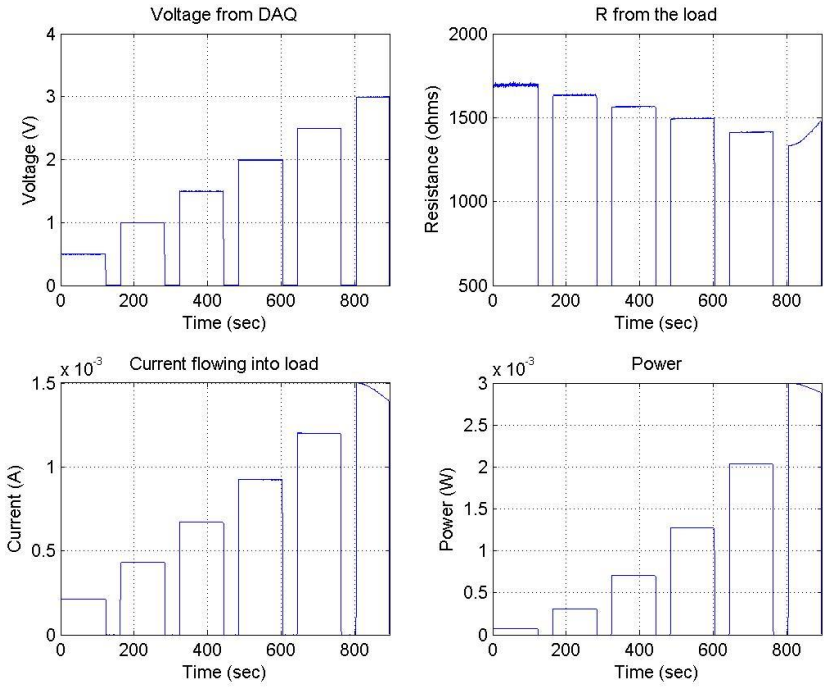

Figure 7.21: Test 62: Vacuum conditions

Figures 7.20 and 7.21 show the electrical resistance recorded from experiments 61 and 62, exhibing similar behavior than in previous experiments but with a different control signal. First, the electrical resistance decreases up to a minimum point which corresponds to a maximum dissipated controlled power (*before* fiber failure), and then it increases until it breaks (figure 7.20). In the case of Test 62, the experiment was stopped before fiber breaks. Both fibers were of similar sizes, Test 61 had a diameter of 1.2375 µm, and Test 62 had a diameter of 1.3650 µm.

Furthermore, the voltage required for both experiments to induce an increase in the electrical resistance measured was around 3 V to 3.5 V. The fiber that was held under vacuum conditions emitted visible light towards the end of the experiment. The fiber that was held under ambient conditions did not emit visible light. A notable difference was found regarding the electrical resistance from both samples. Despite its similarity in sizes, their electrical resistance is notoriously different. For the case of Test 61, its resistance starts around 8 kΩ but for the case of Test 62 it starts around 1.7 kΩ. This is indeed too much for a small change in diameter and it could also be atributed to fiber length and/or volume.

Figures 7.22, 7.23 and 7.24 show the SEM images for Test 61. As observed here, a small gap appeared after the fiber broke. The position of this gap is different from the middle position obtained in previous experiments. However, there was a particle (not shown) between the two electrode carbon walls that might have influenced the outcome of this particular experiment.

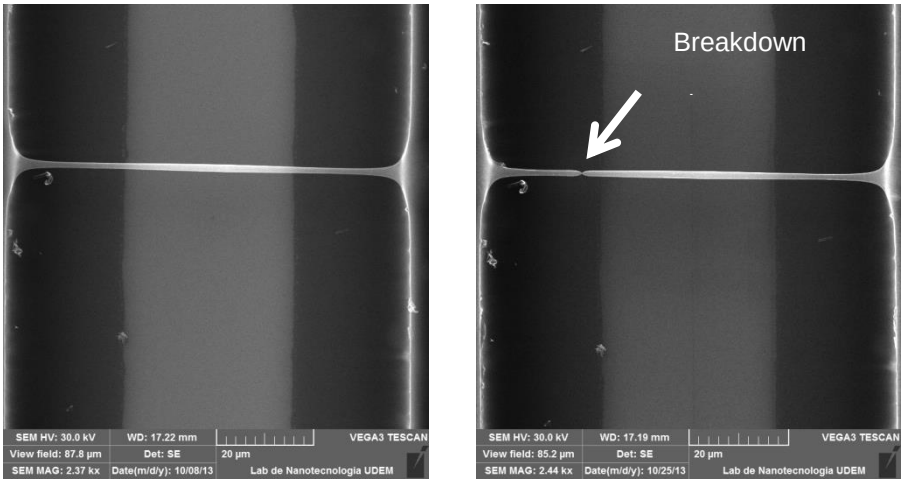

(a) **(b)**

Figure 7.22: SEM images for Test 61, (a) before and (b) after experiment

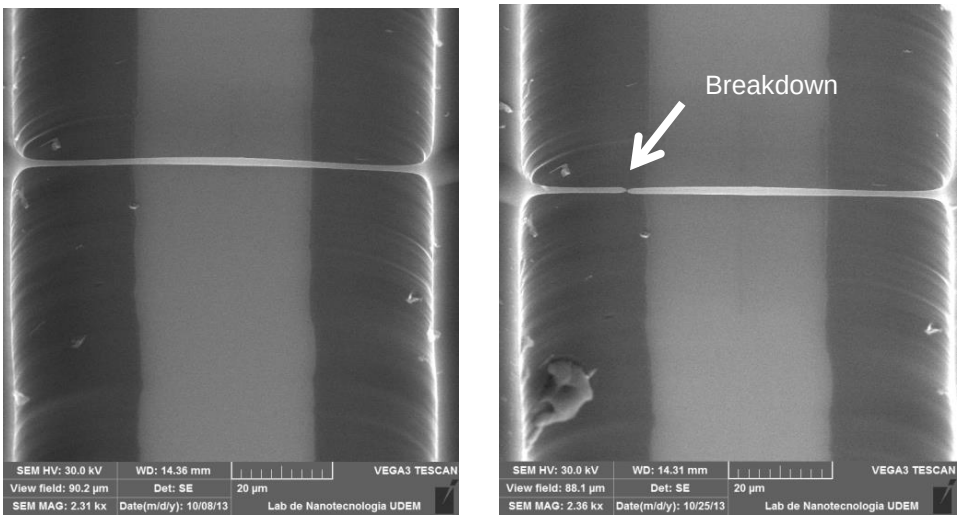

(a) **(b)**

Figure 7.23: SEM tilted images (60°) for Test 61, (a) before and (b) after experiment

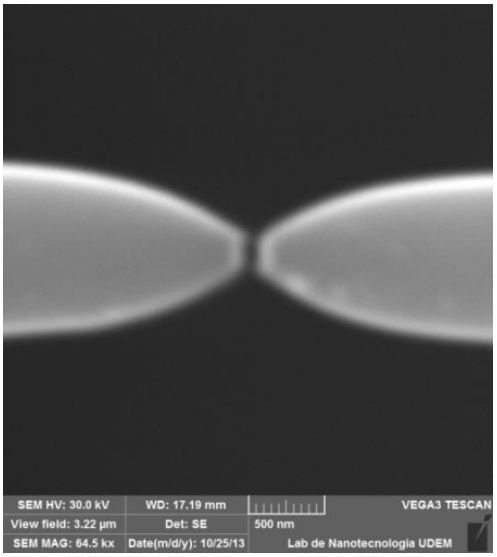

Figure 7.24: Test 61 SEM image, zoom in view of nanogap.

The gap obtained in Test 61 is about 100 nm. The fiber sample reduced approximately 1.0208 µm from an averge thickness of 1.2375 µm just before breaking.

Figures 7.25, 7.26, and 7.27 show results from Test 62. This experiment shows a new interesting phenomenon: the fiber underwent an observed bending towards the SiO_2 substrate.

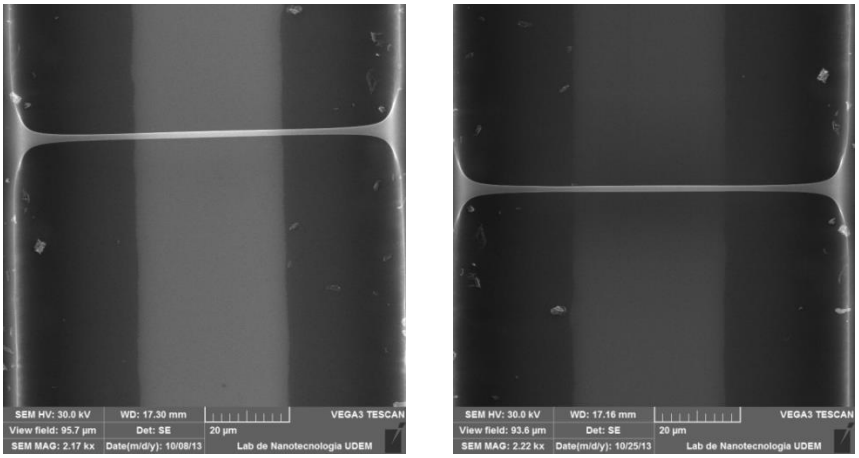

(a) **(b)**

Figure 7.25: SEM images for Test 62, (a) before and (b) after experiment

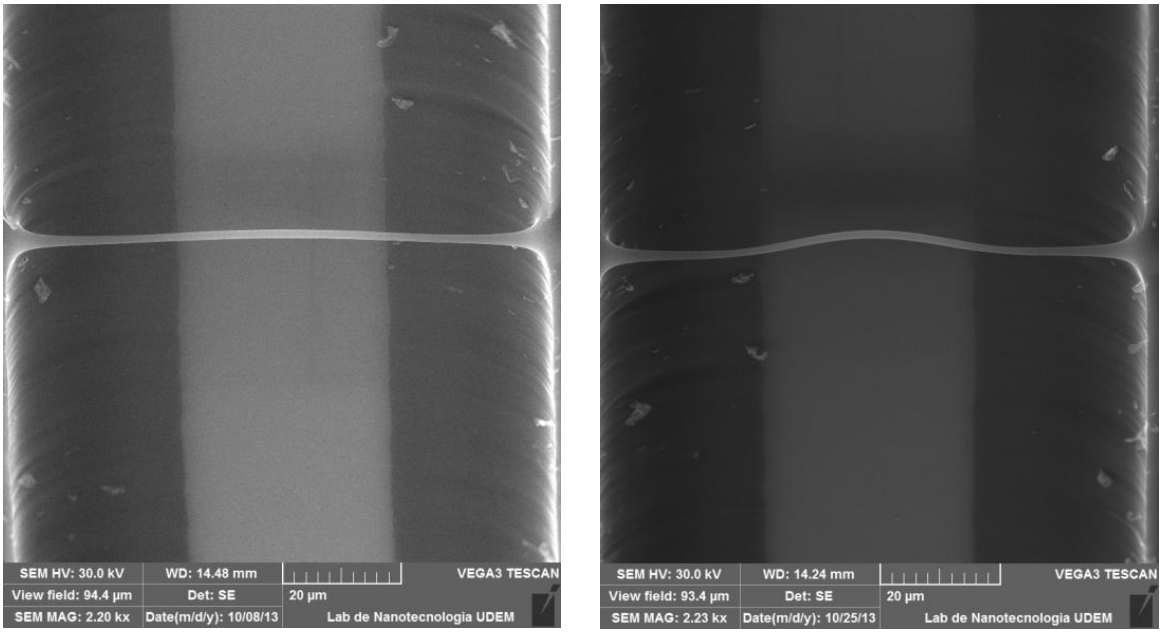

(a) **(b)**

Figure 7.26: SEM tilted (60°) images for Test 62, (a) before and (b) after experiment

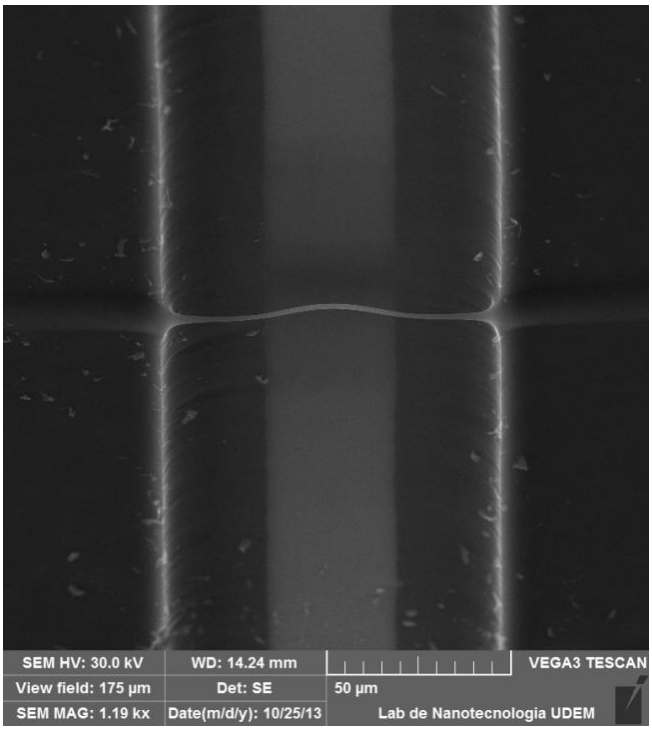

Figure 7.27: SEM image for Test 62 SEM, zoom out view

The fiber from Test 62 was not broken, instead it is still in one single piece as can be seen in figures 7.25 to 7.27, and electrically in figure 7.21. First observations suggest that the fiber might have elongated approximatelly 2.5 µm, from on original length (from around 86.49 µm to 88.97) µm. An explanation of this phenomenon could be that the fiber is reaching its melting point during the experiment, which generates a higher maleability to the fiber resulting in this bending effect. However further experiments must be run in order to elucidate the reasons for this phenomenon. The theoretical temperature in Celsius from Test 61 and Test 62 can be seen in figures 7.28 and 7.29 respectively.

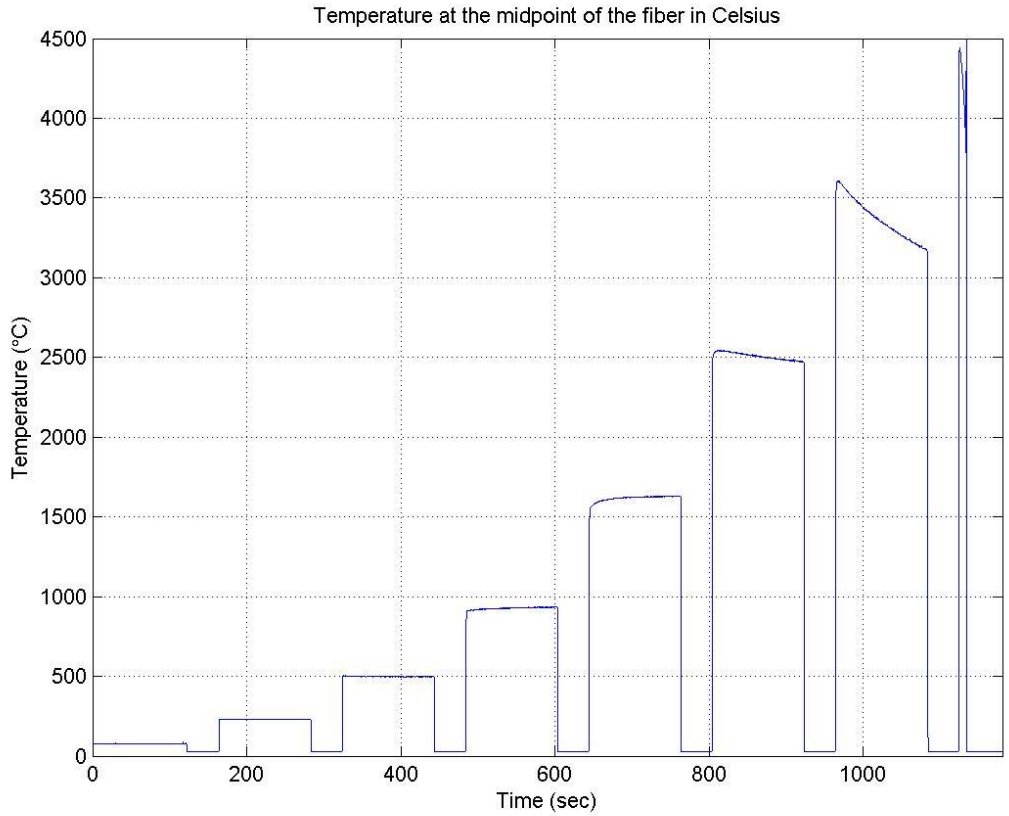

Figure 7.28: Theoretical temperature for Test 61

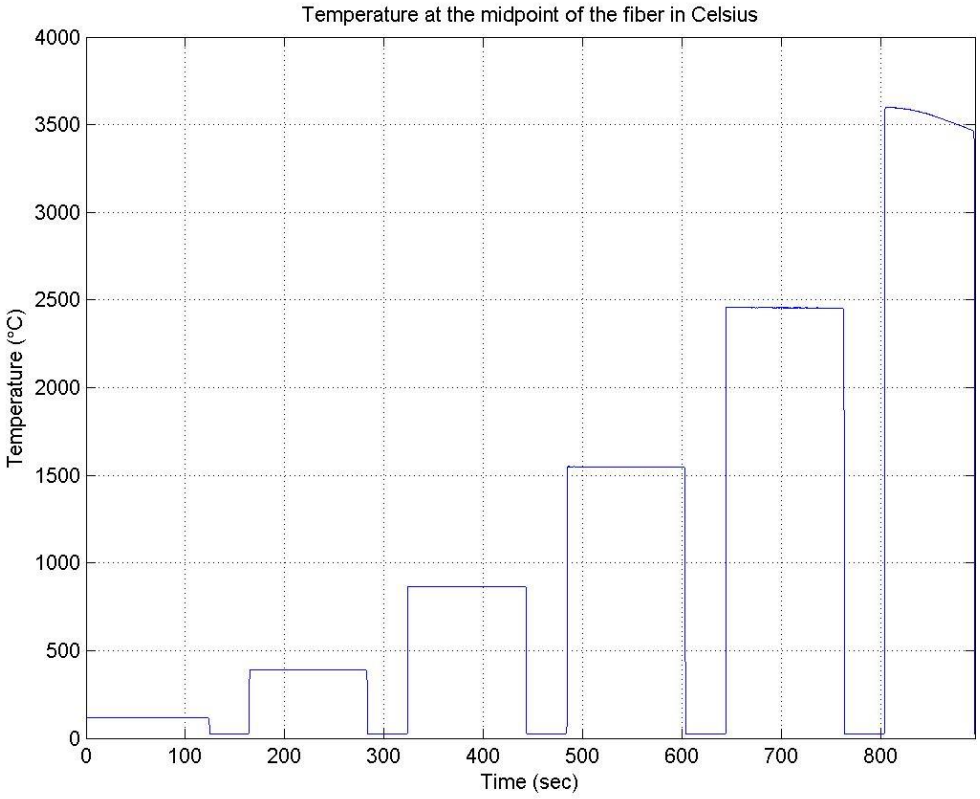

Figure 7.29: Theoretical temperature for Test 62

7.6 Comparison of Temperature and Dissipated Power

In this research, the model from section 4.1 has been used to show the theoretical temperature results from the experiments performed on the suspended carbon nanofibers. However, the theoretical temperature results differ from the model of section 4.1 if the temperature is modeled using the results from section 4.2. Figures 7.30 to 7.36 show the resulting temperature using the equations from section 4.2 for Test 12, Test 31, Test 34, Test 46, Test 52, Test 61, and Test 62.

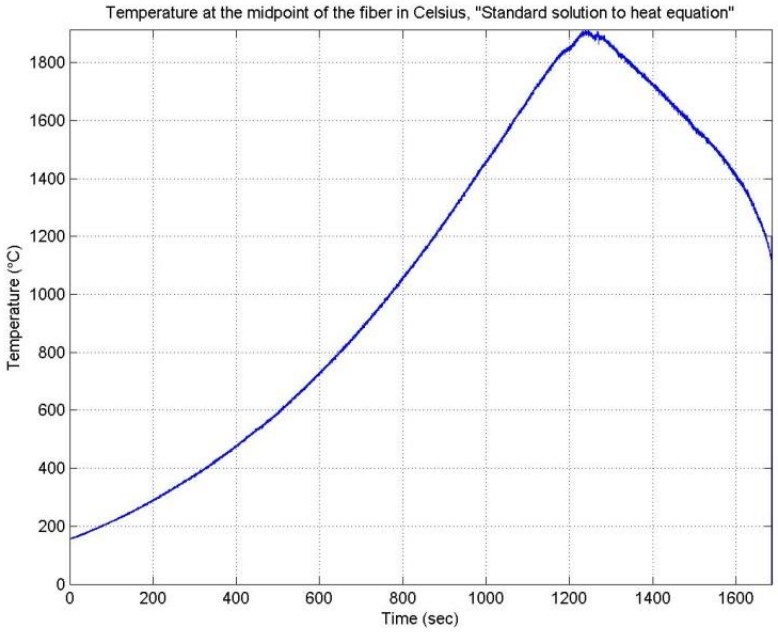

Figure 7.30: Theoretical temperature from Test 12 (open air)

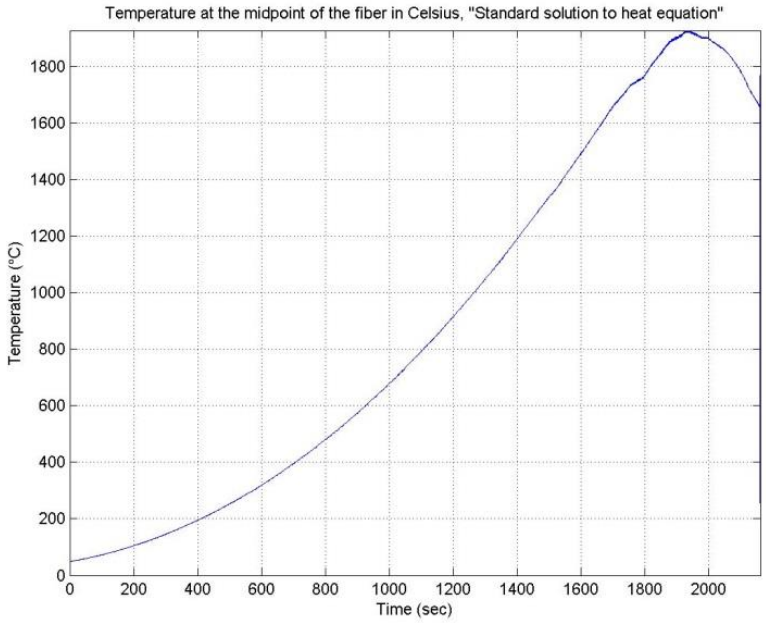

Figure 7.31: Theoretical temperature from Test 31 (open air)

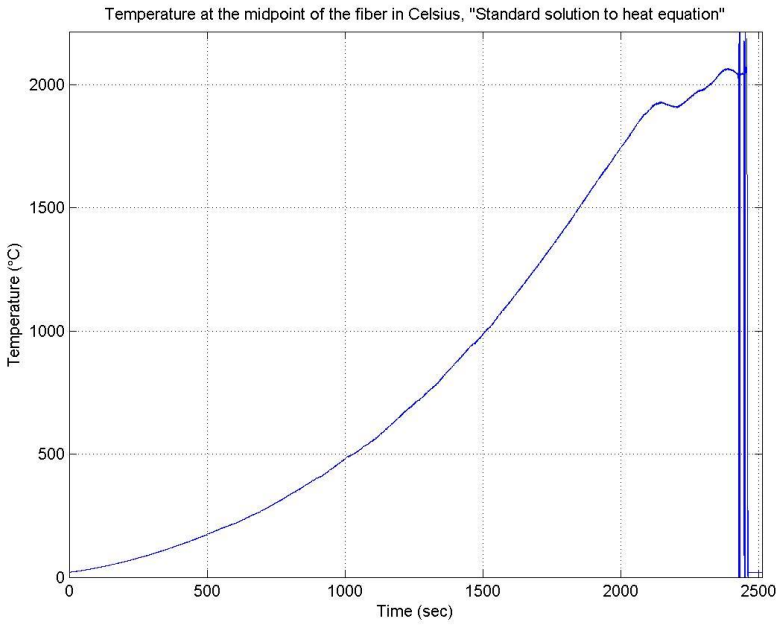

Figure 7.32: Theoretical temperature from Test 34 (open air)

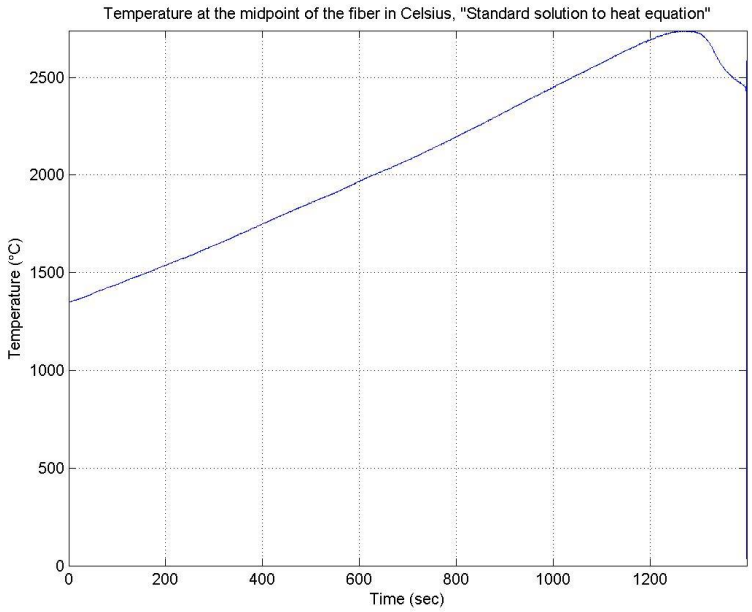

Figure 7.33: Theoretical temperature from Test 46 (vacuum conditions)

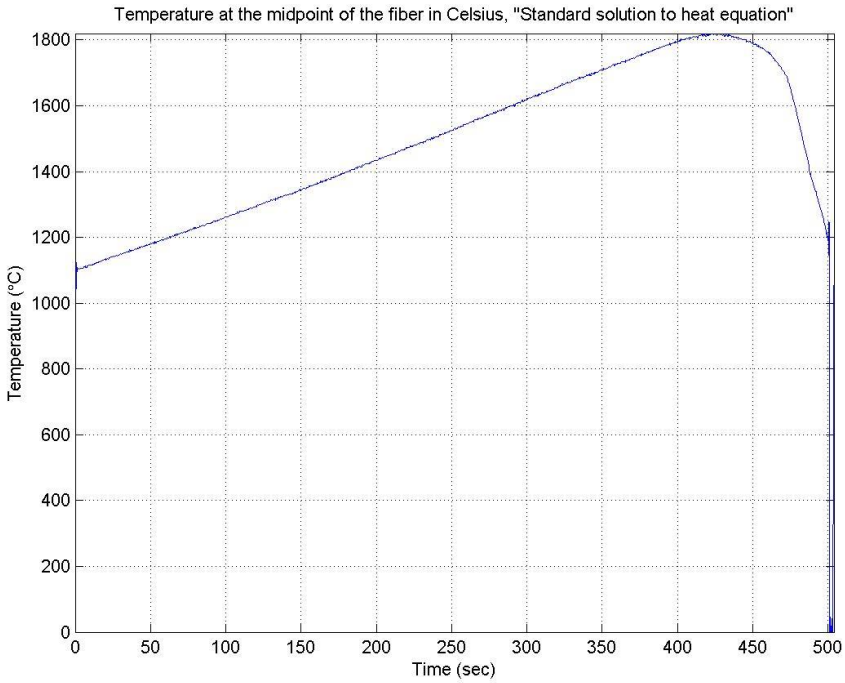

Figure 7.34: Theoretical temperature from Test 52 (vacuum conditions)

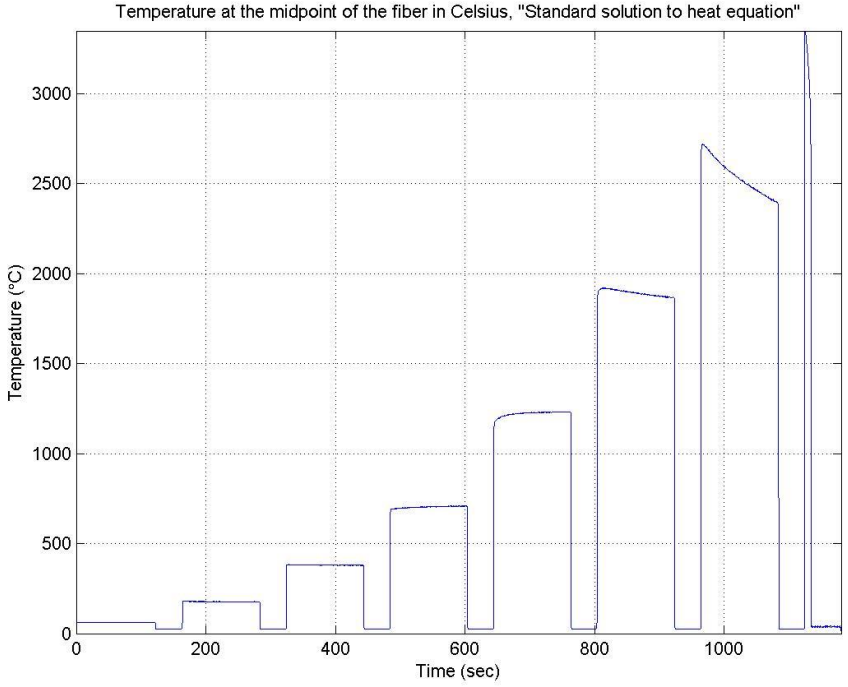

Figure 7.35: Theoretical temperature from Test 61 (vacuum conditions)

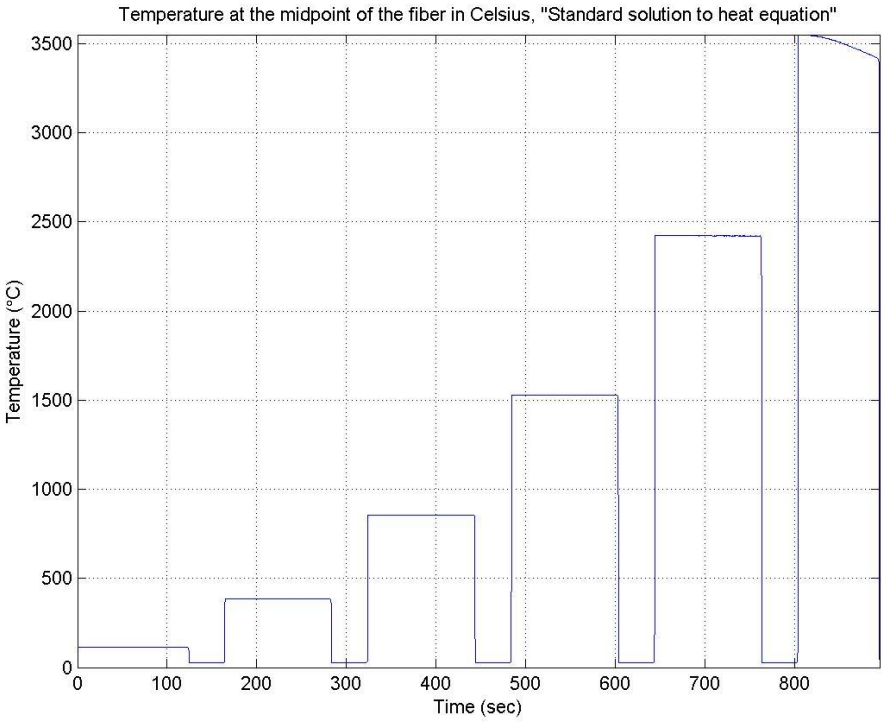

Figure 7.36: Theoretical temperature from Test 62 (vacuum conditions)

As can be seen from figures 7.30 to 7.36, the theoretical temperature reached using equations from section 4.2 is lower than using the equations from section 4.1 (~3600 ^{o}C). An exception to this observation is Test 62 which reaches 3550 ^{o}C. The theoretical maximum temperature reached from Test 12, Test 31, Test 34, Test 46, Test 52, Test 61, and Test 62 using equations from section 4.2 are summarized in figure 7.37. Notice that for experiments in open air conditions, the maximum temperature seems not to reach above 2000 ^{o}C. Also important to note is that the maximum theoretical temperature from experiments in vacuum conditions seems not to be below 2700 ^{o}C. An exception to this last observation is Test 52 which temperature is around 1800 ^{o}C. The electrical current for ambient and vacuum conditions is shown in figure 7.38.

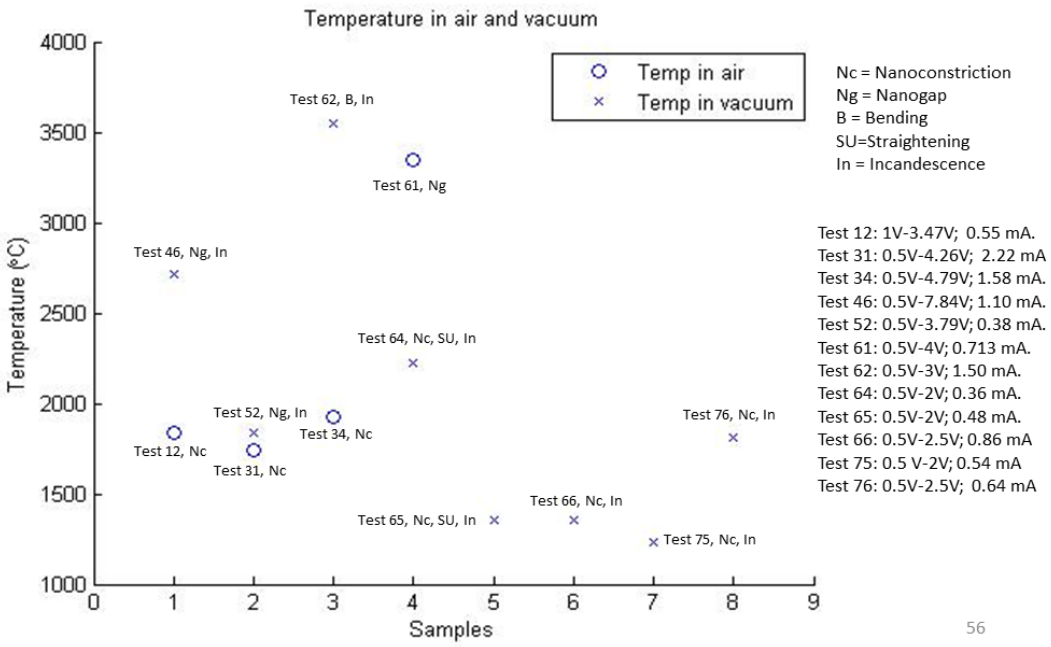

56

Figure 7.37: Theoretical temperature from air and vacuum conditions experiments

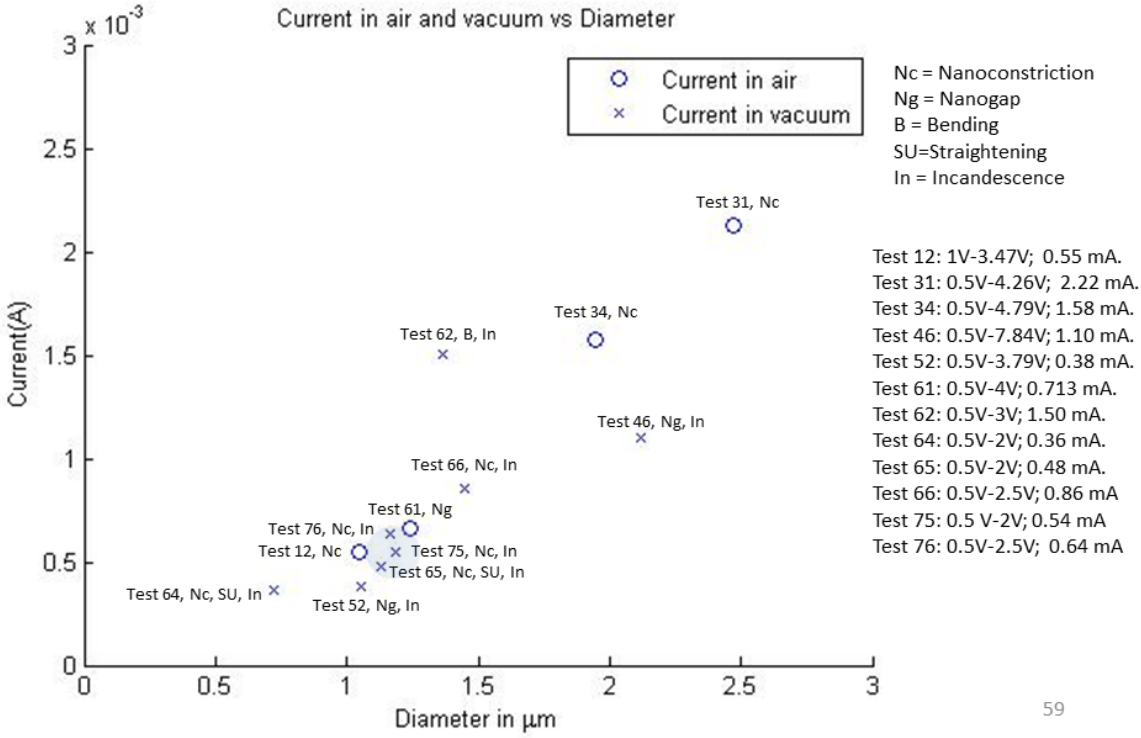

59

Figure 7.38: Current from air and vacuum conditions experiments

Figure 7.39 shows the dissipated power versus nanofiber diameter. As can be seen in this figure, there is a clear tendency for the dissipated power to increase as the fiber diameter is increased.

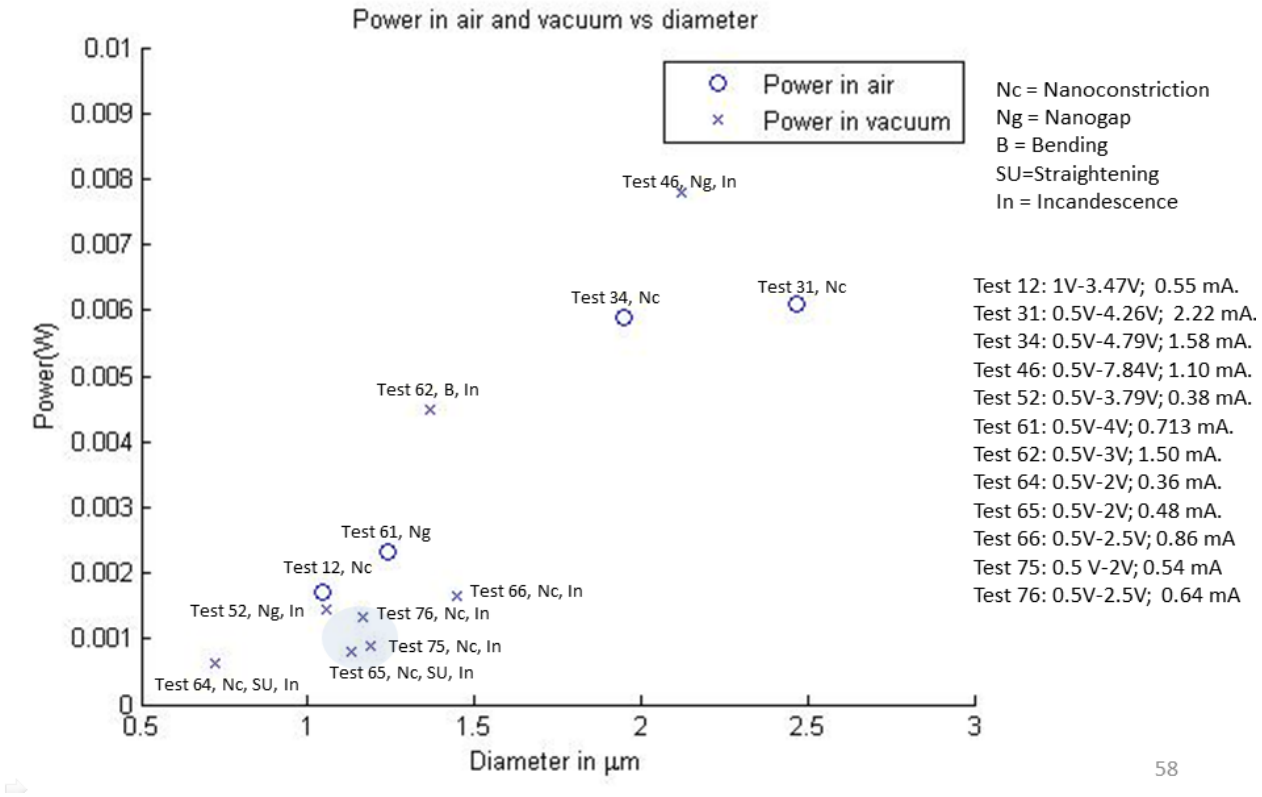

Figure 7.39: Power from air and vacuum conditions experiments vs nanofiber diameter

7.7 Summary of Experimental Result

Tables 7.4 to 7.7 show a summary of the characteristic parameters for experiments run both in vacuum and ambient conditions in which nanoconstrictions, nanogap, light emission and bending/straightening phenomena was observed. Experiments in bold were run in ambient conditions (25 ^{o}C and 50% humidity), experiments in non-bold were run in vacuum conditions (0.1 mbar and 25 ^{o}C).

Table 7.4: Nanoconstrictions

Name	D (µm)	L (µm)	V range (Volts)	I_{max} (mA)	P_{max} (mW)	J (A/cm^2)	R_{Lmin} (kΩ)	T (°C) (Model Results)	ΔD (nm)
Test12	**1**	**48.32**	**1 - 3.47**	**0.546**	**1.7**	**63.75e3**	**5.540**	**1803**	**200**
Test31	**2.44**	**74.56**	**0.5-4.257**	**2.220**	**6.1**	**46.32e3**	**1.195**	**1887**	**180**
Test34	**2.32**	**74.56**	**0.5-4.787**	**1.576**	**5.9**	**37.37e3**	**2.184**	**1817**	**509**
Test62	1.37	86.49	0.5 - 3	1.502	3	102.7e3	1.333	3550	164-338
Test64	0.72	70.32	0.5-2	0.364	0.639	89.5e3	4.845	2216	50-162
Test65	1.13	83.25	0.5-2	0.481	0.808	48.08e3	3.488	1357	115-337
Test66	1.45	68.52	0.5-2.5	0.855	1.65	52.02e3	2.259	1389	218-335

Table 7.5: Nanogaps

Name	D (µm)	L (µm)	V range (Volts)	I_{max} (mA)	P_{max} (mW)	J (A/cm^2)	R_{Lmin} (kΩ)	T (°C) (Model Results)	Gap (nm)
Test46	2.12	61.82	0.5 - 7.84	1.102	7.81	31.19e3	6.400	2738	79
Test52	1.22	64.98	0.5 - 3.79	0.380	1.34	32.49e3	9.232	1843	91
Test61	**1.24**	**80.17**	**0.5 - 4**	**0.713**	**2.51**	**59.29e3**	**4.634**	**3346**	**100**

Table 7.6: Incandescence

Name	D (µm)	L (µm)	V range (Volts)	I_{max} (mA)	P_{max} (mW)	J (A/cm^2)	R_{Lmin} (kΩ)	T (°C) (Model Results)
Test46	2.12	61.82	0.5 -7.84	1.102	7.81	31.19e3	6.400	2738
Test52	1.22	64.98	0.5 - 3.79	0.380	1.34	32.49e3	9.232	1843
Test62	1.37	86.49	0.5 - 3	1.502	3	102.7e3	1.333	3550
Test64	0.72	70.32	0.5 - 2	0.364	0.639	89.5e3	4.845	2216
Test65	1.13	83.25	0.5 - 2	0.481	0.808	48.08e3	3.488	1357
Test66	1.45	68.52	0.5 - 2.5	0.855	1.65	52.02e3	2.259	1389

Table 7.7: Bending (+) / straightening (-)

Name	D (µm)	L (µm)	V range (Volts)	I_{max} (mA)	P_{max} (mW)	J (A/cm^2)	R_{Lmin} (kΩ)	T (°C) (Model Results)	ΔL (nm)
Test62	1.37	86.49	0.5 - 3	1.502	3	102.7e3	1.333	3550	+ 2500
Test64	0.72	70.32	0.5 - 2	0.364	0.639	89.5e3	4.845	2216	- 190
Test65	1.13	83.25	0.5 - 2	0.481	0.808	48.08e3	3.488	1357	- 970

Tables 7.8, 7.9, and 7.10 show the characteristic parameters and partial results for the three main different programs that were used during this research (Chapter 5). Again, experiments in bold were run in ambient conditions (25 °C and 50% humidity), experiments in non-bold were run in vacuum conditions (0.1 mbar and 25 °C).

Table 7.8: Nanogap program parameter table (first program described)

Test name	RL initial (kΩ)	Initial Voltage (V)	Voltage Ramp (mV/sec)	ΔR Threshold	Stop Delay (sec)
1 µm fiber	**14.1**	**1**	**2**	**<1.5 R_{in}**	**200**

Table 7.9: Nanogap and nanogap program parameter table (second program described)

Test name	RL initial (kΩ)	Initial Voltage (V)	Voltage Ramp (mV/sec)	ΔR Threshold	Stop Delay (sec)
Test 12 (nanoconstriction)	**7.2**	**1**	**2**	**<1.5 R_{in}**	**524**
Test 31 (nanoconstriction)	**1.6**	**0.5**	**2**	**<1.5 R_{in}**	**449**
Test 34 (nanoconstriction)	**2.7**	**0.5**	**2**	**<1.5 R_{in}**	**385**
Test 46 (nanoconstriction)	6.6	0.5	2	<1.5 R_{in}	260
Test 52 (nanogap)	9.7	0.5	2	<1.5 R_{in}	127

Table 7.10: Steady state program parameter table: Nanoconstrictions, nanogaps, and deformation

Test name	RL initial (kΩ)	Initial Voltage (V)	Discrete voltage changes (V/160sec)	ΔR Threshold	Stop Delay Last Segment (sec)
Test 61 (nanogap)	**7.5**	**0.5**	**0.5**	**<1.5 R_{in}**	**8**
Test 62 (bending)	1.7	0.5	0.5	<1.5 R_{in}	88
Test 64 (straightening, nanoconstriction)	13	0.5	0.5	<1.5 R_{in}	34
Test 65 (straightening, nanoconstriction)	5.4	0.5	0.5	<1.5 R_{in}	58
Test 66 (nanoconstriction)	4.9	0.5	0.5	<1.5 R_{in}	57
Test 75 (nanoconstriction)	4.9	0.5	0.5	<1.5 R_{in}	62
Test 76 (nanoconstriction)	7	0.5	0.5	<1.5 R_{in}	56

Finally, table 7.11 shows results for experiments run under steady state in which nanoconstrictions were obtained. Repeatability of results for several experiments is summarized in table 7.12. It is important to notice in table 7.12 that all the samples have roughly the same average diameter. Furthermore, the nanoconstrictions obtained for Test 65 and Test 76 are remarkably similar for similar conditions, 337 nm for Test 65 and 363 nm for Test 76. These two experiments resulted in approximately the same nanoconstriction, giving very good experimental repeatability. Even more, using the methodology explained in this work, it is possible to tailor to some extent the degree of nanoconstriction obtained. For example, in Test 75 the nanoconstriction obtained was 215 nm, less than for Test 65 and Test 76. This result was obtained by automatically stopping the control program when the resistance change and current change slope were barely starting to change in direction, from negative to positive for electrical resistance, and from positive to negative for the electrical current.

Table 7.11: Steady state experiments

Test Name	ΔR_L (Ω)	ΔI (μA)	Delay Time (sec)	ΔR_L(Ω) / Delay Time (sec)	ΔI (μA)/ Delay Time (sec)	Average ΔD (nm)	Notes
Test 64 (0.72 μm)	+1529	-80	34	44.97	- 2.35	161 (22%)	Straightened
Test 62 (1.37 μm)	+159	-102	88	1.81	- 1.16	338 (25%)	Nanofiber bend towards substrate
Test 66 (1.45 μm)	+343	-91	57	6.08	- 1.60	335 (23%)	-

Table 7.12: Repeatability of steady state experiments

Test Name	ΔR_L (Ω)	ΔI (μA)	Delay Time (sec)	ΔR_L(Ω) / Delay Time (sec)	ΔI (μA)/ Delay Time (sec)	Average ΔD (nm)	Notes
Test 75 (1.19 μm)	+145	-20	62	2.34	-0.32	215 (18%)	Stopped at first changing cycle
Test 65 (1.13 μm)	+1198	-108	58	20.66	-1.86	337 (30%)	-
Test 76 (1.17 μm)	+2914	-272	56	52.04	-4.86	363 (31%)	Reduced at several points
Test 61 (1.24 μm)	**+189; +849; >1 MΩ**	**-17; -93; - 128**	**116; 116; 8**	**1.63; 7.32; >125,000**	**-0.15; -0.80; -16**	**-**	**Gap after 8 sec on last cycle**

One last observation on table 7.12 is for Test 61 in which three different points are tabulated. Each of the Test 61 points refers to a different cycle for the control signal. Attention should be paid to the absolute incremental of the changes in resistance and current over time as these ratios are significant when nanoconstrictions are to be obtained. If those ratios become too high with respect to the initial values (i.e. 16 in this case); then a nanogap would be formed.

7.8 Summary

This chapter described additional experiments and tests performed to the nanofiber samples. This time the fibers operate at vacuum conditions of 0.1 mbars. The experiment set up, includes the instrumentation and hardware facilities described in previous chapters plus a vacuum chamber available at the Engineering Laboratories from ITESM. Additional experimental results show phenomena such as nanofiber glowing and nanofiber expansion generated also under electrical current control. A re-design of the electrode support system for the new fiber samples intends to reduce the electric resistance of the contacting elements such as the resistance of the nanofiber becomes dominant in the experiments. An analysis of temperature profiles for different tests was developed in order to validate the steady state temperature responses predicted by the Joule heating model from chapter 4. Even though the temperature results have not been entirely validated, the power and temperature profiles for different sample test show a remarkable consistency. The use of a temperature sensing device would give us a much exhaustive validation of the Joule heating model that predicts the temperature of the fiber at the middle point. Finally, tables summarizing the control program characteristic parameters, results for the experiment under vacuum conditions, and results for experimental repeatability are also shown.

Chapter 8

Conclusions

This research provides to provide a deep characterization and analysis of glassy carbon fiber samples (diameters from a little less than 1μm to 4 μm) when they are subject to electric fields and currents. The general objective was to increase our knowledge in the prediction of phenomena associated to their performance under free air and vacuum conditions subject to controlled electrical experiments. The prediction of nanoconstraints, nanoconstraint progressions, nanogap formation, electroluminescence (glowing) and fiber expansion are studied under controlled electrical experimentation using a data acquisition system and a driving LabVIEW software program. Also, modeling the temperature of the fiber sample is performed using a Joule heating mathematical model, represented by a second order partial differential equation (PDE) where the temperature field is analyzed in detail. Even though, a temperature measurement of the fiber sample would be necessary to completely validate the Joule heating model. Temperature ranges for free air and vacuum conditions are estimated based upon this model.

This dissertation accomplished the following sequence of steps to provide a solid methodology:

1. Glassy carbon nanofiber samples were manufactured using techniques and procedures developed for photolithography and for electrospinning processes. They were fabricated using the advanced clean room facilities of UCI. Diameters in glassy carbon fiber samples range from 0.800 μm to 4.5 μm.
2. Nanofiber sample structures were identified and observed using SEM microscope to perform a geometric characterization of the sample.
3. Electromigration phenomena, carbon material and applications of nanofibers were studied carefully and some state of the art developments were consulted.

4. Temperature changes and melting phenomenon was modeled using a second order PDE considering heat conduction, heat generated by current flowing and temperature gradient effects along the longitudinal axis of the fiber.
5. Nanofiber breackdowns, which consists of nanoconstrictions and nanogaps, were induced in nanostructure samples by controlling the voltage and electrical current through the carbon fiber under free air conditions. Data gathering processing was design and performed to measure power dissipation and conductivity.
6. Experiments operating under vacuum conditions were also developed to induce nanoconstriction, nanogaps and nanoglowing in the samples. Electrical variables such as voltage and current were controlled under LabVIEW software graphic programming. The vacuum experiments also measured power dissipation and conductivity.
7. After testing, sample observation was performed again using the SEM to identify nanofiber breackdown phenomena such as nanoconstriction, and nanogap formation.

The previous sequence of steps is summarized as follows.

Three processes for fiber sample fabrication were discussed:

a. Support electrode development using photolithography
b. Electrospinning methods which include FFE and NFE as the basis for the nanofiber sample fabrication in this research project.
c. Pyrolysis process to consolidate the finished fiber.

The EM phenomena and Joule heating was analyzed for nanowires and nanofibers, even though the glassy carbon nanofibers are immune to EM. Nevertheless, concepts in metal EM are adequate for their analysis in very thin glassy carbon nanoconstrictions. The Joule heating phenomena is used to predict the formation of nanogaps and nanoconstrictions in glassy carbon fibers. The current control through the fiber is required to obtain satisfactory results over nanofiber samples.

The process by which polymers are converted into amorphous carbon was also reviewed. A brief discussion on C-MEMS processes was also introduced to generate microstructures useful

for these work objectives. Finally, possible nanofiber applications were described. One of such application (tissue engineering) described a side research work that the author of this manuscript had the opportunity to complete. Such work included the study of stem cell orientation along PCL aligned nanofibers.

The Joule heat conduction model of the nanofiber was described in order to predict fiber´s temperature profiles subject to controlled currents. The mathematical model includes the heat conduction, heat capacity and the heat stimulation terms which are part of a second order PDE equation having the nanofiber internal temperature as the state variable. The transient and steady state solutions are described and used to perform some elementary simulation exercises using platinum and glassy carbon fibers. The mathematical model presented was used to predict nanofiber´s temperature profiles in the generation of nanoconstrictions and nanogaps.

To perform data acquisition, control and post-processing routines in the experimentation with the glassy carbon nanofibers, a hardware platform from National Instruments MyDAQ was used having LabVIEW as the programming language. The software program included a set of routines that perform the control and pre-processing of data using graphical programming. The post-processing included an IIR digital filter that removes noise and performs a smoothing action to the measured signal.

Experiments and tests were performed to the nanofiber samples operating in free air. The experiment set up, instrumentation and hardware facilities available at ITESM, Monterrey campus. One fundamental outcome is the ability to control nanoconstriction progression over a nanofiber using electrical current control.

Additional experiments and tests were performed to the nanofiber samples under vacuum conditions of 0.1 mbars. Experimental results show phenomena such as nanofiber glowing (electroluminescence) and nanofiber expansion generated also under electrical current control. A re-design of the electrode support system for the new fiber samples intends to reduce the electric resistance of the contacting elements, such that the resistance of the nanofiber becomes dominant in the experiments. An analysis of temperature profiles for different tests was developed in order to validate the steady state temperature responses predicted by the Joule heating model. Even though the temperature results have not been entirely validated with a direct/indirect temperature

measurement during an experiment, the power and temperature profiles for different sample test show a remarkable consistency.

The following research lines can be followed taking the present work as a starting platform:

1. To measure the actual temperature of the nanofiber in order to adjust and validate the Joule heating model. A layer of poly-methyl methacrylate (PMMA) or some other polymer with a known melting point can be spin coated on a sample. The melting point for PMMA is 160 ^{o}C; therefore PMMA can be melted by running an electrical current through a nanofiber increasing its temperature to the melting point of PMMA. Optical confirmation of PMMA melting can then be obtained. This experiment could provide evidence that the models used properly predict the temperature reached by the nanofiber.
2. To modify the nanofiber operating environment such that a different gas is used instead of air or vacuum.
3. To experiment the electroluminescence phenomenon with additional samples in order to establish conditions a viability of the fibers as a micro-light source.
4. To develop gas sensors where the fiber would have the heating function.
5. To experiment on the generation of narrower gaps below 100 nm.
6. To perform experiments with electrical stimulation of stem cells stimulation using both, the carbon electrodes and the glassy carbon nano-fiber scaffolds.

Appendices

A. Glossary

SEM: Scanning Electron Microscope

SETT: Single Electron Tunneling Transistors

C-MEMS: Carbon Micro Electro-Mechanical Systems

FFE: Far Field Electrospinning

NFE: Near Field Electrospinning

EM: Electromigration

e-beam: Electron Beam Lithography

UDEM: Universidad de Monterrey

ITESM: Instituto Tecnológico y de Estudios Superiores de Monterrey

UCI: University of California at Irvine

SETD: Single Electron Tunneling Device

MSC: Mesenchymal Stem Cells

PCL: Poly-caprolactone

PDE: Partial Differential Equation

R: Electrical Resistance

R_L: Nanofiber Resistance

R_f: Nanofiber Resistance

I: Electrical Current

I_f: Nanofiber Current

V: Voltage

V0, V1: Voltages to measure electrical current throughout the nanofiber

R_s: Series Resistance

ΔT: Temperature Difference

T_o: Ambient Temperatire

T_m: Melting Point

k: Thermal Conductivity

ρ: Resistivity

σ: Conductivity

P: Power

f: Correction factor

B. LABVIEW Code of Control Program

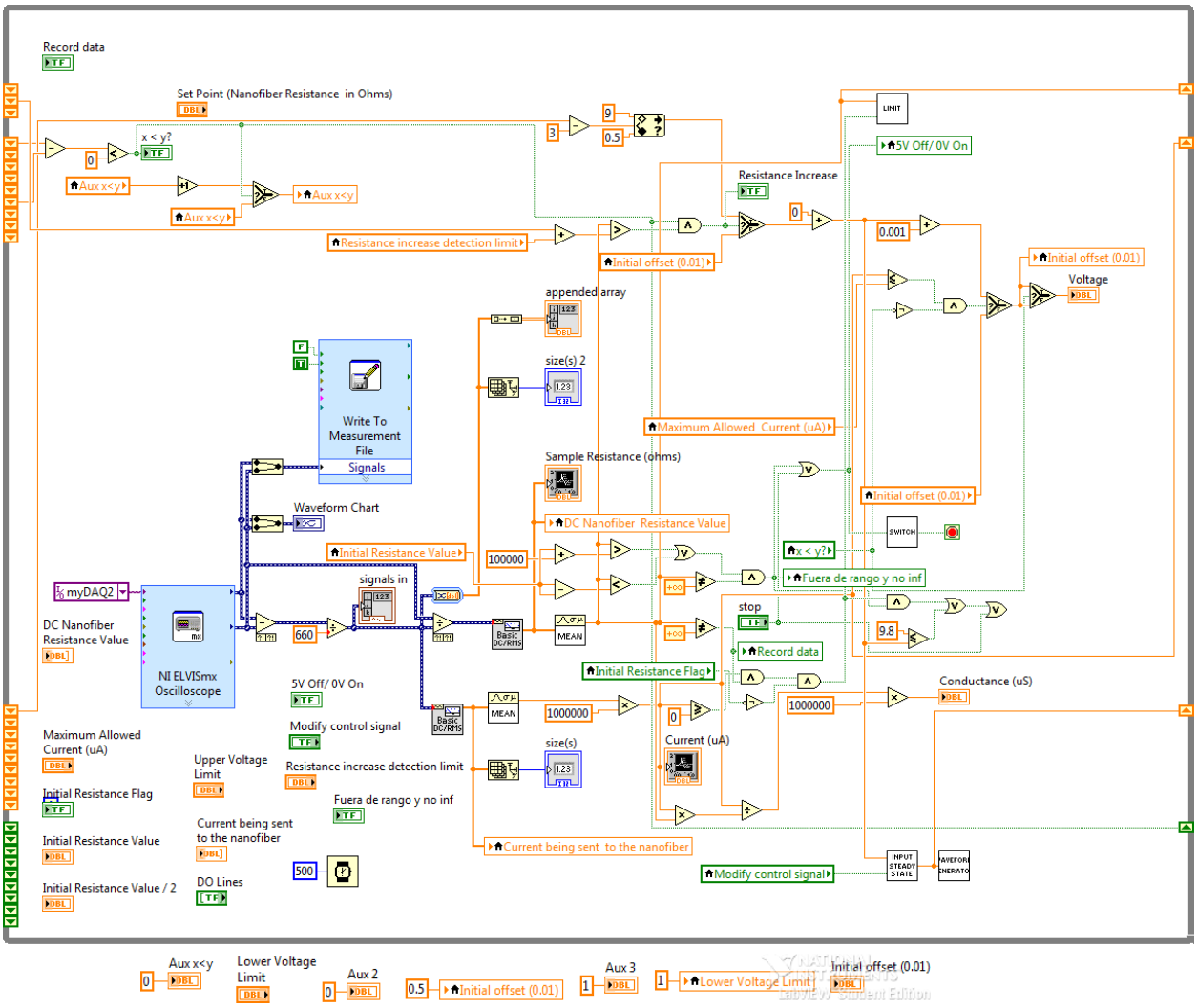

C. Matlab Code

The following MATLAB code was used to perform processing and post processing analysis over the nanofiber data.

```
clc
clear all
close all

A=1.16937E-12;
L=7.9860E-05;

    load
C:\Users\Christian\Desktop\Thesis\sample3_gpo1\test60_comercialresistor\resis
tencia_110.mat
    load
C:\Users\Christian\Desktop\Thesis\sample3_gpo1\test60_comercialresistor\corri
ente_110.mat
    load
C:\Users\Christian\Desktop\Thesis\sample3_gpo1\test60_comercialresistor\condu
ctance_110.mat
    load
C:\Users\Christian\Desktop\Thesis\sample3_gpo1\test60_comercialresistor\volta
ge0_110.mat
    load
C:\Users\Christian\Desktop\Thesis\sample3_gpo1\test60_comercialresistor\volta
ge1_110.mat

filename='C:\Users\Christian\Desktop\Thesis\sample3_gpo1\test60_comercialresi
stor\'

    tiempo=(1:1:length(V0));
    tiempo2=(tiempo.*100e-6)*4.95;

    b=figure
    plot(tiempo2,R)
    grid on
    title('R from the load')
    xlabel('Time (sec)')
    ylabel('Resistance (ohms)')
    axis([0 +Inf 0 15000])
    name=strcat(filename, 'R1')
    saveas(b,name,'jpg')
    close

    yR=resistance();
    b3=figure
    plot(tiempo2,yR)
    grid on
    title('Resistance After IIR Filter')
    xlabel('Time (sec)')
```

```
ylabel('Resistance (Ohms)')
axis([0 +Inf 0 15000])
name=strcat(filename, 'R1_IIR_filter')
saveas(b3,name,'jpg')

c=figure
plot(tiempo2,I)
grid on
title('Current flowing into load')
xlabel('Time (sec)')
ylabel('Current (A)')
axis([0 +Inf 0 +Inf])
name=strcat(filename, 'I1')
saveas(c,name,'jpg')
close
clear name

yI=current();
b3=figure
plot(tiempo2,yI)
grid on
title('Current flowing into load, after IIR filter')
xlabel('Time (sec)')
ylabel('Current (A)')
axis([0 +Inf 0 +Inf])
name=strcat(filename, 'I1_IIR_filter_wc')
saveas(b3,name,'jpg')
close

d=figure
plot(tiempo2,C)
grid on
title('Conductance')
xlabel('Time (sec)')
ylabel('Conductance (S)')
axis([0 +Inf 0 +Inf])
name=strcat(filename, 'C1')
saveas(d,name,'jpg')
close
clear name

yC=conductance();
b3=figure
plot(tiempo2,yC)
grid on
title('Conductance, after IIR filter')
xlabel('Time (sec)')
ylabel('Conductance (S)')
axis([0 +Inf 0 +Inf])
name=strcat(filename, 'C1_IIR_filter_wc')
saveas(b3,name,'jpg')
close

f=figure
P=V1.*I;
plot(tiempo2,P)
```

```
grid on
title('Power')
xlabel('Time (sec)')
ylabel('Power (W)')
axis([0 +Inf 0 +Inf])
name=strcat(filename, 'P1')
saveas(f,name,'jpg')
close
clear name

yP=power();
b3=figure
plot(tiempo2,yP)
grid on
title('Dissipated Power (W), after IIR filter')
xlabel('Time (sec)')
ylabel('Power (W)')
axis([0 +Inf 0 +Inf])
name=strcat(filename, 'P1_IIR_filter_wc')
saveas(b3,name,'jpg')
close

name=strcat(filename, 'yP_110')
save(name, 'yP')

a=figure
subplot(2,2,1), plot(tiempo2,V0)
grid on
title('Voltage from DAQ')
xlabel('Time (sec)')
ylabel('Voltage (V)')
axis([0 +Inf 0 +Inf])

subplot(2,2,2), plot(tiempo2,yR)
grid on
title('R from the load')
xlabel('Time (sec)')
ylabel('Resistance (ohms)')
axis([-Inf +Inf 0 15000])

subplot(2,2,3), plot(tiempo2,yI)
grid on
title('Current flowing into load')
xlabel('Time (sec)')
ylabel('Current (A)')
axis([0 +Inf 0 +Inf])

subplot(2,2,4), plot(tiempo2,yP)
grid on
title('Power')
xlabel('Time (sec)')
ylabel('Power (W)')
axis([0 +Inf 0 +Inf])

name=strcat(filename, '110_IIR')
```

```
saveas(a,name,'jpg')

name=strcat(filename, 'yC_110')
save(name, 'yC')

name=strcat(filename, 'yI_110')
save(name, 'yI')

name=strcat(filename, 'yR_110')
save(name, 'yR')

rho=(A/L).*yR;
name=strcat(filename, 'resistivity_110')
save(name, 'rho')

sigma=1./rho;
name=strcat(filename, 'conductivity_110')
save(name, 'sigma')

Acm=A*10000;
J=yI/Acm;
name=strcat(filename, 'Current_density_110')
save(name, 'J')

a=figure
plot(tiempo2,J)
grid on
title('Current Density (A/cm2)')
xlabel('Time (sec)')
ylabel('J (A/cm^2)')
axis([-Inf Inf 0 3.5e4])
name=strcat(filename, 'Current_density')
saveas(a,name,'jpg')
close

a=figure
plot(yI,rho)
grid on
title('Resistivity vs Current')
xlabel('Current (A)')
ylabel('Resistivity (Ohm.m)')
name=strcat(filename, 'rho_vs_yI')
saveas(a,name,'jpg')
close

a=figure
plot(yI,yR)
grid on
title('Resistance vs Current')
xlabel('Current (A)')
ylabel('Resistance (Ohms)')
name=strcat(filename, 'RL_vs_yI')
saveas(a,name,'jpg')
close
```

```
a=figure
plot(V1, yI)
grid on
title('I vs V')
xlabel('Voltage (V)')
ylabel('Current (A)')
name=strcat(filename, 'yI_vs_V1')
saveas(a,name,'jpg')
close

f=1.4051;
aux2=rho./(8*6.3);
aux3=(yI.*L*f/A).^2;

Tc=aux2.*aux3+292.15;
a=figure
plot(tiempo2,Tc)
grid on
title('Temperature at the midpoint of the fiber in Kelvin')
xlabel('Time (sec)')
ylabel('Temperature ({\circ}K)')
axis([0 +Inf 0 4000])
name=strcat(filename, 'Tc_110')
saveas(a,name,'jpg')

Tc2=Tc-272.15;
a=figure
plot(tiempo2,Tc2)
grid on
title('Temperature at the midpoint of the fiber in Celsius')
xlabel('Time (sec)')
ylabel('Temperature ({\circ}C)')
axis([0 +Inf 0 4000])
name=strcat(filename, 'Tc2_110')
saveas(a,name,'jpg')
```

D. Additional Test Results

Additional test results for Test 64, Test 65, Test 66, Test 75, Test 76, and Test 77 are shown in this appendix. First Test 64, Test 65, and Test 66 had the objective of reproducing the emission of light, avoid breaking of the fibers, and also determine if the fibers tend to bend after those experiments. Then Test 75, and Test 76 assess reproducibility of results shown in section 7.7 of this manuscript.

Characteristic dimensional and electrical values for Test 64 are summarized in table 7.4 of this manuscript. Test 64 was run under vacuum conditions (0.1 mbar and 25 ^{o}C). Constant voltage increments of 0.5 V were used as the control signal. Voltage was left in the on state for 120 seconds and in the off state for 40 seconds. This sample nanofiber emitted light (incandescence). The nanofiber did not break in accordance with the objectives for this experiment. This particular nanofiber became completely straight at the end of the experiment as shown in figure D1 and D2. The electrical signals for Test 64 are shown in figure D3. The temperature profile for this experiment is shown in figure D4.

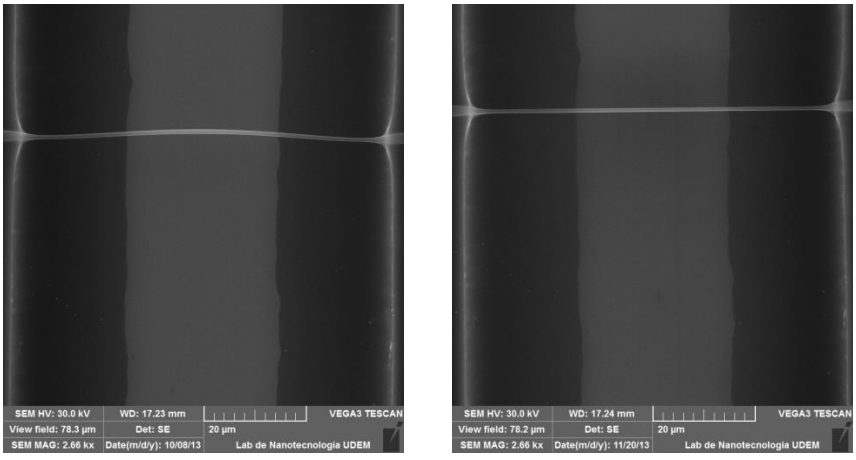

a) **b)**

Figure D1: Top view for Test 64 a) before and b) after

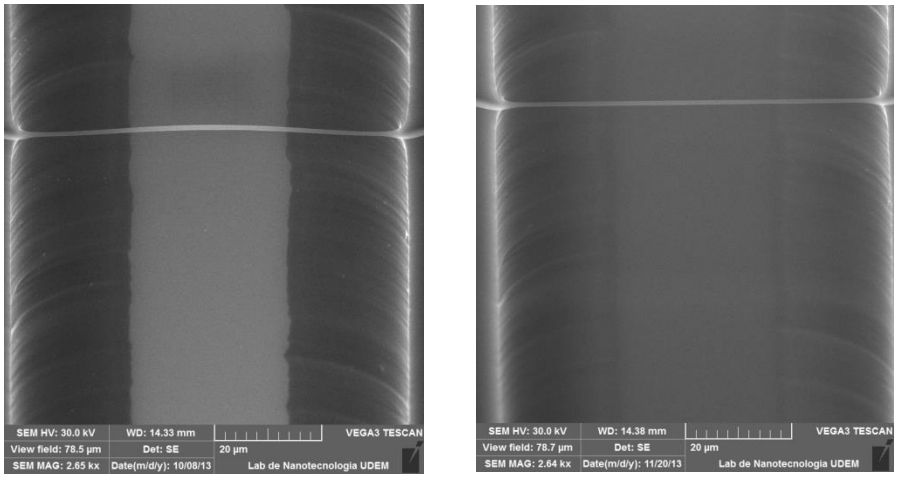

a) **b)**

Figure D2: Tilted view of 60 ^{o} for Test 64 a) before and b) after

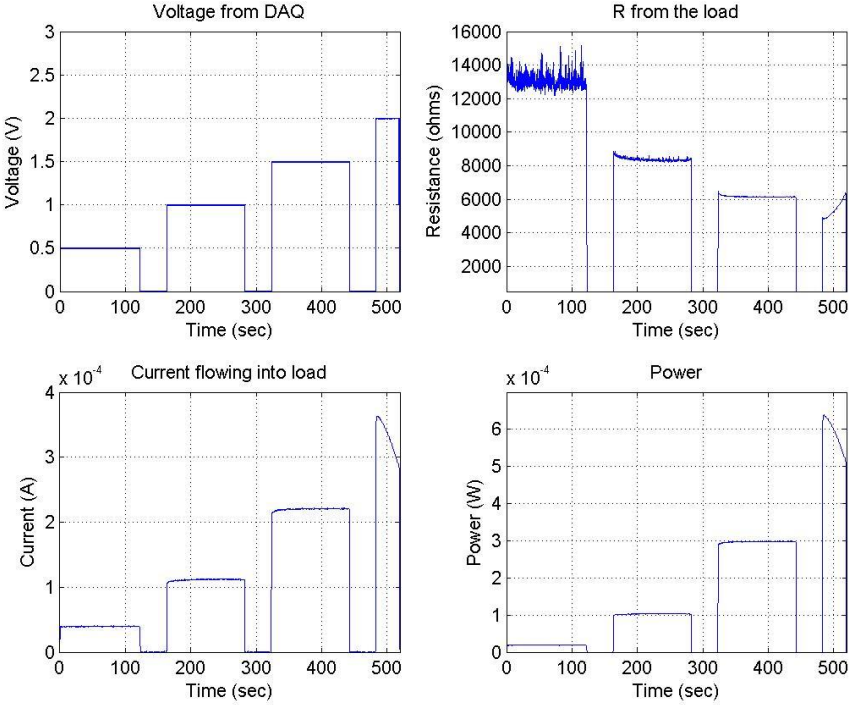

Figure D3: Electrical signals for Test 64

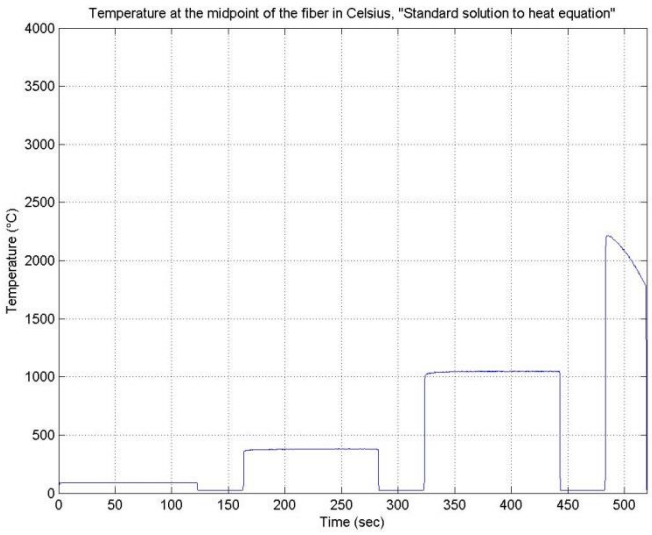

Figure D4: Temperature profile for Test 64

Characteristic dimensional and electrical values for Test 65 are summarized in table 7.4 of this manuscript. Test 65 was run under vacuum conditions (0.1 mbar and 25 ^{o}C). Constant voltage increments of 0.5 V were used as the control signal. Voltage was left in the on state for 120 seconds and in the off state for 40 seconds. This sample nanofiber emitted light (incandescence). The nanofiber did not break in accordance with the objectives for this experiment. This particular nanofiber became completely straight at the end of the experiment as shown in figure D5 and D6. The electrical signals for Test 65 are shown in figure D7. The temperature profile for this experiment is shown in figure D8.

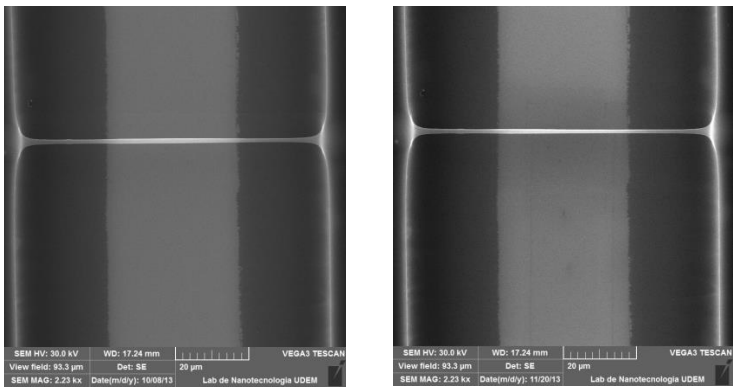

a) **b)**

Figure D5: Top view for Test 65 a) before and b) after

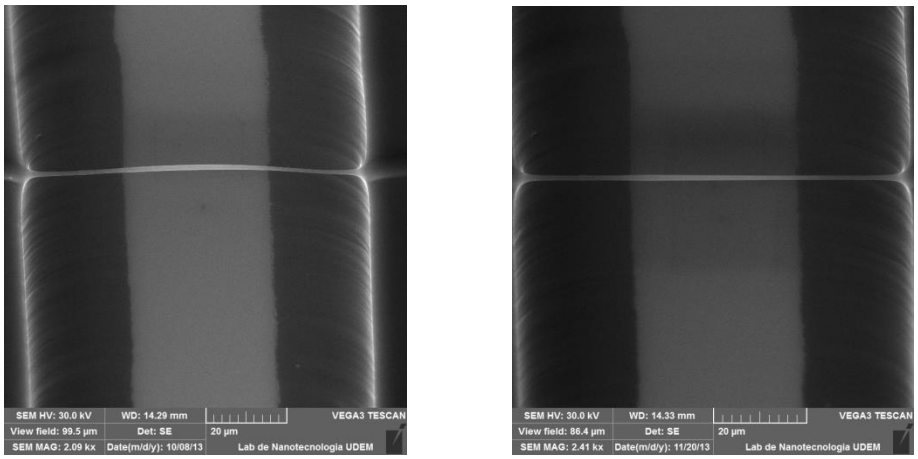

a) **b)**

Figure D6: Tilted view of 60 ^{o} for Test 65 a) before and b) after

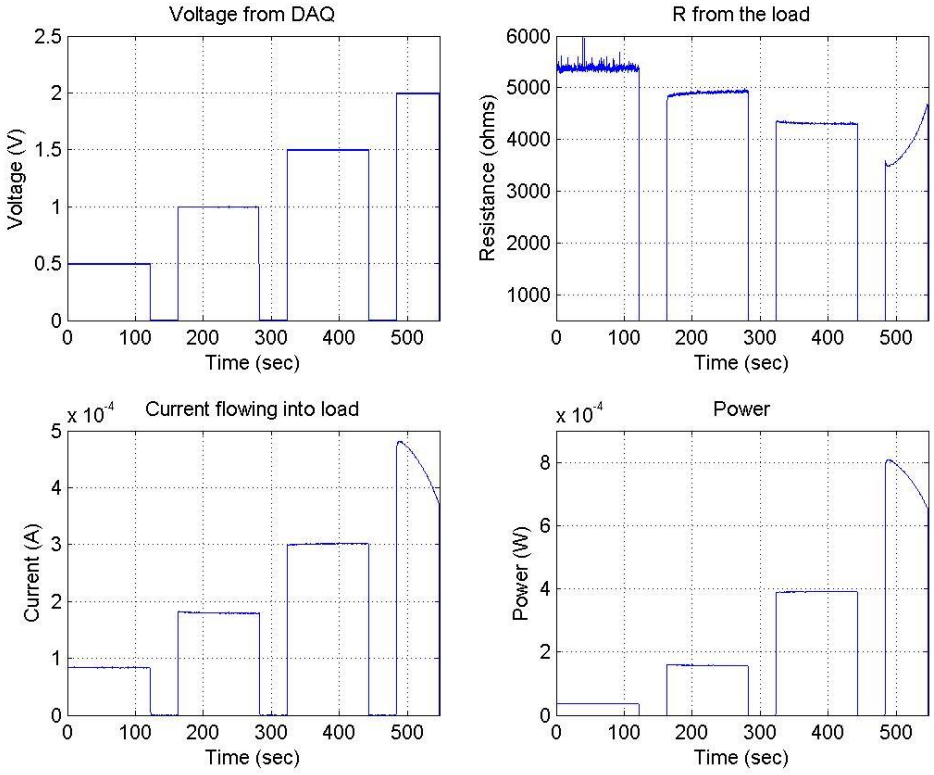

Figure D7: Electrical signals for Test 65

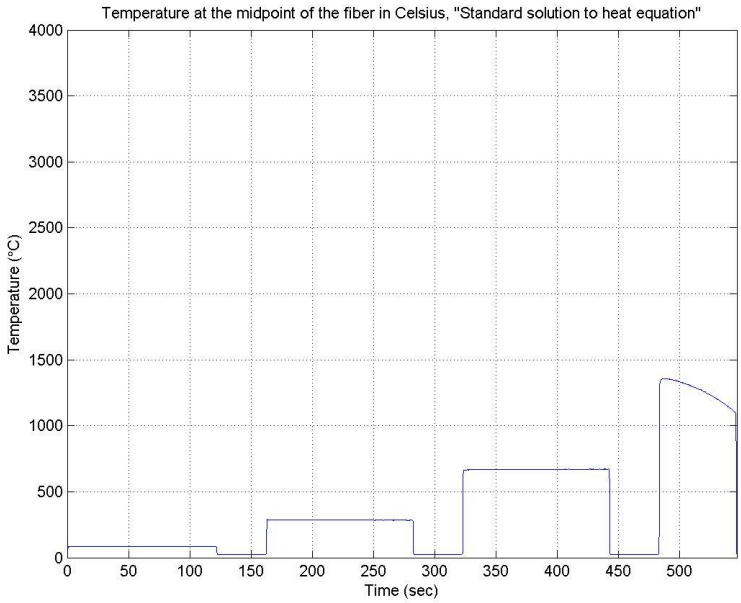

Figure D8: Temperature profile for Test 65

Characteristic dimensional and electrical values for Test 66 are summarized in table 7.4 of this manuscript. Test 66 was run under vacuum conditions (0.1 mbar and 25 ^{o}C). Constant voltage increments of 0.5 V were used as the control signal. Voltage was left in the on state for 120 seconds and in the off state for 40 seconds. This sample nanofiber emitted light (incandescence). The nanofiber did not break in accordance with the objectives for this experiment. This particular nanofiber only reduced in its diameter as shown in figure D9 and D10. The electrical signals for Test 66 are shown in figure D11. The temperature profile for this experiment is shown in figure D12.

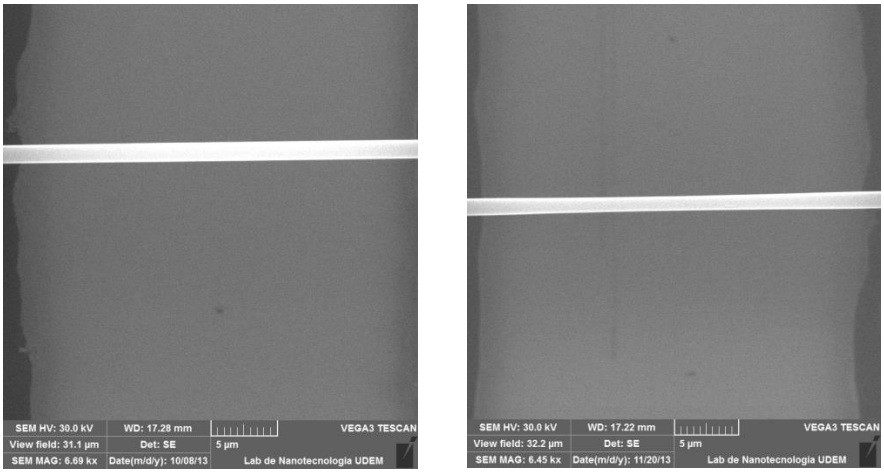

a) **b)**

Figure D9: Top view for Test 66 a) before and b) after

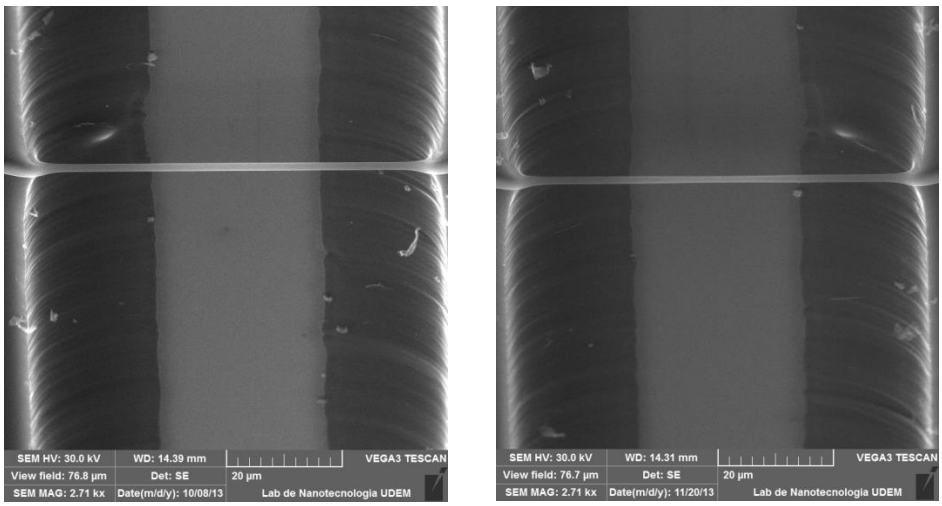

a) **b)**

Figure D10: Tilted view of 60 ^{o} for Test 66 a) before and b) after

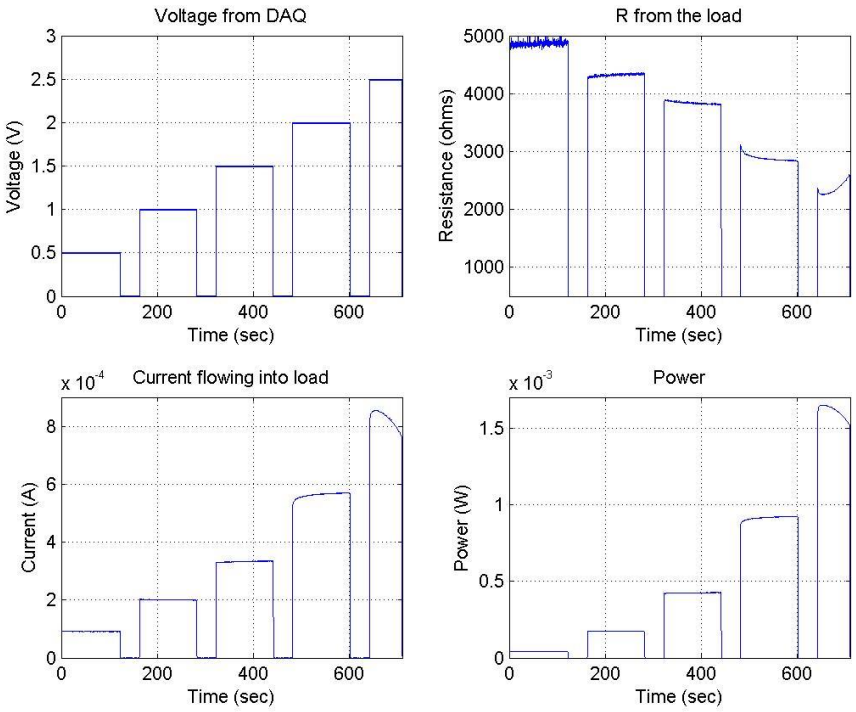

Figure D11: Electrical signals for Test 66

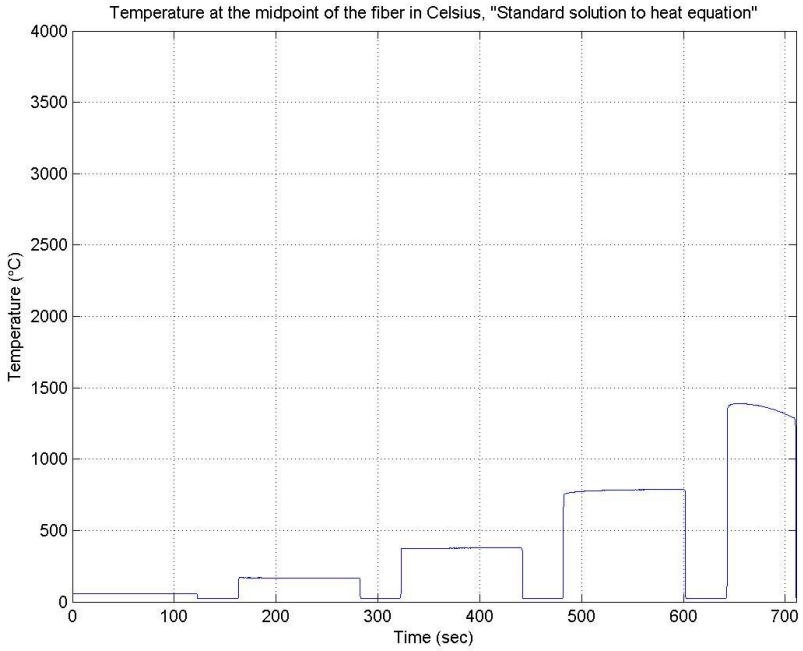

Figure D12: Temperature profile for Test 66

Characteristic dimensional and electrical values for Test 75 are summarized in table 7.11 of this manuscript. Test 75 was run under vacuum conditions (0.1 mbar and 25 ^{o}C). Constant voltage increments of 0.5 V were used as the control signal. Voltage was left in the on state for 120 seconds and in the off state for 40 seconds. This sample nanofiber emitted light (incandescence). The nanofiber did not break in accordance with the objectives for this experiment. This particular nanofiber only reduced in its diameter as shown in figure D13 and D14. The electrical signals for Test 75 are shown in figure D15. The temperature profile for this experiment is shown in figure D16.

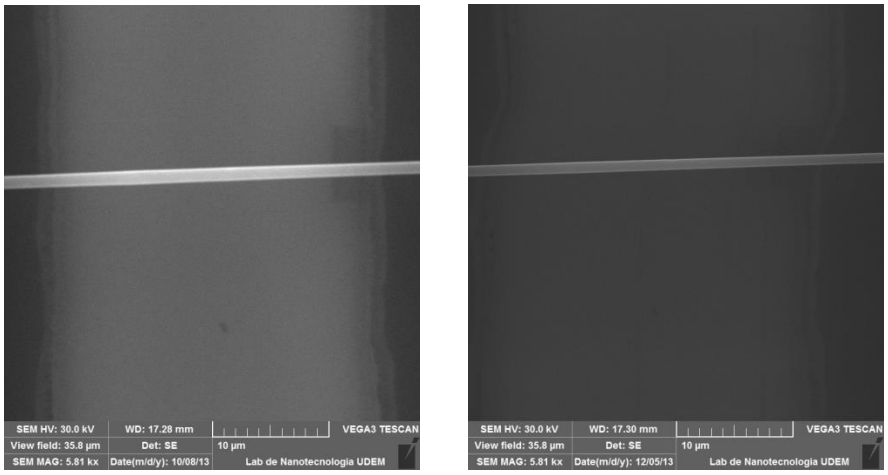

a) **b)**

Figure D13: Top view for Test 75 a) before and b) after

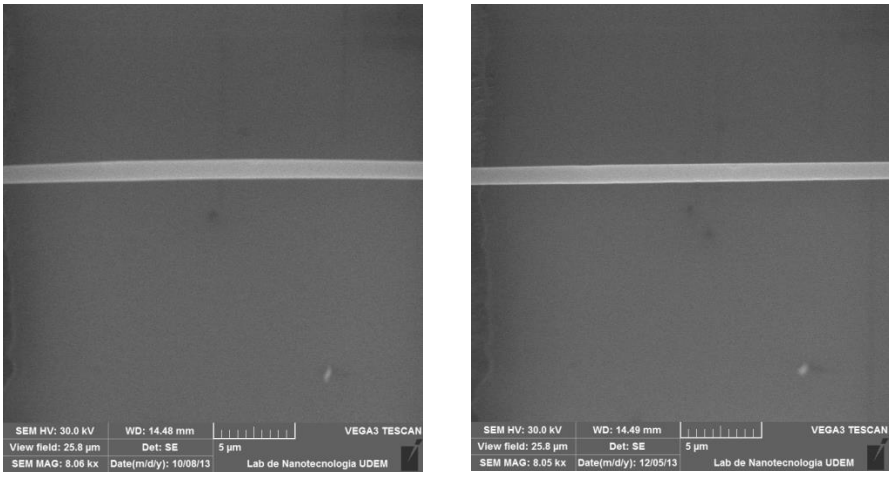

a) **b)**

Figure D14: Tilted view of 60 ^{o} for Test 75 a) before and b) after

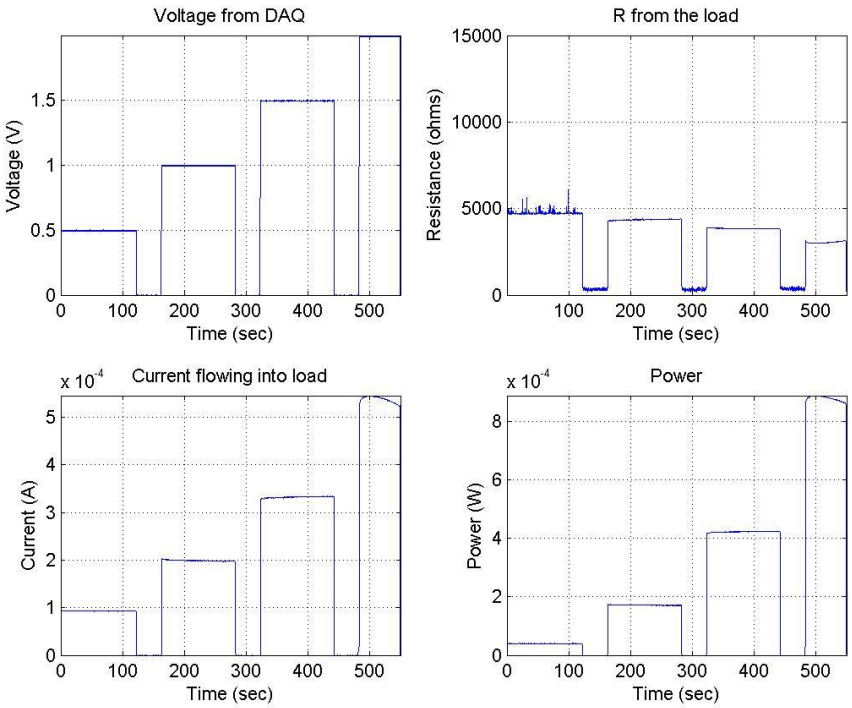

Figure D15: Electrical signals for Test 75

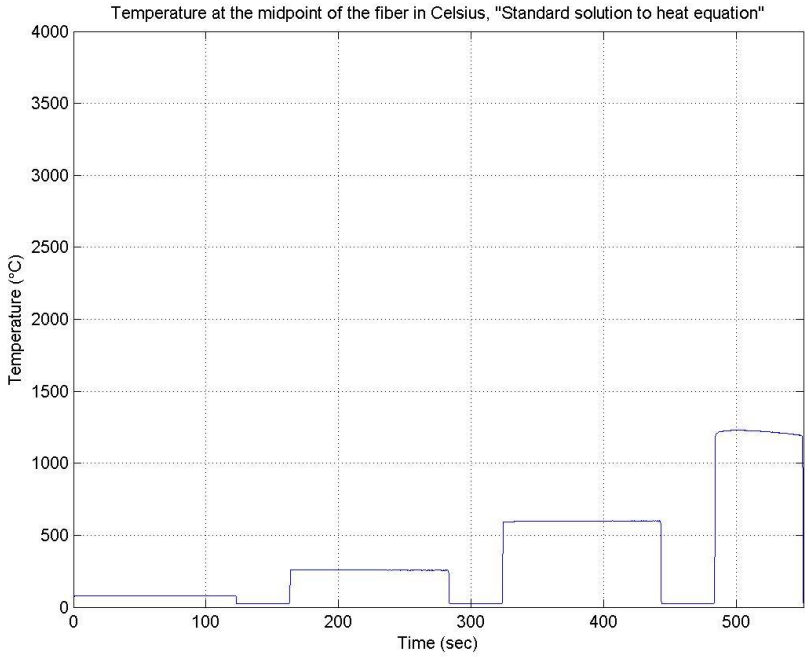

Figure D16: Temperature profile for Test 75

Characteristic dimensional and electrical values for Test 76 are summarized in table 7.11 of this manuscript. Test 76 was run under vacuum conditions (0.1 mbar and 25 ^{o}C). Constant voltage increments of 0.5 V were used as the control signal. Voltage was left in the on state for 120 seconds and in the off state for 40 seconds. This sample nanofiber emitted light (incandescence). The nanofiber did not break in accordance with the objectives for this experiment. This particular nanofiber reduced in its diameter in several parts of the nanofiber as shown in figure D17 and D18. Sections of the underlying carbon may be making electrical contact between the middle portion and the extremes of the suspended nanofiber. The electrical signals for Test 76 are shown in figure D19. The temperature profile for this experiment is shown in figure D20.

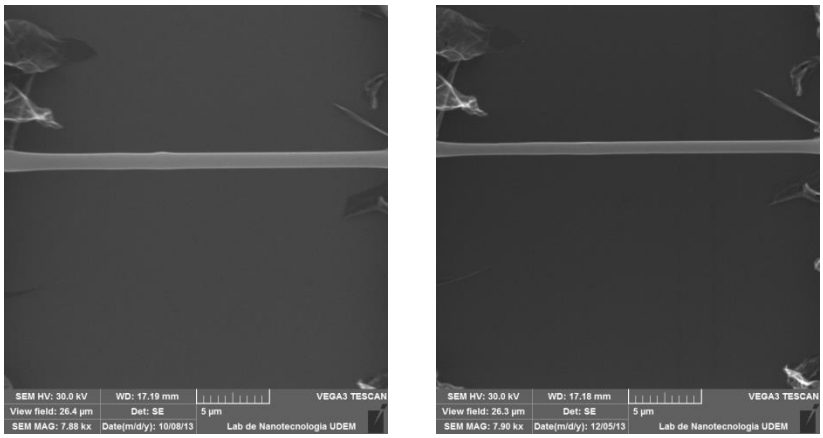

a) **b)**

Figure D17: Top view for Test 76 a) before and b) after

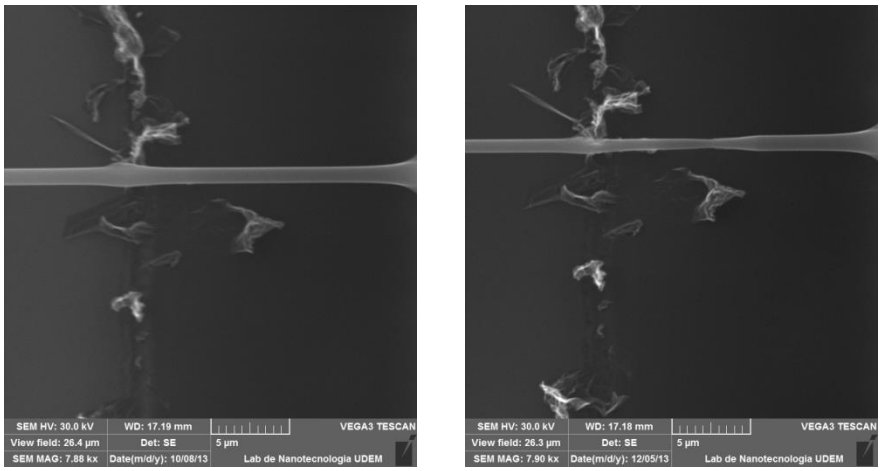

a) **b)**

Figure D18: Top view for Test 76 right side a) before and b) after

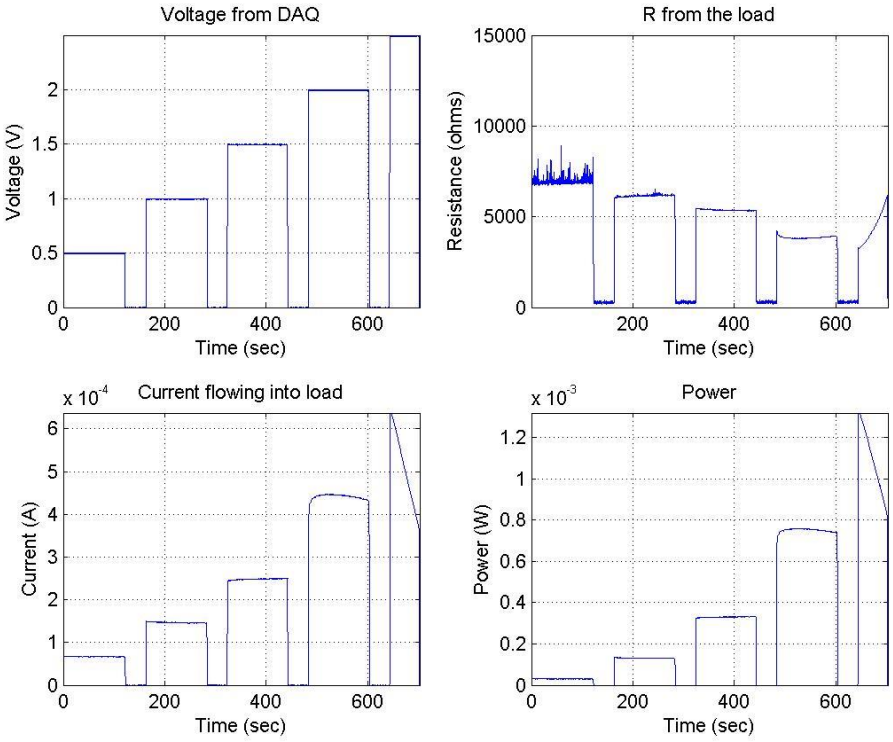

Figure D19: Electrical signals for Test 76

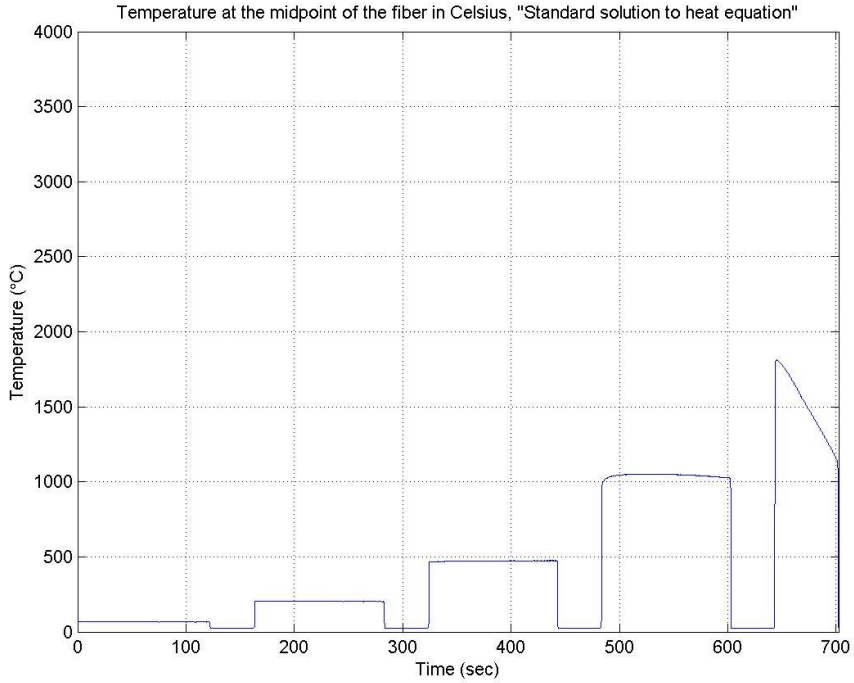

Figure D20: Temperature profile for Test 76

E. Derivation for Heat Equation with Joule Heat in Steady and Transient State

This appendix develops a mathematical derivation for both, steady state and transient state heat equation. First we start from the heat equation in its homogeneous form:

$$k\frac{\partial^2 u}{\partial x^2} = \frac{\partial u}{\partial t} \tag{E.1}$$

E.1 has the following initial conditions:

$$u(0,t) = 0 \tag{E.2}$$
$$u(x,0) = f(x) \tag{E.3}$$
$$u(L,t) = 0 \tag{E.4}$$

First, it is proposed a solution of the form:

$$u = X(x)T(t) \tag{E.5}$$

Having the following boundary conditions:

$$\frac{\partial^2 u}{\partial x^2} = X''(x)T(t) \tag{E.6}$$
$$\frac{\partial u}{\partial t} = X(x)T'(t) \tag{E.7}$$

` Substituting E.6 and E.7 in E.1:

$$k\,X''(x)T(t) = X(x)T'(t) \tag{E.6}$$

Using separation of variables method we can obtain:

$$\frac{X''(x)}{X(x)} = \frac{T'(x)}{k\,T(t)} = -\lambda^2 \tag{E.7}$$

From equation E.7 we can obtain two different equations, namely E.8 and E.9:

$$X''(x) + \lambda^2 X(x) = 0 \tag{E.8}$$

$$T'(t) + k\lambda^2 T(t) = 0 \tag{E.9}$$

Equations E.8 and E.9 have the following solutions:

$$X = C_1 Cos\lambda x + C_2 Sin\lambda x \tag{E.10}$$

$$T = C_3 e^{-k\lambda^2 t} \tag{E.11}$$

Now, applying initial conditions E.2 on E.10 and applying a superposition approach on the first term from E.10 we can obtain that C1=0. Following the same line with the second term from E.10, we note that:

$$X(L) = C_2 Sin\lambda L = 0 \tag{E.12}$$

Equation E.12 can only be equal to 0 when the argument of the sine function is equal to nπ, therefore E.10 and E.11 become:

$$X = C_2 Sin\frac{n\pi}{L}x \tag{E.13}$$

$$T = C_3 e^{-k\left(\frac{n\pi}{L}\right)^2 t} \tag{E.14}$$

Recalling the proposed solution in E.5, and substituting E.13 and E.14 we obtain:

$$U_n = A_n\, e^{-k\left(\frac{n\pi}{L}\right)^2 t}\, Sin\frac{n\pi}{L}x \tag{E.15}$$

Where $A_n = C_2 C_3$. Equation E.15 is valid for all values of n.

So far we have satisfied initial condition E.2, now we are ready to find a solution to satisfy E.3. Rewriting E.15 to formally express its validity for all values of n we obtain:

$$U(x,0) = f(x) = \sum_{n=1}^{\infty} A_n \, e^{-k\left(\frac{n\pi}{L}\right)^2 t} \, Sin\frac{n\pi}{L}x \tag{E.15}$$

Using initial condition E.3 on E.15 (t=0) we obtain:

$$U(x,0) = f(x) = \sum_{n=1}^{\infty} A_n \, Sin\frac{n\pi}{L}x \tag{E.16}$$

E.16 is recognized as a midrange series of f in sine series, which results in E.17:

$$A_n = \frac{2}{L}\int_0^L f(x) \; Sin\frac{n\pi}{L}x \, dx \tag{E.17}$$

By substituting E. 17 into E.16 we obtain:

$$u(x,t) = \frac{2}{L}\sum_{n=1}^{\infty} \int_0^L f(x) \, Sin\frac{n\pi}{L}x \, dx \, e^{-k\left(\frac{n\pi}{L}\right)^2 t} \, Sin\frac{n\pi}{L} \tag{E.18}$$

Equation E.18 is the transient temperature response for the homogeneous case as shown in E.1. We now want to explore the solution for the non-homogeneous case in which the heat equation now takes into account the heat generated by the current flow through the nanofiber.

$$k\frac{\partial^2 u}{\partial x^2} + r = \frac{\partial u}{\partial t} \tag{E.19}$$

E.19 has the following initial conditions:

$$u(0,t) = u_o \tag{E.20}$$

$$u(L,t) = u_1 \tag{E.21}$$

$$u(x,0) = f(x) \tag{E.22}$$

Where u_o and u_1 represent T_o and f(x) represents T.

Let us now propose E.23 as a possible solution for E.19:

$$u(x,t) = v(x,t) + Y(x) \tag{E.23}$$

Taking the second derivative of E.23 we obtain:

$$\frac{\partial^2 u}{\partial x^2} = \frac{\partial v}{\partial x^2} + Y''(x) \tag{E.24}$$

And using $\frac{\partial u}{\partial t} = \frac{\partial v}{\partial t}$ into E. 24 to substitute the result in E.19 we obtain:

$$k\frac{\partial v}{\partial x^2} + kY''(x) + r = \frac{\partial v}{\partial t} \tag{E.25}$$

From E.25 we recognize that we need the second and third term on the left side to be equal to zero in order for us to use the previously derived results for the homogeneous case, in other words:

$$kY''(x) + r = 0 \tag{E.26}$$

Rearranging E.26 for $Y''(x)$ and integrating two times with respect to x we obtain:

$$Y = -\frac{r}{2k}x^2 + C_1 x + C_2 \tag{E.27}$$

Using E.23 and E.20 (x=0) we obtain that $Y(0)=u_o$, in other words C_2 in equation E.27 is equal to zero ($C_2=0$). Following the same idea, using E.23 and E.21 we obtain that $Y(L)=u_1$. Therefore, evaluating E.27 in L, using the fact that $C_2=0$ and solving for C_1 we obtain:

$$C_1 = \frac{1}{L}(u_1 - u_0) + \frac{r}{2k} \tag{E.28}$$

Substituting E.28 in E.27 we obtain:

$$Y(x) = -\frac{r}{2k}x^2 + \left[\frac{1}{L}(u_1 - u_0) + \frac{rL}{2k}\right]x + u_0 \qquad \text{(E.29)}$$

Recalling that $u_1=u_o=T_o$, recognizing that $r = \frac{q}{\rho c}$ and rearranging, we obtain:

$$Y(x) = \frac{q}{2K}(Lx - x^2) + T_o \qquad \text{(E.30)}$$

Where $= \frac{K}{\rho c}$. Equation E.30 is the same steady state solution as for equation 4.2 in this dissertation.

Let us now consider E.23 one more time, but now rearranging $v(x,t)$ and evaluating for t=0 using E.22:

$$v(x,0) = f(x) - Y(x) \qquad \text{(E.31)}$$

$v(x,t)$ is the solution to the heat equation in its homogenous case, therefore we can rewrite E.18 now substituting f(x) from E.18 with $v(x,0)$ from E.31:

$$u(x,t) = \frac{2}{L}\sum_{n=1}^{\infty}\int_0^L \big(f(x) - Y(x)\big)\, Sin\frac{n\pi}{L}x\, dx\, e^{-k\left(\frac{n\pi}{L}\right)^2 t}\, Sin\frac{n\pi}{L} \qquad \text{(E.32)}$$

Using the fact that $f(x)=T_o$, and the E.30 into E.32 we obtain an integral expression that needs to be solved:

$$\int_0^L \big(f(x) - Y(x)\big)\, Sin\frac{n\pi}{L}x\, dx = \frac{q}{kL}\int_0^L (x^2 - Lx) Sin\frac{n\pi}{L}x\, dx \qquad \text{(E.33)}$$

Solving this integral and substituting into E.32 provides the solution to this transient state temperature equation for the non-homogeneous case (Joule heat included):

$$T_2 = \frac{2qL^2}{k\pi^3}\sum_{m=1}^{\infty}\frac{(-1)^m-1}{m^3}\ e^{-k\left(\frac{m\pi}{L}\right)^2 t}\ Sin\frac{m\pi}{L}x \qquad \text{(E.34)}$$

Equation E.34 is the same as equation 4.3 in this dissertation.

References

[1] Deng-Guang, Y., Xiao-Fei, Z., Xia-Xia, S., Li-Min, Z., Branford-White, C., Yang, Y. C., et al. (2009, 11-13 June 2009). Polyacrylonitrile/Kaolinite Hybrid Nanofiber Mats Aimed for Treatment of Polluted Water. Paper presented at the Bioinformatics and Biomedical Engineering , 2009. ICBBE 2009. 3rd International Conference on.

[2] Dresselhaus, M. S., & Dresselhaus, G. (1997a). Energy-Related Applications of Nanostructured Carbons. Journal of Electroceramics, 1(3), 273-286.

[3] Fang, J., Niu, H., Lin, T., & Wang, X. (2008). Applications of electrospun nanofibers. Chinese Science Bulletin, 53(15), 2265-2286.

[4] Pan, T., & Wang, W. (2011). From Cleanroom to Desktop: Emerging Micro-Nanofabrication Technology for Biomedical Applications. Annals of Biomedical Engineering, 39(2), 600-620.

[5] Upare, D., Yoon, S., & Lee, C. (2011). Nano-structured porous carbon materials for catalysis and energy storage. Korean Journal of Chemical Engineering, 28(3), 731-743.

[6] Wu, H., Pan, W., Lin, D., & Li, H. (2012). Electrospinning of ceramic nanofibers: Fabrication, assembly and applications. Journal of Advanced Ceramics, 1(1), 2-23.

[7] Amir Zabet-Khosousi and Al-Amin, D. (2007). Shadow mask fabrication of micron-wide break-junctions and their application in single-nanoparticle devices. Nanotechnology, 18(45), 455305.

[8] Bolotin, K. I., Kuemmeth, F., Pasupathy, A. N., & Ralph, D. C. (2005). From Ballistic Transport to Tunneling in Electromigrated Ferromagnetic Breakjunctions. Nano Letters, 6(1), 123-127.

[9] Chen, X., Yeganeh, S., Qin, L., Li, S., Xue, C., Braunschweig, A. B., et al. (2009). Chemical Fabrication of Heterometallic Nanogaps for Molecular Transport Junctions. Nano

Letters, 9(12), 3974-3979.

[10] Cher, M. T., & Feifei, H. (2013). Electromigration Modeling at Circuit Layout Level (1st ed.). Singapore: Springer.

[11] Feringa, B., Browne, W., van der Molen, S., Liljeroth, P. "Conductance Properties of Switchable Molecules". (2011). Wiley, 2nd Edition.

[12] Strachan, D. R., Smith, D. E., Johnston, D. E., Park, T. H., Therien, M. J., Bonnell, D. A., et al. (2005). Controlled fabrication of nanogaps in ambient environment for molecular electronics. Applied Physics Letters, 86(4), 043109-043103.

[13] Nagase, T., Gamo, K., Kubota, T., Mashiko, S. Direct fabrication of nano-gap electrodes by focused ion beam etching. (2006). Thin Solid Films, 499(1-2), 279.

[14] Esen, G., & Fuhrer, M. S. (2005). Temperature control of electromigration to form gold nanogap junctions. Applied Physics Letters, 87(26), 263101-263103.

[15] Chiu, P., Chen, K., Lin, C. Fabrication and characteristics of ultrashort-channel carbon nanotube field-effect transistors. (2008). Applied Physics Letters, 92(15), 152111.

[16] Wu, Z., Steinacher, M., Huner, R., Calame, M., van der Molen, S., Schonenberger, C. Feedback controlled electromigration in four-terminal nanojunctions. (2007). Applied Physics Letters, 91(5), 053118.

[17] See, J., Dollfus, P., Galdin, S., Hesto, P. From wave-functions to current-voltage characteristics: overview of a Coulomb blockade device simulator using fundamental physical parameters. (2006). Journal of Computational Electronics, 5(1), 35.

[18] Ramachandran, G., Edelstein, M., Blackburn, D, Suehle, J., Vogel, E., Richter, C. (2005). Nanometre gaps in gold wires are formed by thermal migration. Nanotechnology, 16(8), 1294.

[19] Hadeed, F. O., & Durkan, C. (2007). Controlled fabrication of 1-2 nm nanogaps by electromigration in gold and gold-palladium nanowires. Applied Physics Letters, 91(12), 123120-123123.

[20] Hoffmann, R., Weissenberger, D., Hawecker, J., & Stoffler, D. (2008). Conductance of gold nanojunctions thinned by electromigration. Applied Physics Letters, 93(4), 043118-043113.

[21] Heersche, H., Lientschnig, G., O'Neill, K., van der Zant, H., Zandberg, H. In situ imaging of electromigration-induced nanogap formation by transmission electron microscopy. (2007). Applied Physics Letters, 91(7), 072107.

[22] Jemmy Sutanto and Rosemary, L. S. a. S. D. C. (2010). Fabrication of nano-gap electrodes and nano wires using an electrochemical and chemical etching technique. Journal of Micromechanics and Microengineering, 20(4), 045016.

[23] Jiang, L., Dong, H., Meng, Q., Tan, J., Jiang, W., Xu, C., et al. (2012). Molecular Crystal Lithography: A Facile and Low-Cost Approach to Fabricate Nanogap Electrodes. Advanced Materials, 24(5), 694-698.

[24] Jing, J., Liang, L., & Meng, G. (2010). Electromigration Simulation for Metal Lines. Journal of Electronic Packaging, 132(1), 011002-011002.

[25] Johnston, D. E., Strachan, D. R., & Johnson, A. T. C. (2007). Parallel Fabrication of Nanogap Electrodes. Nano Letters, 7(9), 2774-2777.

[26] Kondo effects in a C60 single-molecule transistor. (2008). physica status solidi (b), NA.

[27] Li, T., Hu, W., & Zhu, D. (2010). Nanogap Electrodes. Advanced Materials, 22(2), 286-300.

[28] Lin, Y.-C., Bai, J., & Huang, Y. (2009). Self-Aligned Nanolithography in a Nanogap. Nano Letters, 9(6), 2234-2238.

[29] Liu, S., Tok, J. B. H., & Bao, Z. (2005). Nanowire Lithography: Fabricating Controllable Electrode Gaps Using Au-Ag-Au Nanowires. Nano Letters, 5(6), 1071-1076.

[30] Lu, Y., Merchant, C. A., Drndic, M., & Johnson, A. T. C. (2011). In Situ Electronic Characterization of Graphene Nanoconstrictions Fabricated in a Transmission Electron

Microscope. Nano Letters, 11(12), 5184-5188.

[31] Mahapatro, A. K., Ying, J., Ren, T., & Janes, D. B. (2008). Electronic Transport through Ruthenium-Based Redox-Active Molecules in Metal-Molecule-Metal Nanogap Junctions. Nano Letters, 8(8), 2131-2136.

[32] Bolotin, K., Kuemmeth, F, Pasupathy, A., Ralph, D. Metal-nanoparticle single-electron transistors fabricated using electromigration. (2004). Applied Physics Letters, 84(16), 3154.

[33] Moser, J., & Bachtold, A. (2009). Fabrication of large addition energy quantum dots in graphene. Applied Physics Letters, 95(17), 173506-173503.

[34] Nanogap Electrode Fabrication for a Nanoscale Device by Volume-Expanding Electrochemical Synthesis. (2011). Small, n/a.

[35] Nanogap Electrodes. (2009). Advanced Materials, NA.

[36] Park, H., Lim, A. K. L., Alivisatos, A. P., Park, J., & McEuen, P. L. (1999). Fabrication of metallic electrodes with nanometer separation by electromigration. Applied Physics Letters, 75(2), 301-303.

[37] Prins, F., Barreiro, A., Ruitenberg, J. W., Seldenthuis, J. S., Aliaga-Alcalde, N., Vandersypen, L. M. K., et al. (2011). Room-Temperature Gating of Molecular Junctions Using Few-Layer Graphene Nanogap Electrodes. Nano Letters, 11(11), 4607-4611.

[38] Strachan, D., Johnston, D., Guiton, B., Datta, S., Davies, P., Bonell, D. Real-Time TEM Imaging of the Formation of Crystalline Nanoscale Gaps. (2008). Physical Review Letters, 100(5), 056805.

[39] Mangin, A., Anthore, A., Rocca, M., Boulat, E., Lafarge, P. Reduced work functions in gold electromigrated nanogaps. (2009). Physical Review B, 80(23), 235432.

[40] Schoenenberg, C., Bernanrd, L., Calame, M., Molen, S. (2007). Controlled formation of metallic nanowires via Au nanoparticle ac trapping. Nanotechnology, 18(23), 235202.

[41] Du, K., Knutson, C., Glogowski, E., McCarthy, K., Shenhar, R., et. al. Self-Assembled

Electrical Contact to Nanoparticles Using Metallic Droplets. (2009). Small, 5(17), 1974-1977.

[42] Sense Jan van der Molen and Peter, L. (2010). Charge transport through molecular switches. Journal of Physics: Condensed Matter, 22(13), 133001.

[43] Shawn, D., Howel, S., Zmuda, S., Childs, K., Blain, M., et. al. (2005). Novel one-dimensional nanogap created with standard optical lithography and evaporation procedures. Nanotechnology, 16(10), 1983.

[44] Shi, S. F., Xu, X., Ralph, D. C., & McEuen, P. L. (2011a). Plasmon Resonance in Individual Nanogap Electrodes Studied Using Graphene Nanoconstrictions as Photodetectors. Nano Letters, 11(4), 1814-1818.

[45] Standley, B., Bao, W., Zhang, H., Bruck, J., Lau, C. N., & Bockrath, M. (2008). Graphene-Based Atomic-Scale Switches. Nano Letters, 8(10), 3345-3349.

[46] Howell, S., Dirk, S., Childs, K., Pang, H., Blain, M., Simonson, R., Tour, J., et. al. (2005). Mass-fabricated one-dimensional silicon nanogaps for hybrid organic/nanoparticle arrays. Nanotechnology, 16(6), 754.

[47] Strachan, D. R., Smith, D. E., Fischbein, M. D., Johnston, D. E., Guiton, B. S., Drndic, M., et al. (2006). Clean Electromigrated Nanogaps Imaged by Transmission Electron Microscopy. Nano Letters, 6(3), 441-444.

[48] Tanielian, M. H., Greegor, R. B., Nielsen, J. A., & Parazzoli, C. G. (2011). Fabrication of nanometer scale gaps for thermo-tunneling devices. Applied Physics Letters, 99(12), 123104-123103.

[49] Taychatanapat, T., Bolotin, K. I., Kuemmeth, F., & Ralph, D. C. (2007). Imaging Electromigration during the Formation of Break Junctions. Nano Letters, 7(3), 652-656.

[50] Trowborst, M., van der Molen, S., van Wees, B. The role of Joule heating in the formation of nanogaps by electromigration. (2006). Journal of Applied Physics, 99(11), 114316.

[51] Toshiaki Hayashi and Toshimasa, F. (2008). Voltage-pulse-induced electromigration.

Nanotechnology, 19(14), 145709.

[52] Xiang, C., Kim, J. Y., & Penner, R. M. (2009). Reconnectable Sub-5 nm Nanogaps in Ultralong Gold Nanowires. Nano Letters, 9(5), 2133-2138.

[53] Yexian Wu and Wenjing Hong and Terunobu Akiyama and Sebastian Gautsch and Viliam Kolivoska and Thomas Wandlowski and Nico, F. d. R. (2013). Batch fabrication of gold-gold nanogaps by E-beam lithography and electrochemical deposition. Nanotechnology, 24(23), 235302.

[54] Yu, H., Luo, Y., Beverly, K., Stoddart, J. F., Tseng, H.-R., & Heath, J. R. (2003). The Moleculeâ€“Electrode Interface in Single-Molecule Transistors. Angewandte Chemie International Edition, 42(46), 5706-5711.

[55] Zhao, J., Sun, H., Dai, S., Wang, Y., & Zhu, J. (2011). Electrical Breakdown of Nanowires. Nano Letters, 11(11), 4647-4651.

[56] Antipov, A. A., Arakelyan, S. M., Kutrovskaya, S. V., Kucherik, A. O., Osipov, A. V., Prokoshev, V. G., et al. (2011). Laser synthesis of carbon nanofibers and nanoclusters. Nanotechnologies in Russia, 6(5-6), 303-310.

[57] Dutta Majumdar, J., & Manna, I. (2003). Laser processing of materials. Sadhana, 28(3-4), 495-562.

[58] Ishigaki, T., Suzuki, S., Kataura, H., Krätschmer, W., & Achiba, Y. (2000). Characterization of fullerenes and carbon nanoparticles generated with a laser-furnace technique. Applied Physics A, 70(2), 121-124.

[59] Lebedev, I. G., Vorob'ev, S. A., Shushakov, V. D., & Virgil'ev, Y. S. (2002). Neutron Irradiation Induced Changes in the Structure and Properties of Glassy Carbon. Atomic Energy, 92(5), 381-385.

[60] Suzuki, S., Yamaguchi, H., Ishigaki, T., Sen, R., Kataura, H., Krätschmer, W., et al. (2001). Time evolution of emission by carbon nanoparticles generated with a laser furnace technique. The European Physical Journal D - Atomic, Molecular, Optical and Plasma Physics,

16(1), 369-372.

[61] Virgil'ev, Y. S., & Lebedev, I. G. (2002). Effect of Neutron Irradiation on Properties of Glassy Carbon. Inorganic Materials, 38(7), 668-673.

[62] Vitali, G., Rossi, M., Terranova, M. L., & Sessa, V. (1995). Laser-induced structural modifications of glassy carbon surfaces. Journal of Applied Physics, 77(9), 4307-4311.

[63] Yasumaru, N., Miyazaki, K., & Kiuchi, J. (2004). Glassy carbon layer formed in diamond-like carbon films with femtosecond laser pulses. Applied Physics A, 79(3), 425-427.

[64] Zollo, G., Palumbo, L., Rossi, M., & Vitali, G. (1993). Temperature behavior of implanted and pulsed laser irradiated GaAs. Applied Physics A, 56(5), 409-411.

[65] Tohmyoh, H. (2009). A governing parameter for the melting phenomenon at nanocontacts by Joule heating and its applications to joining together two thin metallic wires. Journal of Applied Physics, 105(1), 014907-9.

[66] Tohmyoh, H. (2013). Heat conduction model for nanowire applications. Applied Physics Letter, 102(8), 084107-4.

[67] Kitsuki, H., Yamada, T., Fabris, D., Jameson, J., Wilhite, P., Suzuki, M., et. al. (2008). Length dependence of current-induced breakdown in carbon nanofiber interconnects. Applied Physics Letters, 92(17), 173110-3.

[68] Alayo, M., Rehder, G., & Carreño, M. (2008). MEMS-based incandescent microlamps for integrated optics applications. Journal of Optics A: Pure and Applied Optics, 10(10), 104022-8.

[69] Guozhong C., & Brinker, J. (2006). Annual Review of Nano Research: Vol. I. New Mexico, USA: World Scientific Publishing.

[70] Kinoshita, S., Yoshioka, S., & Miyazaki, J. “Physics of structural colors”. (2008). Reports on Progress in Physics. 71(7), 076401.

[71] Burger, C., Hsiao, B., & Chu, B. (2006). Nanofibrous materials and their applications. Annual Review of Materials Research. 36: 333-368.

[72] Madou, M. (2011). Fundamentals of Microfabrication and Nanotechnology (3rd edition). Boca Raton, USA. CRC Press.

[73] Canton, G., Kulinsky, L., & Madou, M. (2013). Electro-mechanical spinning: A new manufacturing technique for micro/nano-fabrication of carbon fibers. IEEE International Symposium on Advanced Packing Materials. (9), 230-239.

[74] Yamada, T., Yabutani, H., Saito, T., & Yang, C. (2010). Temperature dependence of carbon nanofiber resistance. Nanotechnology, 21, 265707.

[75] Jenkins, G.,& Kawamura, K. (1971). Structure of Glassy Carbon: Nature, 231:175-176.

[76] Blakeney, B. A., Tambralli, A., Anderson, J. M., Andukuri, A., Lim, D.-J., Dean, D. R., et al. (2011). Cell infiltration and growth in a low density, uncompressed three-dimensional electrospun nanofibrous scaffold. Biomaterials, 32(6), 1583-1590.

[77] Bouta, E. M., McCarthy, C. W., Keim, A., Wang, H. B., Gilbert, R. J., & Goldman, J. (2011). Biomaterial guides for lymphatic endothelial cell alignment and migration. Acta Biomaterialia, 7(3), 1104-1113.

[78] Cao, H., Liu, T., & Chew, S. Y. (2009). The application of nanofibrous scaffolds in neural tissue engineering. Advanced Drug Delivery Reviews, 61(12), 1055-1064.

[79] Chen, F.-M., Sun, H.-H., Lu, H., & Yu, Q. (2012). Stem cell-delivery therapeutics for periodontal tissue regeneration. Biomaterials, 33(27), 6320-6344.

[80] Chew, S. Y., Mi, R., Hoke, A., & Leong, K. W. (2008). The effect of the alignment of electrospun fibrous scaffolds on Schwann cell maturation. Biomaterials, 29(6), 653-661.

[81] Cho, Y. I., Choi, J. S., Jeong, S. Y., & Yoo, H. S. (2010). Nerve growth factor (NGF)-conjugated electrospun nanostructures with topographical cues for neuronal differentiation of mesenchymal stem cells. Acta Biomaterialia, 6(12), 4725-4733.

[82] Corey, J. M., Gertz, C. C., Wang, B.-S., Birrell, L. K., Johnson, S. L., Martin, D. C., et al. (2008). The design of electrospun PLLA nanofiber scaffolds compatible with serum-free

growth of primary motor and sensory neurons. Acta Biomaterialia, 4(4), 863-875.

[83] Delcroix, G. J. R., Schiller, P. C., Benoit, J.-P., & Montero-Menei, C. N. (2010). Adult cell therapy for brain neuronal damages and the role of tissue engineering. Biomaterials, 31(8), 2105-2120.

[84] Ferreira, L., Karp, J. M., Nobre, L., & Langer, R. (2008). New Opportunities: The Use of Nanotechnologies to Manipulate and Track Stem Cells. Cell Stem Cell, 3(2), 136-146.

[85] Ghasemi-Mobarakeh, L., Prabhakaran, M. P., Morshed, M., Nasr-Esfahani, M.-H., & Ramakrishna, S. (2008). Electrospun poly(ε-caprolactone)/gelatin nanofibrous scaffolds for nerve tissue engineering. Biomaterials, 29(34), 4532-4539.

[86] Guarino, V., Alvarez-Perez, M., Cirillo, V., & Ambrosio, L. (2011). hMSC interaction with PCL and PCL/gelatin platforms: A comparative study on films and electrospun membranes. Journal of Bioactive and Compatible Polymers, 26(2), 144-160.

[87] Han, W., Mullins, M., Cregg, J., Hurtado, A., Oudega, A., et. al. (2009). Creation of highly aligned electrospun poly-L-lactic acid fibers for nerve regeneration applications. Journal of Neural Engineering, 6(1), 016001.

[88] Hartman, O., Zhang, C., Adams, E. L., Farach-Carson, M. C., Petrelli, N. J., Chase, B. D., et al. (2010). Biofunctionalization of electrospun PCL-based scaffolds with perlecan domain IV peptide to create a 3-D pharmacokinetic cancer model. Biomaterials, 31(21), 5700-5718.

[89] Kabiri, M., Soleimani, M., Shabani, I., Futrega, K., Ghaemi, N., Ahvaz, H., et al. (2012). Neural differentiation of mouse embryonic stem cells on conductive nanofiber scaffolds. Biotechnology Letters, 34(7), 1357-1365.

[90] Karam, J.-P., Muscari, C., & Montero-Menei, C. N. (2012). Combining adult stem cells and polymeric devices for tissue engineering in infarcted myocardium. Biomaterials, 33(23), 5683-5695.

[91] Kim, H. N., Jiao, A., Hwang, N. S., Kim, M. S., Kang, D. H., Kim, D.-H., et al. Nanotopography-guided tissue engineering and regenerative medicine. Advanced Drug

Delivery Reviews (0).

[92] Kundu, B., Rajkhowa, R., Kundu, S. C., & Wang, X. Silk fibroin biomaterials for tissue regenerations. Advanced Drug Delivery Reviews(0).

[93] Lee, M. R., Kwon, K. W., Jung, H., Kim, H. N., Suh, K. Y., Kim, K., et al. (2010). Direct differentiation of human embryonic stem cells into selective neurons on nanoscale ridge/groove pattern arrays. Biomaterials, 31(15), 4360-4366.

[94] Lim, S. H., Liu, X. Y., Song, H., Yarema, K. J., & Mao, H.-Q. (2010). The effect of nanofiber-guided cell alignment on the preferential differentiation of neural stem cells. Biomaterials, 31(34), 9031-9039.

[95] Lim, S. H., & Mao, H.-Q. (2009). Electrospun scaffolds for stem cell engineering. Advanced Drug Delivery Reviews, 61(12), 1084-1096.

[96] Low, W. C., Rujitanaroj, P.-O., Lee, D.-K., Messersmith, P. B., Stanton, L. W., Goh, E., et al. Nanofibrous scaffold-mediated REST knockdown to enhance neuronal differentiation of stem cells. Biomaterials(0).

[97] Maitra, T., Sharma, S., Srivastava, A., Cho, Y.-K., Madou, M., & Sharma, A. (2012). Improved graphitization and electrical conductivity of suspended carbon nanofibers derived from carbon nanotube/polyacrylonitrile composites by directed electrospinning. Carbon, 50(5), 1753-1761.

[98] Mukhatyar, V. J., Salmerón-Sánchez, M., Rudra, S., Mukhopadaya, S., Barker, T. H., García, A. J., et al. (2011). Role of fibronectin in topographical guidance of neurite extension on electrospun fibers. Biomaterials, 32(16), 3958-3968.

[99] Nayak, R., Padhye, R., Kyratzis, I. L., Truong, Y. B., & Arnold, L. (2012). Recent advances in nanofibre fabrication techniques. Textile Research Journal, 82(2), 129-147.

[100] Prabhakaran, M. P., Ghasemi-Mobarakeh, L., Jin, G., & Ramakrishna, S. (2011). Electrospun conducting polymer nanofibers and electrical stimulation of nerve stem cells. Journal of Bioscience and Bioengineering, 112(5), 501-507.

[101] Prabhakaran, M. P., Venugopal, J. R., & Ramakrishna, S. (2009). Mesenchymal stem cell differentiation to neuronal cells on electrospun nanofibrous substrates for nerve tissue engineering. Biomaterials, 30(28), 4996-5003.

[102] Perez, R. A., Won, J.-E., Knowles, J. C., & Kim, H.-W. Naturally and synthetic smart composite biomaterials for tissue regeneration. Advanced Drug Delivery Reviews (0).

[103] Shin, S.-H., Purevdorj, O., Castano, O., Planell, J. A., & Kim, H.-W. (2012). A short review: Recent advances in electrospinning for bone tissue regeneration. Journal of Tissue Engineering, 3(1).

[104] Sokolsky-Papkov, M., Agashi, K., Olaye, A., Shakesheff, K., & Domb, A. J. (2007). Polymer carriers for drug delivery in tissue engineering. Advanced Drug Delivery Reviews, 59(4ΓÇô5), 187-206.

[105] Spasova, M., Stoilova, O., Manolova, N., Rashkov, I., & Altankov, G. (2007). Preparation of PLLA/PEG Nanofibers by Electrospinning and Potential Applications. Journal of Bioactive and Compatible Polymers, 22(1), 62-76.

[106] Subramaniam, J., Turon, G., Gorkin, R., Tripathi, P., Bisht, G., et. al. (2008). Carbon microelectromechanical systems as a substratum for cell growth. Biomedical Materials, 3(3), 034116.

[107] Subramanian, A., Krishnan, U., & Sethuraman, S. (2012). Axially aligned electrically conducting biodegradable nanofibers for neural regeneration. Journal of Materials Science: Materials in Medicine, 23(7), 1797-1809.

[108] Wan, A. C. A., & Ying, J. Y. (2010). Nanomaterials for in situ cell delivery and tissue regeneration. Advanced Drug Delivery Reviews, 62(7ΓÇô8), 731-740.

[109] Wang, H. B., Mullins, M. E., Cregg, J. M., McCarthy, C. W., & Gilbert, R. J. (2010). Varying the diameter of aligned electrospun fibers alters neurite outgrowth and Schwann cell migration. Acta Biomaterialia, 6(8), 2970-2978.

[110] Wang, L., Wang, Z.-H., Shen, C.-Y., You, M.-L., Xiao, J.-F., & Chen, G.-Q. (2010).

Differentiation of human bone marrow mesenchymal stem cells grown in terpolyesters of 3-hydroxyalkanoates scaffolds into nerve cells. Biomaterials, 31(7), 1691-1698.

[111] Wang, T.-Y., Forsythe, J. S., Nisbet, D. R., & Parish, C. L. (2012). Promoting engraftment of transplanted neural stem cells/progenitors using biofunctionalised electrospun scaffolds. Biomaterials, 33(36), 9188-9197.

[112] Yim, E. K. F., & Leong, K. W. (2005). Significance of synthetic nanostructures in dictating cellular response. Nanomedicine: Nanotechnology, Biology and Medicine, 1(1), 10-21.

[113] Yim, E. K. F., Wen, J., & Leong, K. W. (2006). Enhanced extracellular matrix production and differentiation of human embryonic germ cell derivatives in biodegradable poly(ε-caprolactone-co-ethyl ethylene phosphate) scaffold. Acta Biomaterialia, 2(4), 365-376.

[114] Yu, L. M. Y., Leipzig, N. D., & Shoichet, M. S. (2008). Promoting neuron adhesion and growth. Materials Today, 11(5), 36-43.

[115] Zhang, L., & Webster, T. J. (2009). Nanotechnology and nanomaterials: Promises for improved tissue regeneration. Nano Today, 4(1), 66-80.

[116] Zhao, C., Tan, A., Pastorin, G., & Ho, H. K. Nanomaterial scaffolds for stem cell proliferation and differentiation in tissue engineering. Biotechnology Advances (0).

[117] Cho, J., Inam, F., Reece, M., Chlup, Z. k., Dlouhy, I., Shaffer, M. P., et al. (2011). Carbon nanotubes: do they toughen brittle matrices? Journal of Materials Science, 46(14), 4770-4779.

[118] Lyshevski, S. (2007). Nano and Molecular Electronics Handbook (1st edition). Boca Raton, USA. CRC Press.

[119] Small, M. (2012). Dynamics of Biological Systems (1st edition). Boca Raton, USA. CRC Press.

[120] National Instruments. (Unknown). NI MyDAQ. In National Instruments. Retrieved

November 1, 2013, from http://www.ni.com/mydaq/.

[121] National Instruments. (Unknown). Labview System Design Software. In National Instruments. Retrieved November 1, 2013, from http://www.ni.com/labview/.

[122] Leica Microsystems, (Unknown). Bal-Tec. CED 030. In Leica Microsystems. Retrieved November 1, 2013, from: http://www.leica-microsystems.com/index.php?id=732.

[123] Personal communication with Dr. Ricardo Pulido, Mathematics Department, Tecnológico de Monterrey, Monterrey Campus, November 13, 2013.